NTNU – Trondheim
Norwegian University of
Science and Technology

Vortex Induced Vibrations on an ''Artificial Seabed'' for Support of a Floating Bridge

Simon Grevstad

Marine Technology
Submission date: June 2015
Supervisor: Carl Martin Larsen, IMT

Norwegian University of Science and Technology
Department of Marine Technology

NTNU Trondheim
Norwegian university of science and technology
Department of marinetechnology

MASTER THESIS, SPRING 2015

for

SIMON GREVSTAD

VORTEX INDUCED VIBRATIONS ON AN "ARTIFICIAL SEABED" FOR SUPPORT OF A FLOATING BRIDGE

Planning of a new highway on the west coast of Norway is now in progress. An important part of this work is to design new bridges across wide and deep fjords. A large number of designs will be studied, and a variety of load cases must be investigated during the construction and completed stages for each bridge.

One concept applies an "artificial seabed" to support the bridge. This structure consists of two submerged tensioned lines made by steel pipes which are connected by a set of tensioned members. The steel pipes are anchored to land on each side of the fjord, while the members are oriented along the fjord. The "artificial seabed" will be installed prior to the floating bridge and possibly stay one winter season without being connected to the floating bridge.

The fjord will have tidal and wind generated current in addition to current caused by rivers. Vortex induced vibrations (VIV) may therefore appear in slender structures like the tensioned cylinders in the actual "artificial seabed". The purpose of the master thesis is to make analyses of VIV for this structure.

The work may be carried out in steps as follows:

1. Conduct model experiments in the Marine Cybernetics Laboratory to get hydrodynamic data for a pipe bundle consisting of 3 pipes.
2. Calculate VIV on the artificial seabed when both attached to and detached from the floating bridge. The hydrodynamic coefficients found in step 1 should be included for this analysis. The computer program VIVANA should be applied.
3. Define main uncertainties linked to the analyses, and if needed proposal for further work.

The work may show to be more extensive than anticipated. Some topics may therefore be left out after discussion with the supervisor without any negative influence on the grading.

The candidate should in her/his report give a personal contribution to the solution of the problem formulated in this text. All assumptions and conclusions must be supported by mathematical models and/or references to physical effects in a logical manner.
The candidate should apply all available sources to find relevant literature and information on the actual problem.

The report should be well organised and give a clear presentation of the work and all conclusions. It is important that the text is well written and that tables and figures are used to support the verbal presentation. The report should be complete, but still as short as possible.

The final report must contain this text, an acknowledgement, summary, main body, conclusions and suggestions for further work, symbol list, references and appendices. All figures, tables and equations must be identified by numbers. References should be given by author name and year in the text, and presented alphabetically by name in the reference list. The report must be submitted in two copies unless otherwise has been agreed with the supervisor.

The supervisor may require that the candidate should give a written plan that describes the progress of the work after having received this text. The plan may contain a table of content for the report and also assumed use of computer resources.

From the report it should be possible to identify the work carried out by the candidate and what has been found in the available literature. It is important to give references to the original source for theories and experimental results.

The report must be signed by the candidate, include this text, appear as a paperback, and - if needed - have a separate enclosure (memory stick or DVD/ CD) with additional material.

The work will be carried out in cooperation with Deep Ocean

Supervisor: Carl M. Larsen
Co-supervisor at Deep Ocean: Martin Hasle

Deadline: 10 June 2015

Trondheim, January 2015

Carl M. Larsen

Preface

This master thesis investigates the effects of vortex induced vibrations (VIV) on an artificial seabed in the Sognefjord. An artificial seabed is a structure for anchoring a floating bridge. It is designed and patented by the company Reinertsen. The project has been done in collaboration with Deepocean and Reinertsen.

The artificial seabed has been modelled when assumed attached to and detached from the floating bridge and tunnel. The software VIVANA was used for calculating VIV effects.

To get the best possible hydrodynamic data of a bundle consisting of three pipes, model experiments were conducted in the Marine Cybernetics Lab at NTNU. The relevant results from the experiments were used in the VIV calculations in VIVANA.

I would like to thank my supervisor, Professor Carl Martin Larsen for guiding me in this project. His advice and comments have been of great value. I am also very grateful that he gave me the opportunity to do experiments in the MC-lab. Martin Hasle at Deepocean should also be thanked for giving me the opportunity to work with this project. Moreover I would like to thank Marit Reiso at Reinertsen for providing useful information and showing interest in the project.

Torgeir Wahl, which is part of the NTNU laboratory staff, should also be thanked. His help in the MC-lab has been of huge importance for the experiments. Also I would like to thank PhD Decao Jin for briefing me on how to do the laboratory experiments and providing MATLAB code examples.

Abstract

The engineering company Reinertsen is planning a floating bridge with tunnel that will go across the Sognefjord. Reinertsen has designed what they call an "artificial seabed" to be used for anchoring of the floating bridge. The subsea company Deepocean is hired by Reinertsen to look at the installation possibilites of this construction. It is of Deepoceans and Reinertsens interest to see how vortex induced vibrations (VIV) may affect the artificial seabed.

The main objectives of this master thesis have been to do VIV calculations on the artificial seabed when modeled as connected to and detached from the floating bridge and tunnel. The calculations were done in the software VIVANA developed at MARINTEK.

The artificial seabed is made of two main bundles each consisting of three pipes. To get realistic hydrodynamic data for a bundle with three pipes, model experiments were conducted in the Marine Cybernetics Laboratory at NTNU. The model experiments were also one of the main objectives in this thesis.

The model experiments were done using forced vibrations in a tank filled with water. The model was mounted to a yoke and carriage system programmed to run the model with constant velocity through the tank. Both pure cross-flow and combined in-line/cross-flow tests were done. Three different orientations of the bundle relative to the current flow were used. The results of the experiments were excitation, added mass, drag and lift coefficients. The Strouhals number was also calculated for each orientation. The results from the combined in-line/cross-flow tests showed that VIV will not occur for the combinations of phase angles and amplitudes used in the experiments.

Pure cross-flow analyses were done in VIVANA using the hydrodynamic coefficients found from the experiments. The shortest fatigue life found for the case where the artificial seabed model was assumed connected to the

floating bridge was $0.23919 \cdot 10^6$ years. For the cases where the artificial seabed model was assumed detached from the floating bridge and tunnel, the shortest fatigue life was found to be $0.24240 \cdot 10^6$ years. The large fatigue life implies that vortex induced vibrations will not be a problem to the artificial seabed. The results are however uncertain due to the limitations of the study.

Sammendrag

Ingeniørselskapet Reinertsen planlegger en flytebro med tunnel som vil gå over Sognefjorden. Reinertsen har utviklet det de kaller en "kunstig sjøbunn" som skal brukes til forankring av flytebroen. Subsea-selskapet Deepocean er innleid av Reinertsen for å se på hvordan denne konstruksjonen kan bli installert. Det er av Deepoceans og Reinertsens interesse å se hvordan virvelinduserte vibrasjoner (VIV) kan påvirke den kunstige sjøbunnen.

De viktigste målene for denne masteroppgaven har vært å gjøre VIV-beregninger på den kunstige sjøbunnen modellert som både frakoblet og tilkoblet flytebroen. Beregningene ble gjort i programvaren VIVANA utviklet ved MARINTEK.

Den kunstige sjøbunnen er laget av to moduler som hver består av tre rør. For å få realistiske hydrodynamiske data for disse modulene, ble modellforsøk gjennomført i MC-laben ved NTNU. Modellforsøkene utgjorde også et av hovedmålene i oppgaven.

Modellforsøkene ble utført ved hjelp av tvungne vibrasjoner i en tank fylt med vann. Modellen ble montert på et åk og vognsystem som var programmert til å kjøre modellen med konstant hastighet gjennom tanken. Både ren cross-flow (CF) og kombinert in-line (IL) og CF forsøk ble utført. Tre forskjellige orienteringer av modellen i forhold til strømningsretningen ble brukt. Resultatene av forsøkene var eksitasjon, tilleggsmasse, drag og løftkoeffisienter. Strouhals tall ble også beregnet for hver retning. Resultatene fra de kombinerte CF/IL testene viste at VIV ikke vil forekomme for de kombinasjoner av fasevinkler og amplituder brukt i forsøkene.

Rene CF analyser ble gjort i VIVANA ved hjelp av hydrodynamiske koeffisienter funnet fra forsøkene. Den korteste utmattingslevetiden funnet for det tilfellet hvor den kunstige sjøbunn-modellen ble antatt forbundet med flytebroen var $0.23919 \cdot 10^6$ år. For de tilfellene hvor den kunstige sjøbunnmodellen var antatt frakoblet fra flytebroen, ble den korteste utmattingsleve-

tiden $0.24240 \cdot 10^6$ år. Den store utmattingslevetiden innebærer at virvelinduserte vibrasjoner ikke vil være et problem for den kunstige sjøbunnen. Resultatene er noe usikre på grunn av begrensningene som er gjort i oppgaven.

Contents

List of Figures

List of Tables

Nomenclature

Abbreviations

2D	Two dimensional
3D	Three dimensional
CF	Cross-flow
DRE	Data reduction equation
IL	In-line
MC-lab	Marine Cybernetics Laboratory
MCL	File extension of the carriage input files
NTNU	Norwegian University of Science and Technology
PhD	Doctor of Philosophy
STD	Standard deviation
VIV	Vortex induced vibrations
WL	Waterline

Roman symbols

A	Oscillation amplitude, cross section area
A_{cs}	Cross section area of pipe
A/D	Amplitude ratio in CF or IL direction
$A/D_{Ce=0}$	Amplitude ratio in CF or IL direction where Ce=0
A_{void}	Area of the void between the pipes in the bundle model
A_{wp}	Waterplane area
a	Constant used in velocity profile 2
$a_{CF/IL}$	Acceleration in CF or IL direction
$a_{max,pipe}$	Maximum vertical acceleration of the pipe section

$a(t)$	Acceleration as a function of time in z-direction
a_0	Acceleration at t=0
B	Bias error
C	Constant used in velocity profile 2
$C_a, C_{a,CF/IL}$	Added mass coefficient in CF or IL direction
C_D	Drag coefficient
$C_e, C_{e,CF/IL}$	Dynamic excitation coefficient in CF or IL direction
C_L	Lift coefficient
D	Hydrodynamic diameter used in the amplitude ratio / Outer diameter of one pipe in the bundle
D_H	Hydrodynamic diameter of the bundle model
$D_{H,fullscale}$	Hydrodynamic diameter of the full scale bundle
D_i	Internal diameter of one pipe in the bundle
$D_{iel,iend,ipt}$	accumulated fatigue damage
$D_{pipe,fullscale}$	Outer diameter of one pipe in the full scale bundle
dl	Change in length in axial direction
dz	Change in length in z direction
E	Young's modulus
E_i	Excitation parameter
F_{CF}	Measured force in CF direction
$F_{ex,max}$	Maximum external force from the pipe section
$F_{ex,z}$	Force acting on pontoon in positive z-direction
$F_{hydro}, F_{hydro,CF/IL}$	Hydrodynamic force in IL or CF direction
$F_{hydro,0}$	Hydrodynamic force amplitude
F_IL	Measured force in IL direction
$F_{measured,CF/IL}$	Force measured by force sensors in CF or IL direction
f_{curr2}	Function used to calculate Velocity Profile 2
f_{osc}	Oscillation frequency in CF or IL direction
f_v	vortex shedding frequency
F_{wp}	Force due to waterplane stiffness
f_0	Eigenfrequency in still water
$\hat{f}$	Nondimensional frequency in IL or CF direction
g	Acceleration of gravity
k, K	Stiffness
k_{wp}	Waterplane stiffness
L	Bundle model length / crossbar length

L_{ps}	Length of pipe section
M_H	Added mass matrix
M_p	Total mass of bundle model, shafts, shaft housing and cylinders
M_s	Mass matrix
$M_w, void$	Mass of water inside the void between the pipes in the bundle model
m	Mass
m_ps	Mass of pipe section
m_a	Added mass
N_i	Number of cycles to failure for stress cycle i
n	sample size, number of oscillation periods
$n_{i,year,iel,iend,ipt}$	The total number of cycles for stress range i during a year
Re	Reynolds number
s	standard deviation of a sample
St	Strouhals number
t	Time variable
$t_{0.05}$	t-value for a 95% confidence interval
T	Time
T_H	Horizontal pretension
T_{osc}	Oscillation period
U_0	Flow velocity
U_N	Normal component of the flow velocity
x_j	Sample value j
x_0	Displacement amplitude, x-coordinate at the end of the fjord
$\dot{x_0}$	Velocity amplitude
$\dot{x_0}$	Acceleration amplitude
$\bar{x}$	mean of a sample
y	y-coordinate
z	z-coordinate
z_0	z-position at t=0
$\dot{z}$	Derivating z with respect to time
$\ddot{z}$	Derivating z with respect to time two times

Greek symbols

α	Phase angle describing the orbital shape, angle between cross bar and the horizontal line
$\Delta\sigma$	Stress ranges
$\Delta\sigma_i$	Stress range i
Δz	Change in z-direction
γ	Damping coefficient
μ	Mean of a population
$\mu_{CI95\%}$	95% confidence interval of μ
ν	Kinematic viscosity
π	3.141592..
ρ	Density of water in laboratory tank (fresh water)
ρ_{steel}	Density of steel
ρ_{sw}	Density of sea water
ϕ	Phase angle between force and displacement, general phase angle
ω	Circular frequency, underdamped harmonic motion
ω_{osc}	Circular oscillation frequency

Chapter 1

Introduction

1.1 Background information

The engineering company Reinertsen is working with the concept of a floating bridge connecting the highway E39 on each side of the Sognefjord. Due to the great depth and difficult bottom conditions in the fjord, Reinertsen has designed what they call an artificial seabed. This artificial seabed will be used to anchor the floating bridge.

The subsea engineering company Deepocean has been hired to investigate how the artificial seabed can be installed. It is of Deepocean and Reinertsen's interest to get to know the influence of vortex induced vibrations (VIV) on the artificial seabed due to currents in the fjord.

1.2 Objective

The main objectives of this master thesis has been to calculate the effect of VIV on an artificial seabed, and to perform model experiments of a bundle with three pipes. Two primary calculations have been done: one with the artificial seabed attached to the floating bridge, and one with the artificial seabed detached from the floating bridge. To get the best possible hydrodynamic data for the calculations, model experiments of a bundle consisting of three pipes were done.

1.3 Scope and limitations

The project of the artificial seabed and floating bridge is at an early phase. Because of this not all information about the construction is ready, and assumptions has been made. One assumption was that the pipes in the bundles were in direct contact with each other. Another assumption done in this project was the number and position of the cross bars connecting the artificial seabed and tunnel.

The model experiments done in this project are linked to a number of uncertainties. The uncertainties are addressed in this report. The model experiments were all done at a Reynolds number of $2.0 \cdot 10^4$. The Reynolds number in the full scale scenario is of order 10^6. Thus the data used in VIVANA from the model experiments will give some uncertainties in the calculations related to this.

Due to the limited time in the laboratory, prioritization had to be done regarding what tests to run. As a result of this, the data for the combined cross-flow and in-line tests were signifanctly limited compared to the data from the pure cross-flow tests. The VIV analyses in this thesis are based on the limited data from the experiments and the results should be interpreted carefully.

VIVANA uses some simplifications in its calculations. One simplification is the choice of using a constant added mass for each nondimensional frequency. The simplifications should accounted for when interpreting the results.

When doing the calculations in VIVANA, the focus has been on providing the best possible hydrodynamic coefficients and parameters. As a result of this, the discussion and configuration of the fatigue analyses in VIVANA have been deprioritized. A SN curve following one of the examples in VIVANA has been used in the fatigue analyses.

The current data used in this project is based on a report by SINTEF. These current data are found using numerical methods, and may differ from the actual velocities in the fjord. The data does however include a significant safety margin and will be considered conservative. The current profiles made in VIVANA are based on these current data. The VIVANA profiles are made to be simple estimations of the actual current profiles in the fjord.

Chapter 2

The concept of the floating bridge and artificial seabed

A floating bridge with tunnel is planned across the Sognefjord to connect the highway E39 on each side of the fjord (Deepocean, 2014). Due to the great depth of the Sognefjord, and the challenging bottom conditions, Reinertsen has come up with the design of an artificial seabed. The artificial seabed is used for anchoring the floating bridge and tunnel. The concept of the floating bridge with tunnel and artificial seabed is shown in Figure 2.1.

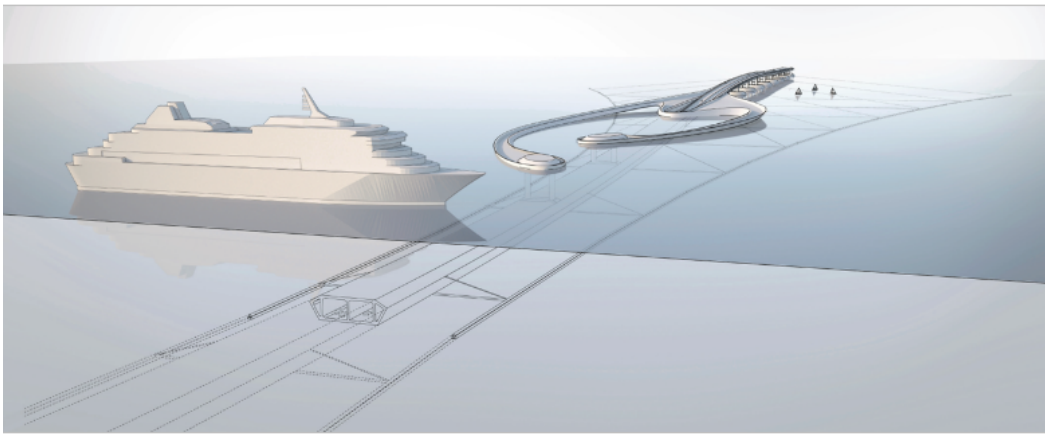

Figure 2.1: An illustration of the floating bridge and tunnel connected to the artificial seabed (Reinertsen, 2014).

2.1 The artificial seabed

The artificial seabed is made of two main pipe bundles crossing the fjord at 30m depth (Reinertsen, 2014). The two pipe bundles are pulled together by 13 cross pipes which increase the stiffness of the construction. An illustration of the artificial seabed is shown in Figure 2.2.

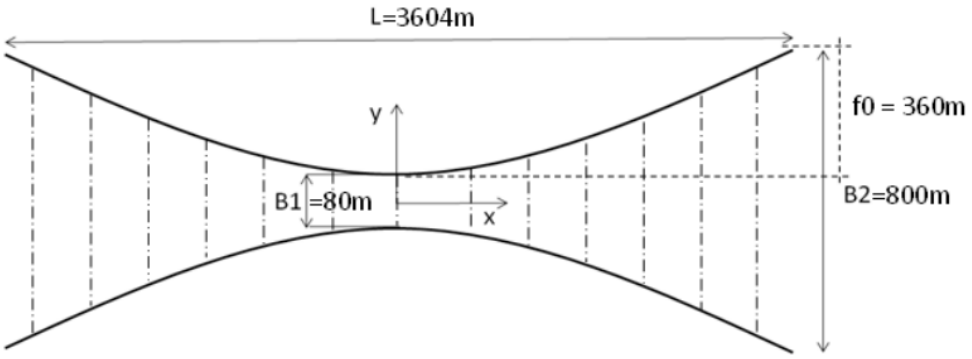

Figure 2.2: The artificial seabed as seen from above (Reinertsen, 2014). It should be noticed that the length/width ratio in the figure is different from the real model.

The two main pipe bundles each consist of three pipes. The cross section of one pipe bundle is shown in Figure 2.3.

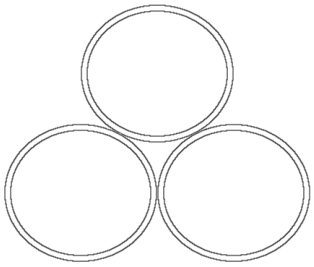

Figure 2.3: The cross section geometry of one pipe bundle

The cross section dimensions of the bundle are listed in Table 2.1, as specified by Reinertsen.

The bundles and cross pipes are made of steel (Reinertsen, 2014). When the artificial seabed is installed as shown in Figure 2.2 the bundles will get

Table 2.1: Cross section dimensions of the bundle (Reinertsen, 2014).

Parameter	Value
Diameter of one pipe	$0.9144m$
Wall thickness of one pipe	$0.0305m$
Cross section area of the solid bundle	$0.254m^2$

pre-stressed to 40% of the yield stress. The resulting pre-stress is listed in Table 2.2 along with the material specific data of the bundles.

Table 2.2: Pre-stress and material specific data of the bundles (Reinertsen, 2014).

Parameter	Value
Density (steel)	$7850\frac{kg}{m^3}$
Youngs modulus	$207 \cdot 10^9 Pa$
Yield stress	$480 \cdot 10^6 Pa$
Prestress	$192 \cdot 10^6 Pa$

2.2 The floating bridge and tunnel

The floating bridge is made up of two 1002m long modules on each side of the fjord (Reinertsen, 2014). The tunnel is located between the two floating bridge modules and is 1600m long.

2.2.1 Tunnel dimensions

The cross section of the tunnel is shown in Figure 2.4. The tunnel is 23m wide at the bottom and has a height of 9m. The tunnel will be connected to the artificial seabed using some crossbars (Reiso, 2015). This is to increase the horizontal stiffness of the tunnel. The number of crossbars are not decided yet, but has been assumed to be one per pontoon in connection with the tunnel, on each side of the artificial seabed. This was decided after discussions with Marit Reiso at Reinertsen (Reiso, 2015).

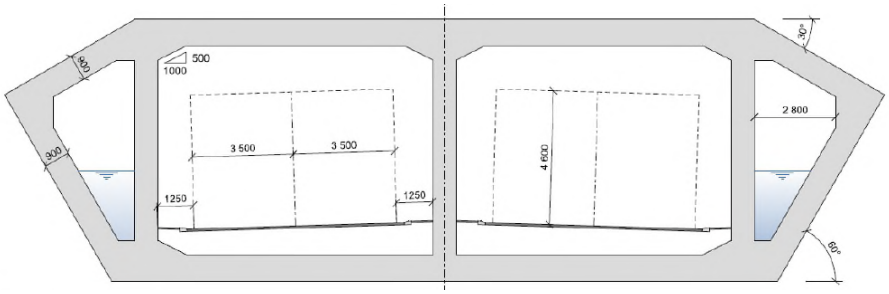

Figure 2.4: The cross section of the tunnel (Reinertsen, 2014).

Table 2.3 shows the tunnel dimensions that will be used later in this project.

Table 2.3: Tunnel cross section dimensions used in this project, taken from Reinertsen (Reinertsen, 2014).

Parameter	Value
Width at bottom	23m
Total height	9m

2.2.2 Pontoons

The floating bridge and tunnel are connected to a total of 24 pontoons to get the necessary buoyancy. This is illustrated in Figure 2.5.

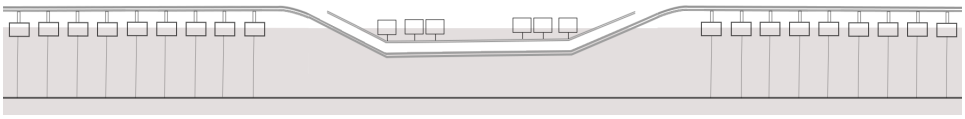

Figure 2.5: A simplified illustration of the floating bridge and tunnel connected to pontoons.

The floating bridge is mounted on top of cylindrical pontoons. The properties of the pontoons are given in Table 2.4

Six pontoons are mounted directly to the tunnel. These pontoons are of different geometry and size than the cylindrical pontoons mounted to the float bridge modules. Since these six pontoons are not directly connected to the artificial seabed they will not be further described.

Table 2.4: Properties of the cylindrical pontoon

Parameter	Value
Diameter	31.0m
Height	8.5m
Freeboard	3.5m
Draught	5.0m

2.2.3 Crossbars

The pontoons are anchored to the artificial seabed by crossbars. These bars are cylindrical shaped and made of steel. The properties of the bars are given in Table 2.5.

Table 2.5: Properties of the mounting bars

Property	Value
Outer diameter	$0.30m$
Inner diameter	$0.28m$
Wall thickness	$0.01m$
Cross section area	$0.009m^2$
Youngs module	$207GPa$

2.3 Current velocities

The current velocities used in this project are based on the current velocities calculated for the Sognefjord by SINTEF (SINTEF, 2011). The velocities are listed in Table 2.6.

Table 2.6: Current data for the Sognefjord as calculated by SINTEF (SINTEF, 2011).

Water depth$[m]$	$U_{out}[m/s]$	$U_{mean}[m/s]$	$U_{in}[m/s]$
$0-10$	-1.06	-0.533	1.27
30	-0.55	0.258	0.48
75	-0.44	0.257	0.39

The artificial seabed is located at 30m depth, and hence the velocities at this depth were used in this project.

Chapter 3

The stiffness acting on the artificial seabed

One of the main objectives in this master thesis was to calculate VIV on the artificial seabed when attached to the floating bridge. In the last chapter it was described how the artificial seabed will be connected to a set of pontoons which in turn will be connected to the floating bridge. The artificial seabed will be connected to the pontoons by some mounting bars. When calculating VIV on the artificial seabed in connection with the floating bridge, the stiffness from the pontoons and mounting bars must be considered. In this chapter the procedure and results of the calculations of these stiffnesses will be described. The results from the calculations will be used in the VIVANA analyses where the floating bridge and tunnel are included.

3.1 Stiffness from the pontoons

The mass of the pontoons is relatively big compared to the mass of the main pipes in the artificial seabed. Thus the force from the acceleration of the main pipes will not be able to move the pontoons. The pontoons can therefore be modelled as rigid. This can be shown by looking at a pontoon in equiblibrium condition in the water. The weight of the pontoon is balanced by the buoyancy. Any additional external force working on the pontoon in positive z-direction will move the pontoon upwards a distance Δz.

In this case the external force $F_{ex,z}$ will be due to the acceleration from the oscillation of the main pipe. It is of interest to find the maximum value

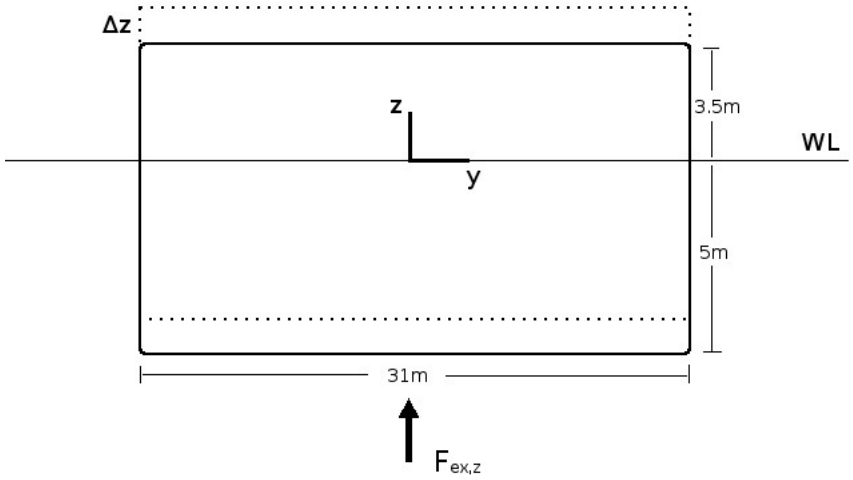

Figure 3.1: An external force $F_{ex,z}$ in the positive z-direction will move the pontoon a distance Δz upwards.

of this external force.

3.1.1 Calculating the maximum external force

Considering a simple mass-spring system, the movement in z-direction as a function of time is given by:

$$z(t) = z_0 + Acos(\omega t + \phi) \tag{3.1}$$

Where z_0 is the equilibium position of the mass, A the amplitude, ω the angular frequency, t the time and ϕ the phase angle.

Derivating Equation 3.1 with respect to t two times, the acceleration of the mass becomes:

$$a(t) = \ddot{z} = a_0 - \omega^2 Acos(\omega t + \phi) \tag{3.2}$$

Using $a_0 = 0$ and knowing that the maximum of the cosinus function is 1 the maximum acceleration of the pipe is:

$$a_{max} = -\omega^2 A \tag{3.3}$$

Based on the VIVANA analyses done in the project thesis of Grevstad (2014), the values are found to be $\omega = 0.355\frac{rad}{s}$ and $A_{maks} = 0.64m$. The values are taken from the dominating mode found for the simple model in the simplified analyses of the project thesis (Grevstad, 2014). Both ω and A_{maks} will be affected by the stiffness from the bars connecting the artificial seabed to the pontoons. However it is assumed that these values are in worst case conservative.

Inserting the values above, the maximum acceleration becomes:

$$a_{max,pipe} = -\omega^2 A = -(0.355\frac{rad}{s})^2 * 0.64m = 0.081\frac{m}{s^2} \tag{3.4}$$

The pontoons are placed every 106m from land along the length of the floating bridge. It is therefore assumed that 106m of the accelerated pipe can be used for calculating the mass. The mass of the accelerated pipe part then becomes:

$$m_{ps} = A_{cs} * \rho_{steel} * L_{ps} = 0.254m^2 * 7850\frac{kg}{m^3} * 106m = 211 * 10^3 kg \tag{3.5}$$

Where m_{ps} is the mass of the pipe section, A_{cs} the cross section area of the pipe, ρ_{steel} the density of steel and L_{ps} the length of the pipe section.

The maximum mass force from the main pipe is then calculated to be:

$$F_{ex,max} = m_{ps} * a_{max,pipe} = 211 * 10^3 kg * 0.081\frac{m}{s^2} = 17091N \tag{3.6}$$

3.1.2 Finding the maximum displacement of the pontoon

The next step is to find the maximum displacement, Δz_{max}, caused by the previously found maximum external force $F_{ex,max}$. This is found by balancing the maximum external mass force with the force from the water plane stiffness of the pontoon. The force due to the water plane stiffness is given by:

$$F_{wp} = k_{wp}\Delta z = \rho_{sw} g A_{wp} \Delta z \tag{3.7}$$

Where ρ_{sw} is the density of the seawater, g the gravity acceleration, and A_{wp} the water plane area.

Balancing the two forces gives:

$$F_{wp} = F_{ex,max} = \rho_{sw} g A_{wl} \Delta z = m_{ps} * a_{max,pipe} \tag{3.8}$$

Rearranging the equation gives:

$$\Delta z = \frac{m_{ps} * a_{max,pipe}}{\rho_{sw} g A_{wl}} = \frac{17091N}{1027\frac{kg}{m^3} * 9.81\frac{m}{s^2} * \frac{\pi}{4} * (31m)^2} = 0.002m \tag{3.9}$$

When calculating the water plane area of the pontoon it is used a diameter of 31m as described in Table 2.4 in Section 2.2.2

The small displacement of only 0.002m shows that the pontoons may in general be seen as rigid. It should be noted that these calculations are very simplified. It is however assumed that only the bars connecting the pontoons (and tunnel) with the main pipe will give a vertical stiffness.

3.2 Stiffness from the mounting bars

The bar connecting the pontoon to one of the main pipes in the artificial seabed will have an elastic stiffness given by $K = \frac{EA}{L}$. If the main pipe is moved downwards by a force P, as shown in Figure 3.2, the bar will be stretched a distance dl given by:

$$dl = \frac{\frac{P}{sin(\alpha)}}{\frac{EA}{L}} \tag{3.10}$$

Where $\frac{P}{sin(\alpha)}$ is the component of P paralell to the initial position of the spring (bar), and $\frac{EA}{L}$ is the stiffness of the spring.

Figure 3.3 shows how the same elongation dl is geometrically related to the vertical displacement dz of the main pipe and the angle α, which is the same angle as in Figure 3.2.

The following relation is seen from Figure 3.3:

$$dl = dz * sin(\alpha) \tag{3.11}$$

Combining Equation 3.10 and 3.11 give the following expression for dz:

$$dz = \frac{dl}{sin(\alpha)} = \frac{\frac{P}{sin(\alpha)}}{\frac{EA}{L} * sin(\alpha)} = \frac{P}{\frac{EA}{L} * sin^2(\alpha)} = \frac{P}{K_z} \tag{3.12}$$

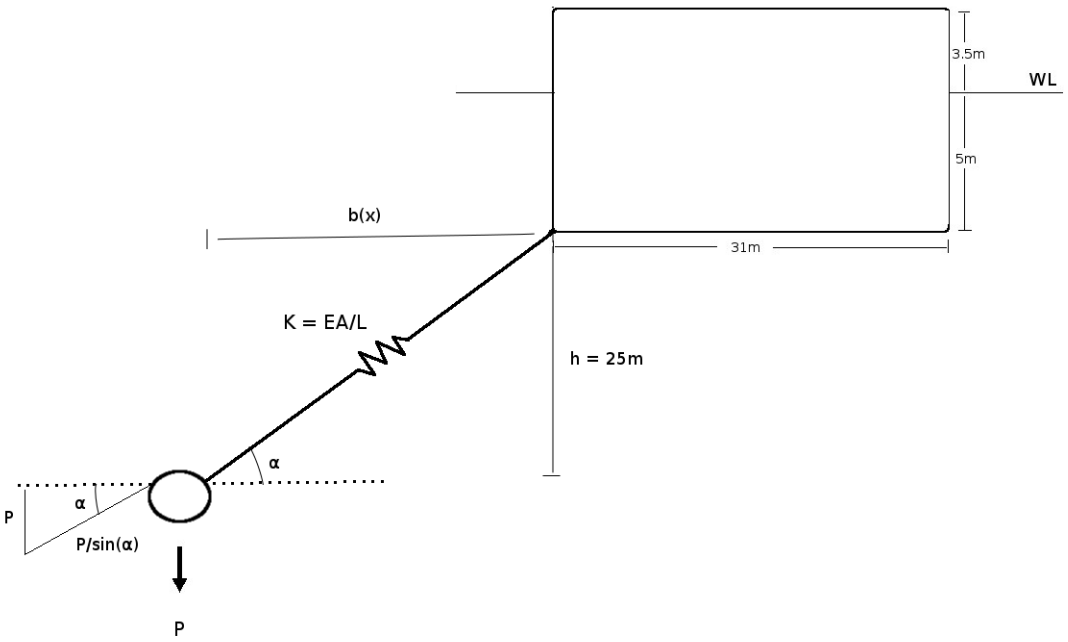

Figure 3.2: The crossbar connected to the pontoon and main pipe modelled as a spring.

So the vertical stiffness from the bars is given by $K_z = \frac{EA}{L} * sin^2(\alpha)$. The angle α will vary along the length of the artificial seabed.

3.3 Calculating the vertical stiffness from each mounting bar

As shown in the previous section, the artificial seabed will get a vertical stiffness contribution from each mounting bar given by $K_z = \frac{EA}{L} * sin^2(\alpha)$. The mounting bars specified by Reinertsen are of the same cross section area and material, and the stiffness will only vary with the length and angle of the bars along the x-axis.

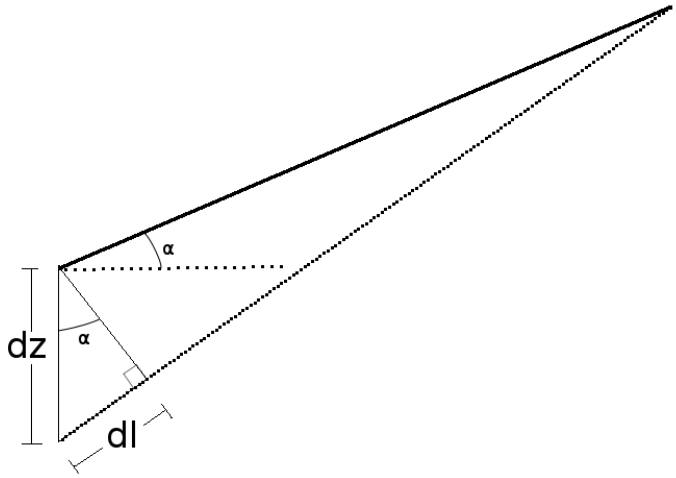

Figure 3.3: The geometric relation of the spring before and after the vertical displacement of the main pipe.

3.3.1 Finding the length and angle of each mounting bar

It can be seen from Figure 3.2 that the angle α and length L are related to the horizontal distance b(x) and vertical distance h from the pipe to the mounting point on the pontoon. The vertical distance h is assumed to be constant and approximately 25m. This is found by substracting the draught of the pontoons (5m) with the distance from the main pipes to the surface (30m). The horizontal distance b(x) will vary along the x-axis because of the curvature of the artificial seabed in the xy-plane as seen in Figure 2.2. The values of b(x) are found from a RIFLEX analysis of the artificial seabed without current. The geometric values of the bars connected to the cylindrical pontoons on one floating bridge module are presented in Table 3.1.

It should be noted that the corresponding values for the other floating bridge module will be the same as in Table 3.1, except that the x-coordinates will be negative. This is due to the symmetry of the complete construction.

Table 3.1: Geometric values for the different pontoons

distance from land[m]	x-coordinate[m]	b(x)[m]	h[m]	L[m]	α[deg]
106	1696	337.37	25	338.3	4.24
212	1590	297.18	25	298.2	4.81
318	1484	257.62	25	258.8	5.54
424	1378	220.74	25	222.2	6.46
530	1272	189.82	25	191.5	7.50
636	1166	159.49	25	161.4	8.91
742	1060	132.33	25	134.7	10.70
848	954	109.81	25	112.6	12.83
954	848	87.92	25	91.4	15.87

3.3.2 Calculating vertical stiffness

In Section 3.2 the vertical stiffness from one bar was found to be $K_z = \frac{EA}{L} * sin^2(\alpha)$. The youngs module and cross section area of the bars are taken from Table 2.5. L and α are found from Table 3.1. The vertical stiffness from the cross bars connected to the cylindrical pontoons is calculated and presented in Table 3.2.

Table 3.2: Calculated vertical stiffness from the cross bars connected to the cylindrical pontoons.

distance from land[m]	E $[GPa]$	A $[m^2]$	L$[m]$	$\alpha[deg]$	$K_z[\frac{kN}{m}]$
106	207	0.009	338.3	4.24	30.4
212	207	0.009	298.2	4.81	44.4
318	207	0.009	258.8	5.54	68.0
424	207	0.009	222.2	6.46	108.0
530	207	0.009	191.5	7.50	168.0
636	207	0.009	161.4	8.91	280.1
742	207	0.009	134.7	10.70	482.6
848	207	0.009	112.6	12.83	825.1
954	207	0.009	91.4	15.87	1543.3

As described in Section 2.2.2, the tunnel is connected to six pontoons. The artificial seabed is not connected directly to these pontoons. Based on

information from Marit Reiso at Reinertsen (ref), the tunnel will be connected to the floating bridge with some cross bars. It is however not decided in detail how this configuration will be yet. It is therefore assumed that the number of cross bars will be six on each side of the tunnel. This assumption is based on the fact that the cylindrical pontoons are connected to the artificial seabed by one crossbar on each side. The cross bars in connection with the tunnel are further assumed to be at the same x-coordinate as the pontoons in connection with the tunnel. By using this assumption the vertical stiffnesses from the cross bars connected to the tunnel are calculated to be as shown in Table 3.3.

Table 3.3: Calculated vertical stiffness from the cross bars connected to the tunnel.

distance from land[m]	E $[GPa]$	A $[m^2]$	L$[m]$	$\alpha[deg]$	$K_z[\frac{kN}{m}]$
1142	207	0.009	65.4	18.74	2979.0
1512	207	0.009	24.8	14.01	4462.9
1652	207	0.009	18.9	9.11	2494.4

The calculations in Table 3.3 are based on the assumption that the cross bars are mounted to the bottom of the tunnel cross section. The vertical position of the mounting point on the tunnel has been based on the assumed vertical coordinates shown in Table 3.4.

Table 3.4: Estimated vertical position of the tunnel at each mounting point.

Pontoon x-coordinate [m]	Z-position of tunnel bottom [m]
660	9
290	24
150	27

The values in Table 3.4 are based on the assumption that the tunnel is just below the water level where the first pontoon is. The height of the tunnel is 9m, hence the distance from the artificial seabed to the bottom of the tunnel will be 30m - 9m = 21m, at this point. The two other values are based on a report by Reinertsen (Reinertsen, 2014, figure 16).

It should be noted that the vertical stiffness will be the same on both sides of the artificial seabed due to the symmetric properties of the construction.

Chapter 4

The theory of VIVANA and vortex induced vibrations

The theory in this chapter is partly based on the project thesis by Grevstad (2014). The first sections will give an introduction to the general theory of vortex induced vibrations (VIV). After that, the theory behind the software VIVANA, developed at MARINTEK, is discussed.

4.1 Vortex induced vibrations

Vortex induced vibrations (VIV) are oscillations of slender structures such as risers, pipe lines or anchor lines caused by currents (Larsen, 2010). The flow around the structure causes vortices to be released from the separation point (Fjeld, 2013). The position of the separation point varies with time, causing a so called vortex street. This is illustrated in Figure 4.1.

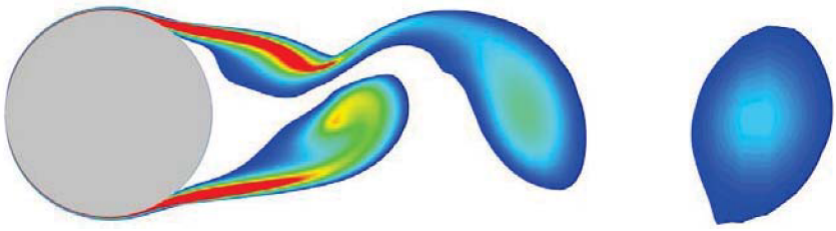

Figure 4.1: Illustration of the vortex street behind a 2D circular cylinder (Fjeld, 2013).

The dynamic lift and drag forces cause oscillations of the structure (Larsen, 2010). The oscillations occur both in the direction tangential to the velocity of the incoming current (in-line oscillations) and normal to the velocity (cross-flow oscillations). The in-line (IL) oscillation has twice the frequency of the cross-flow (CF) oscillation under the same conditions.

VIV is a resonance problem. For a heavy cylinder resonance will occur when the following apply:

$$f_v \approx f_0 \tag{4.1}$$

Where f_v is the vortex shedding frequency for a fixed cylinder and f_0 is the eigenfrequency in still water (Larsen, 2010). For a light cylinder, this is not the case. That is because the added mass will be of significant size compared to the size of the structural mass.

4.1.1 Added mass

Added mass is the component of the hydrodynamic force that is in phase with the acceleration of the structure. It is common practise to separate the added mass from the external force and add it to the left hand side of the dynamic equilibrium equation. This is shown in the following equation taken from the VIVANA theory manual (Passano et al., 2014a)

$$-\omega^2(M_s + M_H)x + i\omega(C_s + C_H)x + Kx = X_L \tag{4.2}$$

Where M_s is the structural mass matrix and M_H the added mass matrix. The eigenfrequency in still water is affected by the added mass in still water (Larsen, 2010). As the added mass varies with the oscillation frequency of the structure, the response frequency will be different than the eigenfrequency in still water (Larsen, 2010). Therefore the system is at resonance when the vortex shedding frequency is close to, but not exactly, the eigenfrequency in still water. Added mass will have a larger effect on a light structure than a heavy structure. This is because the added mass will be a smaller portion of the total mass for a heavy structure, than for a light structure. The oscillating frequency of a rigid cylinder in uniform current is given by (Larsen, 2010):

$$f_{osc} = \frac{1}{2\pi}\sqrt{\frac{k}{m + m_a}} \tag{4.3}$$

Where m is the structural mass, m_a the added mass, and k the stiffness of the cylinder. Equation 4.3 shows that if m_a is relatively small compared to m, the oscillating frequency will be little affected by added mass. That means for a heavy structure the response frequency will be approximately the same as the eigenfrequency of the structure. This can be seen from Figure 4.2

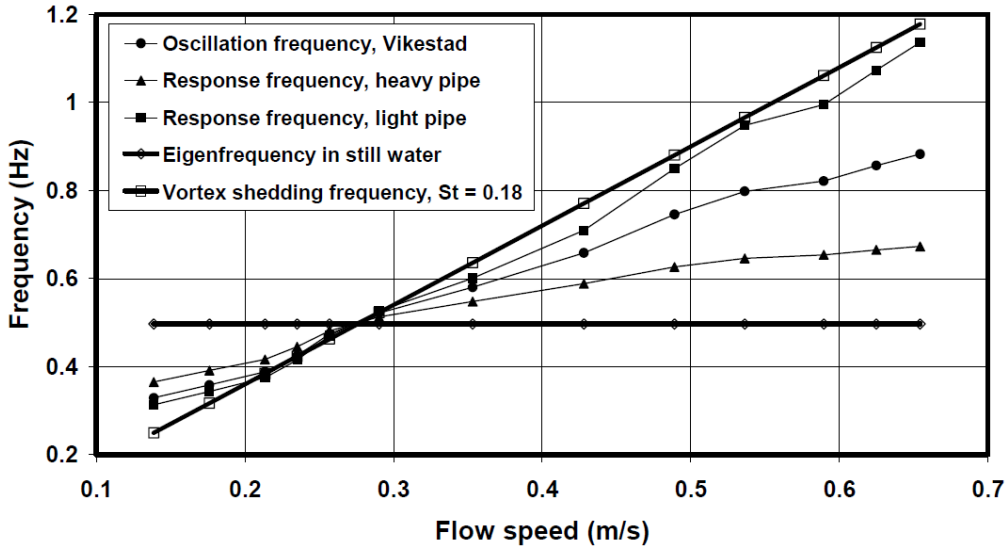

Figure 4.2: Oscillation frequency as a function of flow speed for three different pipes (Larsen, 2010).

Figure 4.2 shows that the response frequency will be a compromise between the eigenfrequency in still water (horizontal line), and the vortex shedding frequency for a fixed cylinder (solid straight line).

4.1.2 The excitation force

The excitation force is the component of the hydrodynamic force in phase with the velocity of the oscillations (Larsen, 2010). When the excitation force is positive, energy is transfered from the fluid to the structure. This causes excitation of the structure. When the excitation force becomes negative, energy is transferred from the structure to the fluid, which gives damping.

4.1.3 A self-limiting process

VIV is considered a self-limiting process (Larsen, 2010). This is because when the oscillations reach a certain amplitude, the excitation force will become negative and hence cause damping. The amplitudes at where the excitation force changes from positive to negative will vary with the nondimensional frequency. This can be seen from the contour plot of the excitation coefficients for a circular cylinder, presented in Section 4.3.2.

4.2 Important nondimensional parameters in VIV

In this section some dimensionless parameters that are of interest when calculating VIV will be discussed.

4.2.1 The Reynolds number

The Reynolds number is given by:

$$Re = \frac{U_N \cdot D_H}{\nu} \tag{4.4}$$

Where U_N is the normal component of the flow velocity (relative to the structure), D_H the hydrodynamic diameter and ν the kinematic viscosity. The kinematic viscosity is temperature dependent (Faltinsen, 1990). VIV experiments are normally done in the sub-critical flow regime which is from 300 to 300 000 Re (Larsen, 2010). In the nature however, one would expect very high Reynolds numbers ($>$ 300 000 Re). The results found from the experiments in the lower turbulent flow regimes are however considered conservative and can therefore be used when calculating VIV at higher Reynolds number.

4.2.2 The Strouhal number

The Strouhal number is given by:

$$St = \frac{f_v \cdot D_H}{U_N} \tag{4.5}$$

where f_v is the vortex shedding frequency of the stationary cylinder case. The Strouhals number is a function of the Reynolds number (Larsen, 2010). However for a circular cylinder a Strouhals number of 0.2 is commonly used. Rearranging Equation 4.5 gives:

$$f_v = \frac{St \cdot U_N}{D_H} \tag{4.6}$$

Which shows that the vortex shedding frequency (f_v) will increase for increasing current velocity U_N (Larsen, 2010).

4.2.3 The nondimensional frequency

The nondimensional frequency is given by:

$$\hat{f} = \frac{D_H \cdot f_{osc}}{U_N} \tag{4.7}$$

Where f_{osc} is the oscillation frequency of the structure. The nondimensional frequency is important in the experiments described in Chapter 5.

4.2.4 The nondimensional amplitude

The nondimensional amplitude is simply defined as A/D, where A is the amplitude and D the hydrodynamic diameter. The nondimensional amplitude is used in the forced vibrations experiments described in Chapter 5.

4.3 VIVANA

VIVANA is a software developed at MARINTEK that calculates VIV on slender structures (Passano et al., 2014a). It is based on empirical models from experiments in a Reynolds number range of order 10^4. Two of the main tasks of VIVANA are to find the possible response frequencies, and calculate the fatigue from the active response frequencies. This will be discussed in the following sections.

4.3.1 Calculation of the response frequencies

VIVANA calculates the response frequencies that can be excited on a model under the given conditions. As mentioned in Section 4.1.1, the response

frequencies will be different from the eigenfrequencies of the structure in still water, because the added mass will vary with the oscillating frequency. The oscillating frequency will on the other hand vary with the added mass. Hence an iteration procedure is needed to find the resulting response frequencies.

VIVANA uses data from Gopalkrishnan to find the added mass coefficient for a given nondimensional frequency (Passano et al., 2014a). The added mass coefficients are actually a function of both the nondimensional frequencies ($\hat{f}$) and amplitudes A/D. However VIVANA supports only one added mass coefficient per nondimensional frequency. Figure 4.3 shows how the CF added mass curve is found from a contour plot based on the results of Gopalkrishnan (Passano et al., 2014a). The added mass values are selected at a constant A/D ratio of 0.5. The resulting added mass curve as a function of the nondimensional frequencies is shown in Figure 4.4.

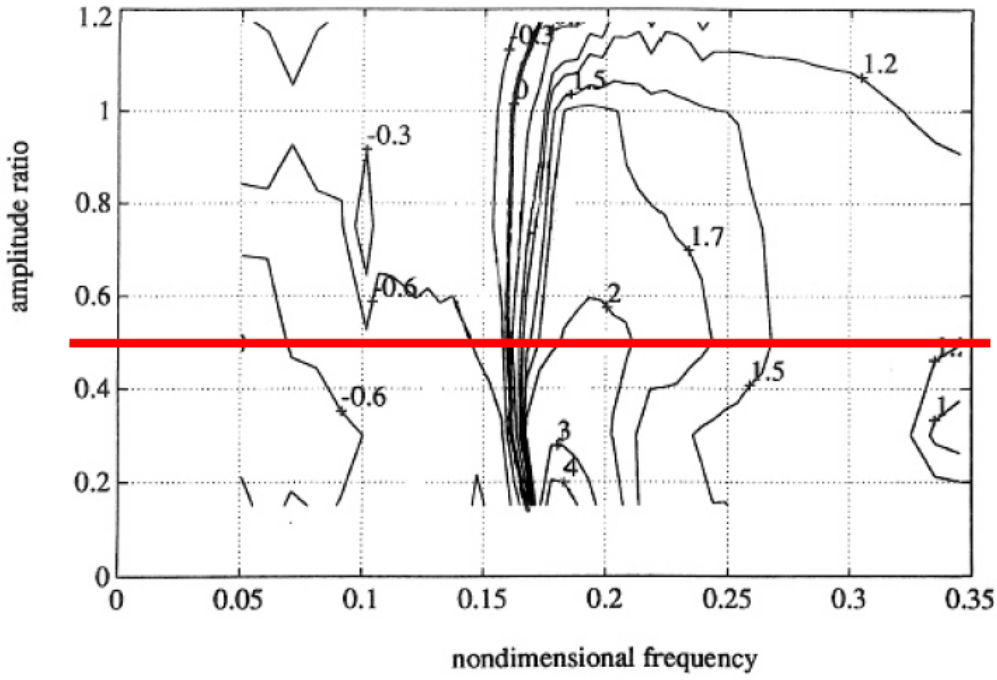

Figure 4.3: The figure shows how the CF added mass curve is found from a contour plot based on the results of Gopalkrishnan

Based on these data the potential response frequencies are found from an iteration process (Passano et al., 2014a):

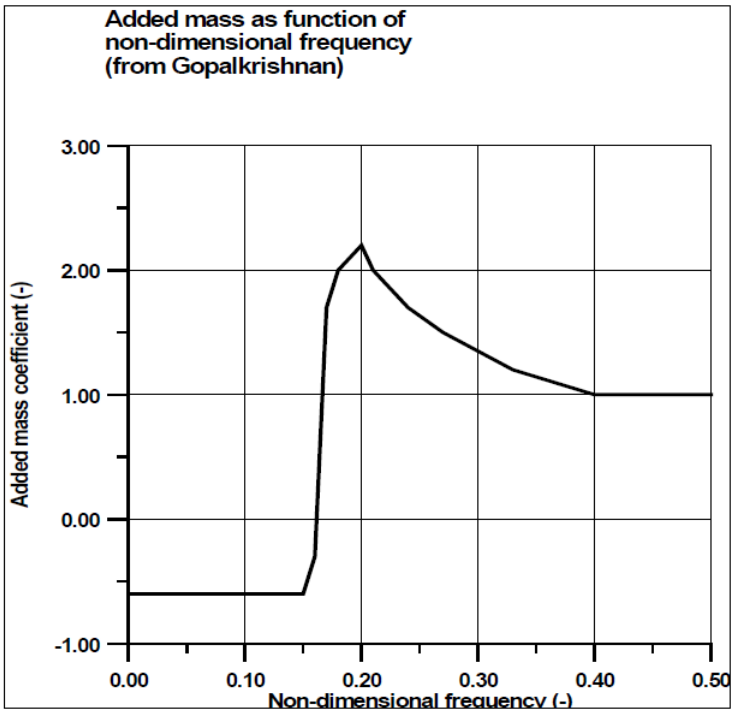

Figure 4.4: The default added mass curve used in VIVANA (Passano et al., 2014a).

1. First the eigenfrequency in still water is calculated using the added mass value in still water.

2. The response frequency candidate is assumed to be the same as the eigenfrequency in still water.

3. The nondimensional frequency is calculated from the response frequency candidate, and corrected if the Strouhals number is different from 0.2.

4. The added mass for the calculated nondimensional frequency is found using the data from Gopalkrishnan.

5. The new eigenfrequency is calculated using the new value of the added mass found in the previous step.

6. Check if the new eigenfrequency is close enough to the response frequency candidate in step 2. If not the iteration will continue from step 3 again using the new eigenfrequency.

The iteration process above is done for each eigenfrequency that has a chance of giving resonance (Passano et al., 2014a). It is also possible to specify data from other experiments than from Gopalkrishnan in VIVANA.

4.3.2 Active response frequencies

When the potential response frequencies are found, VIVANA will calculate which of the frequencies that give excitation (Passano et al., 2014a). The frequencies that give excitation are called active response frequencies. The frequencies will give excitation if the excitation coefficient is positive. For a circular cylinder in pure CF motions, the CF excitation coefficients are positive when the nondimensional frequency is between approximately 0.125 and 0.3 as shown in Figure 4.5 (Passano et al., 2014a).

The nondimensional frequency is calculated for each response frequency at each element along the structure (Passano et al., 2014a). The length along the structure that gives a positive excitation coefficient for a given response frequency is called the excitation zone. Each response frequency will have its own excitation zone. The excitation zones may however overlap.

4.3.3 Excitation coefficient curves

Figure 4.6 shows the excitation coefficient curve that VIVANA builds for each nondimensional frequency ($\hat{f}$) in the excitation region. The values between the points A,B and C are found by interpolation using two second order polynomials (Passano et al., 2014a).

Point A in Figure 4.6 refers to the value of the excitation coefficient where $A/D = 0$. The location of point B is found from the nondimensional amplitude were C_e is at maximum and the magnitude of this value. Point C represents the A/D ratio were the excitation coefficient is zero.

4.3.4 Ranking the response frequencies

When the excitation zones are calculated, VIVANA needs to determine which response frequency that dominates the response. This is done by calculating

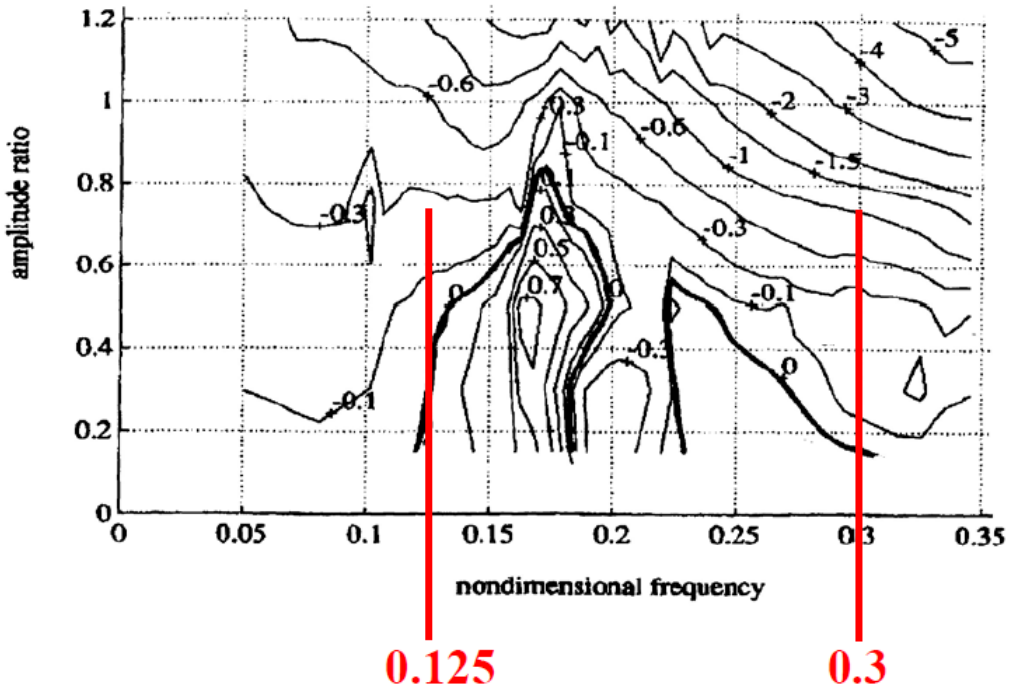

Figure 4.5: The CF excitation coefficients for a circular cylinder in pure CF motion. The excitation area is shown as a bold black line. (Passano et al., 2014a)

an excitation parameter using Equation 4.8 and ranking the frequencies based on this value (Passano et al., 2014a):

$$E_i = \int_{L_{e,i}} U_N^3(s) D_H^2(s) (\frac{A}{D})_{C_e=0} ds \tag{4.8}$$

Where E_i is the excitation parameter. U_N is the normal velocity of the flow, D_H the hydrodynamic diameter and $(\frac{A}{D})_{C_e=0}$ is the nondimensional amplitude where the excitation parameter (C_e) is 0. The response frequency with the highest excitation parameter ranks first. It should be noted that for a uniform current, U_N and D_H will be the same for all response frequencies and hence $(\frac{A}{D})_{C_e=0}$ will be the decisive parameter.

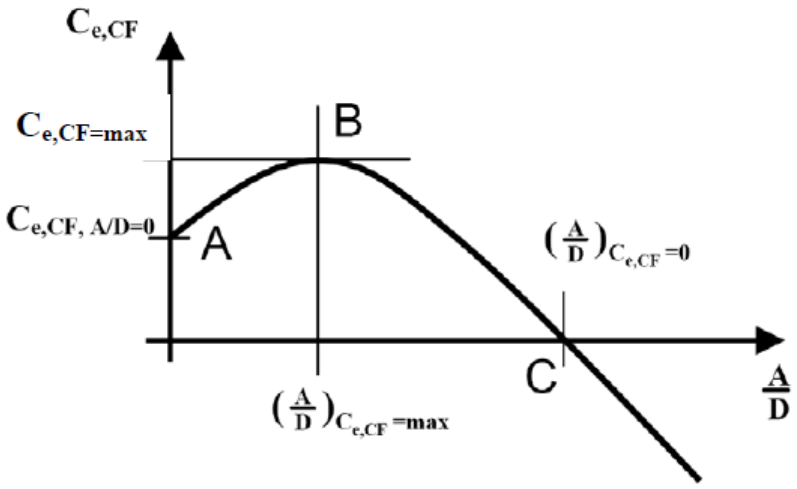

Figure 4.6: The CF excitation coefficient curve used in VIVANA (Passano et al., 2014a).

4.3.5 Time and space sharing

When the excitation zones and parameters are found from all the response frequencies, the fatigue damage can be calculated based on the total response from all the frequencies. The total response can be calculated using a space sharing or time sharing method. Space sharing is the default method in VIVANA.

In space sharing multiple response frequencies can act simultaneously. The frequency with the highest rank will occupy its full excitation zone along the structure. The part of the structure that is not occupied by this frequency is then divided among the other response frequencies based on rank. Figure 4.7 illustrates the space sharing method.

In the time sharing method the response frequencies inside the excitation region will all be active but at different times. One frequency is only active for a certain time interval before another frequency takes over. The duration of each frequency is determined by the excitation parameter described in Section 4.3.4.

The excitation zones of the different response frequencies may overlap in the time sharing method, since they are not active simultaneously. Figure 4.8 illustrates the time sharing method.

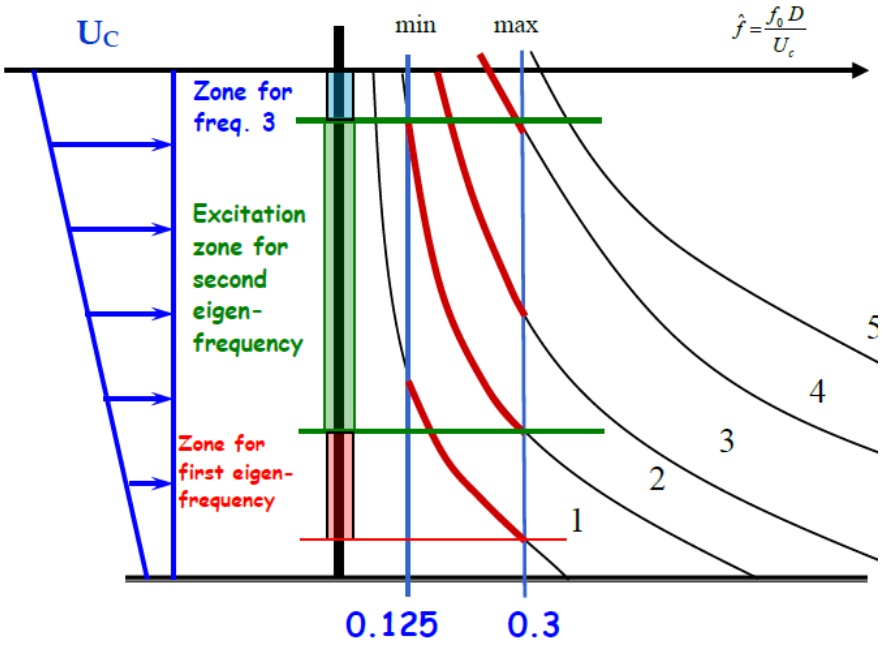

Figure 4.7: An illustration of the space sharing method (Passano et al., 2014a). Each frequency is operating simultaneously at different sections of the structure.

4.3.6 Strouhals number as a function of Reynolds number

The Strouhals number is a function of Reynolds number (Larsen, 2010). VIVANA uses the Strouhals number curve shown in Figure 4.9 as default.

The default Strouhals number curve is valid for circular cylinders with some roughness (Passano et al., 2014a). A custom Strouhals number curve may be specified in VIVANA by the end-user.

4.3.7 Fatigue damage and fatigue life

One method in VIVANA to calculate the accumulated fatigue damage is by using the following equation (Passano et al., 2014a):

$$D_{iel,iend,ipt} = \sum_{i=1}^{N_{\Delta\sigma}} \frac{n_{i,year,iel,iend,ipt}}{N_i} \tag{4.9}$$

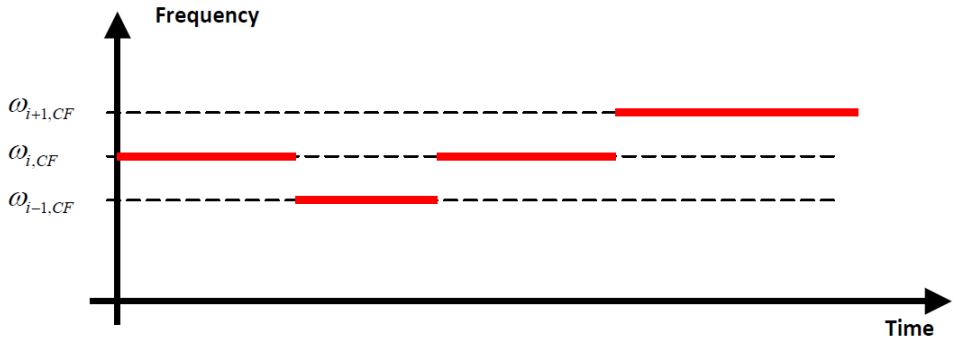

Figure 4.8: An illustration of the time sharing method (Passano et al., 2014a).

N_i is the number of cycles to failure for stress cycle i wich is calculated from the S-N curve data configured in VIVANA (Passano et al., 2014a). $n_{i,year,iel,iend,ipt}$ is the total number of cycles for $\Delta\sigma_i$ during a year. $\Delta\sigma_i$ are the stress ranges.

It should be noticed that the accumulated fatigue damage ($D_{iel,iend,ipt}$) is the inverse of the fatigue life presented in the VIVANA calculations.

For more information on how VIVANA does fatigue calculations it is referred to the VIVANA manual.

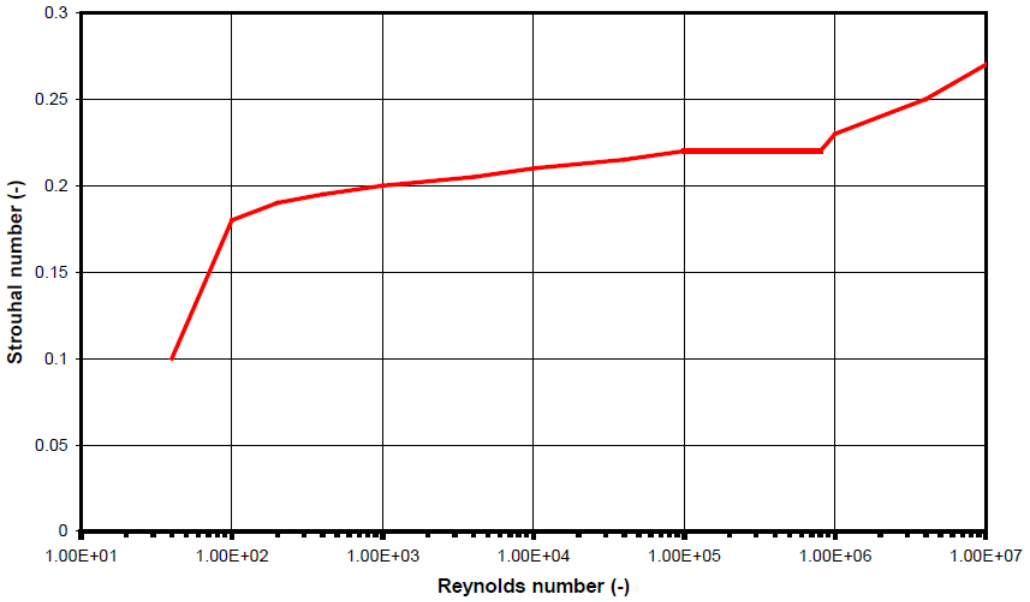

Figure 4.9: The default Strouhals number curve used in VIVANA (Passano et al., 2014a).

Chapter 5

Model experiments

In Chapter 2 it was described how the bundles that make the artificial seabed each consist of 3 pipes. An illustration of this was shown in Figure 2.3. When calculating VIV on the artificial seabed, hydrodynamic data for these bundles are needed in order to give realistic results. To find these hydrodynamic data, model experiments were done in the Marine Cybernetics Laboratory (MC-lab) at NTNU (NTNU, 2015). This chapter describes how these experiments were done and the results from them. The experiments were done in week 14 and 15, 2015.

5.1 Experimental setup

The experiments were done using forced vibrations, with given nondimensional amplitudes and frequencies. This section will describe how the apparatus was set up to accomplish these experiments.

5.1.1 About the bundle model

The bundle model was made using three pipes in aluminium. The pipes were fabricated to be in direct contact with each other (see Figure 2.3) after advice by Marit Reiso at Reinertsen (Reiso, 2015).

The properties of the bundle model are shown in Table 5.1.

Table 5.1: Bundle model properties

Property	Value
Length of bundle	$2.0m$
Mass of bundle	$4.655kg$
Outer diameter of one pipe	$0.05m$
Inner diameter of one pipe	$0.047m$
Hydrodynamic diameter of bundle	$0.107735m$
Area of void between the pipes	$1.0 \cdot 10^{-4}m^2$

5.1.2 Apparatus

The MC-lab contains a tank of dimensions $40m \cdot 6.45m \cdot 1.5m$ (NTNU, 2015). The tank is equipped with a towing carriage with a mounted 5 degrees of freedom motion simulator (Aronsen, 2007). An illustration of the experimental setup is shown in Figure 5.1 and 5.2. The bundle model was constructed with holes on each side to allow water to fill the inside void. This was done to reduce the buoyancy from the pipes. Circular plates were mounted at each end of the bundle model to reduce 3D effects.

The bundle model was connected to a shaft and bearing (including a cylinder) on both sides which in turn were connected to the force sensors. These force sensors were mounted to the yoke connected to the motion simulator on the carriage. The yoke was originally built for the forced vibrations experiments done by Hidetaka Senga on two cylinders with helical strakes (Senga & Larsen, 2014).

Some important properties of the experimental setup are shown in Table 5.2.

Table 5.2: Important properties of the experimental setup.

Property	Value
Total mass on the force sensors (including water)	$20.765kg$
Towing speed	$0.2m/s$
Reynolds number	$2.0 \cdot 10^4[-]$

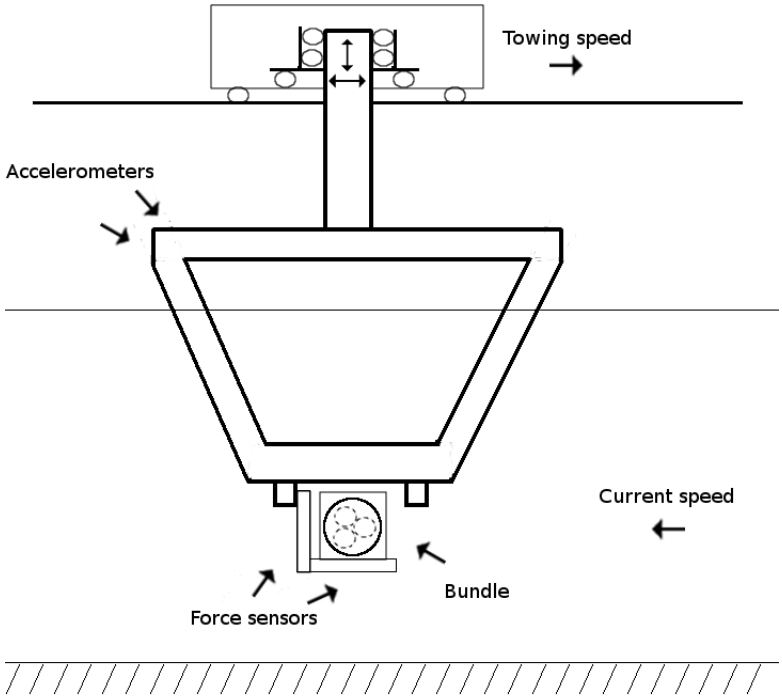

Figure 5.1: The apparatus as seen from starboard side.

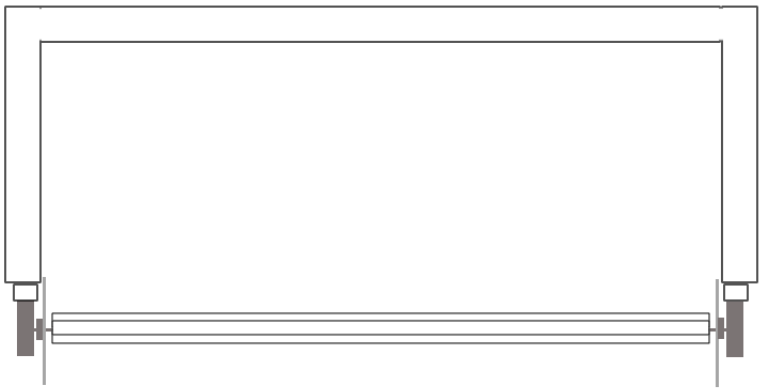

Figure 5.2: Front view of the apparatus.

5.1.3 Coordinate system

The coordinate system of the apparatus is shown in Figure 5.3.

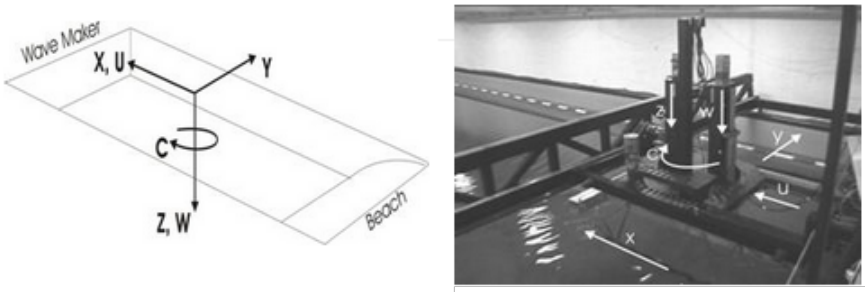

Figure 5.3: Coordinate system of the MC-lab (NTNU, 2015).

The left side when heading towards the positive x-direction will be referred to as the port side and hence the opposite side as the starboard side. This may seem obvious, but the carriage was run in both positive and negative x-direction (see Section 5.1.7) which may lead to confusion.

It should be noted that when calculating the hydrodynamic coefficients the coordinate system used had the z-axis pointing upwards, and the x-axis was relative to the current direction. This is described more in Section 5.5.

5.1.4 Force sensors

A total of four strain gauge force sensors were used in the experiments. The sensors were produced by Hottinger. Two and two sensors were mounted orthogonal and mounted to the yoke as shown in Figure 5.1. The force sensors were numbered 8600-8603 and the position of each sensor is shown in Table 5.3

Table 5.3: Position of the force sensors.

Force sensor number	Side	Alignment
8600	Starboard	Horizontal
8601	Port	Vertical
8602	Port	Horizontal
8603	Starboard	Vertical

Figure 5.1 shows how one force sensor on each side was vertically aligned

while the other was horizontally aligned. The vertically aligned sensors measured the forces in IL direction while the horizontally aligned sensors measured the forces in CF direction. The total force in CF direction was calculated by adding together the values from the two horizontal force sensors and multiplying by a calibration factor. The same method was done in IL direction using a different calibration factor. The calibration factors used were the same as Hidetaka Senga used under his experiments.

Table 5.4: Calibration factors used in the experiments.

Force direction	Calibration factor
IL	-67.36
CF	-67.93

The CF and IL forces were tested by applying a 5kg weight in each direction. This is described in detail in the uncertainty analysis in Section 5.7.

5.1.5 Motion sensors

Two type of motion sensors were used. These were accelerometers and string potentiometers. The accelerometers were mounted on the top-back of the yoke in vertical and horizontal direction as shown in Figure 5.1. The string potentiometers were mounted in two directions between the yoke and carriage. The accelerometers were calibrated against the gravity constant ($9.81 m/s^2$) while the string potentiometers were factory calibrated.

5.1.6 Data acquisition

All the sensors were connected to an amplifier by cables. The amplifier was of the Hottinger MGC+ type. The data was sampled at 100Hz and filtered with a 10Hz filter. The computer software Catman was used to record and save the data. The channel numbering was changed after run 75, on Wednesday 08.04.2015 at approximately 10:00 a.m. This was due to the mounting of an IL string potentiometer which was not needed in the previous runs. The two channel lists used are shown in Table 5.5. "Ch. list 1" refers to the channel numbering used before run 75, while "Ch. list 2" refers to the channel numbering after run 75.

Table 5.5: Data channels from the experiments.

Description	Ch. list 1	Ch. list 2	Unit
Time device	1	1	[s]
IL movement (string potentiometer)	na	2	$[m]$
CF movement (string potentiometer)	2	3	$[m]$
CF acceleration	3	4	$[m/s^2]$
IL acceleration	4	5	$[m/s^2]$
Force sensor 8603	5	6	$[V]$
Force sensor 8600	6	7	$[V]$
Force sensor 8602	7	8	$[V]$
Force sensor 8601	8	9	$[V]$
Carriage x-position	9	10	$[m]$
Input CF displacement	10	11	$[m]$
Carriage speed in x-direction	11	12	$[m/s]$
Total IL force	12	13	$[N]$
Total CF force	13	14	$[N]$
Input IL displacement	na	15	$[m]$

5.1.7 Bundle orientations

The hydrodynamic forces acting on the bundle are depending on the orientation of the bundle relative to the current direction. It was therefore decided to do experiments with three orientations. The orientations were named Orientation 1, Orientation 2 and Orientation 3 as shown in Figure 5.4.

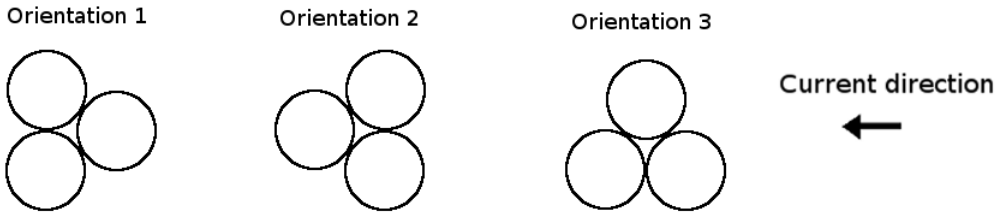

Figure 5.4: Numbering of the three orientations.

The bundle was initially mounted so that Orientation 1 was achieved by running the carriage in positive x-direction (see Figure 5.3). Orientation 2 was achieved by changing the reference position of the carriage to be at the opposite side of the tank, and running the carriage in the negative x-

direction. It was hence not necessary to do any physical modifications of the setup when testing Orientation 1 and 2. When testing Orientation 3 on the other hand, the bundle had to be rotated 90 degrees. A level was used to make all the orientations as correct as possible. The uncertainty in the configuration of the orientations is described in the uncertainty analaysis (see Section 5.7.

5.2 Calculating geometric properties of the bundle

5.2.1 The hydrodynamic diameter

The hydrodynamic diameter used in the experiments was $D_H = 0.107735m$ as previously shown in Table 5.1. Choosing what value to be used as the hydrodynamic diameter for the bundle model was not obvious. Two options were considered. The first option was to make a circular cylinder with the same cross section area as the cross section of the bundle. The hydrodynamic diameter would then be the diameter of that circle. The other option was to make a circle with a circumference going around the bundle cross section, as shown in Figure 5.5. This was the chosen option.

Figure 5.5 shows the bundle cross section and the circle used for calculating the hydrodynamic diameter. The figure is based on the assumption that the pipes are in direct contact with each other. Hence the equations derived from the geometries in the figure will be based on the same assumption.

The radius of the outer circle is of the same length as OP and is referred to as the hydrodynamic radius. The hydrodynamic radius is longer than the diameter of one pipe. To find the length of the hydrodynamic radius, the triangle $\triangle abc$ with vertices in the origin of each pipe, is needed. The hydrodynamic radius will then be given by equation 5.1.

$$R_{hydro} = OP = r + ad - Od \tag{5.1}$$

Where OP is the distance between point O and P, r is the outer radius of one pipe, and ad is the distance from point a to d. Od is the distance from point O to point d.

From Figure 5.5 it can be seen that ad can be found by some simple trigonometry:

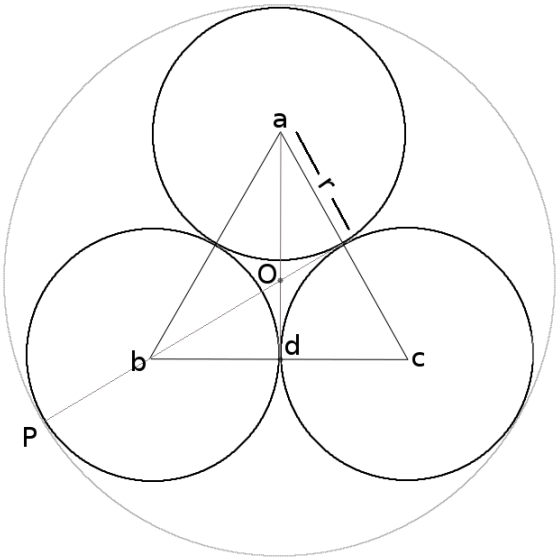

Figure 5.5: The geometry used for calculating the hydrodynamic diameter.

$$ad = \sqrt{(2r)^2 - r^2} \tag{5.2}$$

The distance Od can be found by using the fact that the triangles $\triangle bOd$ and $\triangle adc$ are similar.

$$\frac{Od}{r} = \frac{dc}{ad} = \frac{r}{\sqrt{(2r)^2 - r^2}} \tag{5.3}$$

Solving for this gives the following value of Od:

$$Od = \frac{r}{\sqrt{3}} \tag{5.4}$$

The hydrodynamic radius then becomes:

$$R_{hydro} = r + ad - Od = r + r\sqrt{3} - r\frac{1}{\sqrt{3}} = 2.1547 \cdot r \tag{5.5}$$

Equation 5.5 is also used to calculate the hydrodynamic diameter of the full scale bundle model.

Inserting the value of r from the bundle model geometry (see Table 5.1) the hydrodynamic diameter becomes:

$$D_{hydro} = 2 \cdot R_{hydro} = 2.1547 \cdot D_{pipe,model} = 2.1547 \cdot 0.05m = 0.107735m \quad (5.6)$$

It should be noted that the hydrodynamic diameter calculated here is based on the assumption that the pipes are in direct contact, as seen in Figure 2.3.

5.2.2 The area between the pipes

It is necessary to find the area of the void between the pipes in the bundle model, located around point O in Figure 5.5. This is because the void is filled with water when doing the experiments. This water contributes to the mass used to calculate the inertia force and should hence be included. The inertia force is substracted from the total measured force to get the hydrodynamic force (see Section 5.6.2). The area of the void is calculated in the following way:

$$A_{void} = A_{\triangle abc} - 3 \cdot \frac{A_{pipe}}{6} \quad (5.7)$$

Where $A_{\triangle abc}$ is the area of $\triangle abc$ and $\frac{A_{pipe}}{6}$ is the area of the part of one pipe inside $\triangle abc$. $A_{\triangle abc}$ can be calculated using:

$$A_{\triangle abc} = \frac{1}{2} \cdot 2r \cdot ad = \frac{1}{2} \cdot 2r \cdot r\sqrt{3} = \sqrt{3}r^2 \quad (5.8)$$

Where equation 5.2 from the previous section has been used to calculate the distance ad.

The area of the void can then be calculated:

$$A_{void} = \sqrt{3}r^2 - 3 \cdot \frac{\pi r^2}{6} = (\sqrt{3} - \frac{\pi}{2})r^2 \quad (5.9)$$

And finally by inserting $r = 0.025m$ (see Table 5.1) the area of the void can be found:

$$A_{void} = (\sqrt{3} - \frac{\pi}{2}) \cdot (0.025m)^2 = 1.0 \cdot 10^{-4}m^2 \quad (5.10)$$

5.3 Test cases

Due to the relatively short time available in the MC-lab, prioritations had to be done. The main focus was to do pure CF tests, and if any available time after that do some combined CF/IL tests. As a result of this the pure CF results are based on more data than the combined CF/IL results.

To begin with, a preliminary test matrix was made. This test matrix is shown in Figure 5.6. The preliminary test matrix was primarely used to locate the borders of the excitation region and plan further test runs based on that information. The excitation region is all the combinations of nondimensional amplitudes and frequencies that give a positive excitation coefficient (Aronsen, 2007). Due to the limited time for the experiments, it was prioritized to find the positive excitation coefficients.

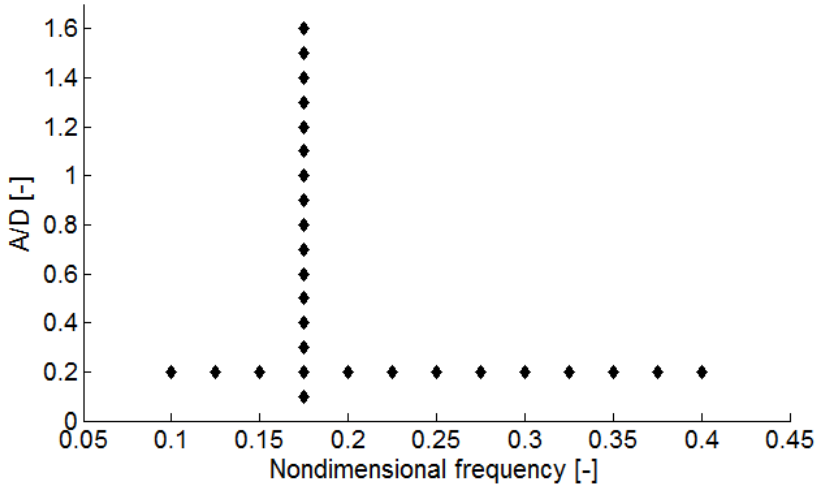

Figure 5.6: The initial test matrix used in the early stage of the experiments.

The carriage was programmed to test each of the cases in the figure above. The programming was done in MATLAB using harmonic motions and a velocity of $U = 0.2m/s$ at all times. This will be described more in detail in Section 5.6.1. Between each run the excitation coefficient and added mass coefficient was found using a post processor (see section 5.6.2). The excitation coefficients from the first tests at $\hat{f} = 0.175$ (the vertical "line" of points in Figure 5.6) turned out to be outside the excitation region. This was in fact the case for all 3 orientations tested (the bundle orientations are

defined in Section 5.1.7). Because of this it was decided not to run all of the tests with $\hat{f} = 0.175$. All of the tests with $A/D = 0.2$ in the preliminary test matrix were however done for all 3 orientations.

5.3.1 Fixed bundle tests

For each orientation, one stationary test was done. This was to find the drag coefficient of the stationary bundle, and the Strouhals number. The fixed bundle tests were of the lowest priority, and only one run was done for each orientation. The results are presented in Section 5.8.

5.3.2 CF tests

The CF tests were of the highest priority in the experiments. As previously mentioned, the test matrix shown in Figure 5.6 was used as a starting point for the pure CF tests in all three orientations. The rest of the test runs were created based on the results from the previous runs. The complete test matrices are presented in the next sections.

Orientation 1

A total of 65 unique pure CF runs were done in Orientation 1. This does not include the repetition runs (see Section 5.3.4). The final test matrix is shown in Figure 5.7.

Orientation 2

In Orientation 2 it was done 56 unique pure CF runs. The final test matrix for Orientation 2 is shown in Figure 5.8.

Orientation 3

In total 35 unique runs were done in Orientation 3. The final test matrix is shown in Figure 5.9.

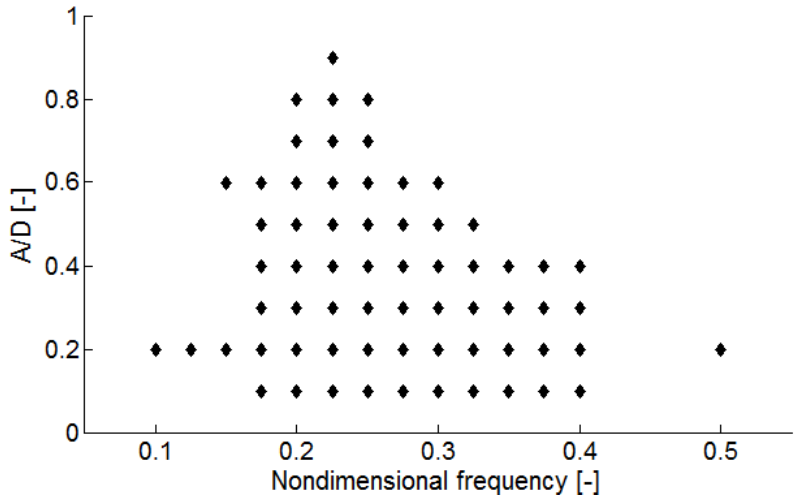

Figure 5.7: The final test matrix for pure CF, Orientation 1.

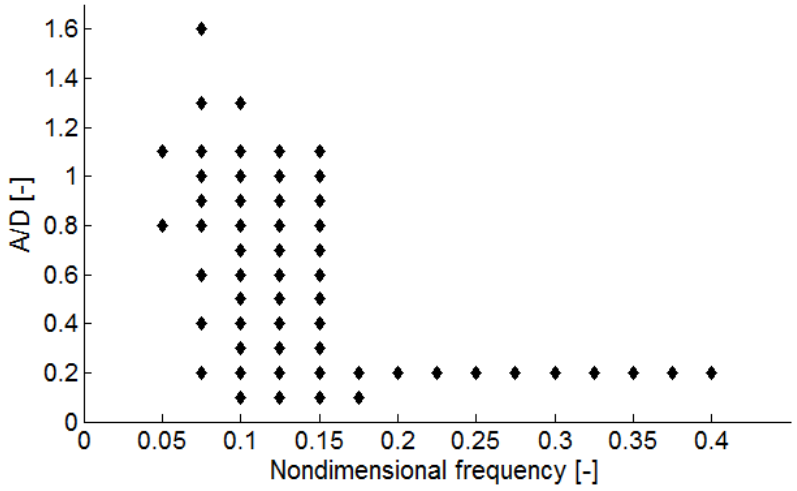

Figure 5.8: The final test matrix for pure CF, Orientation 2.

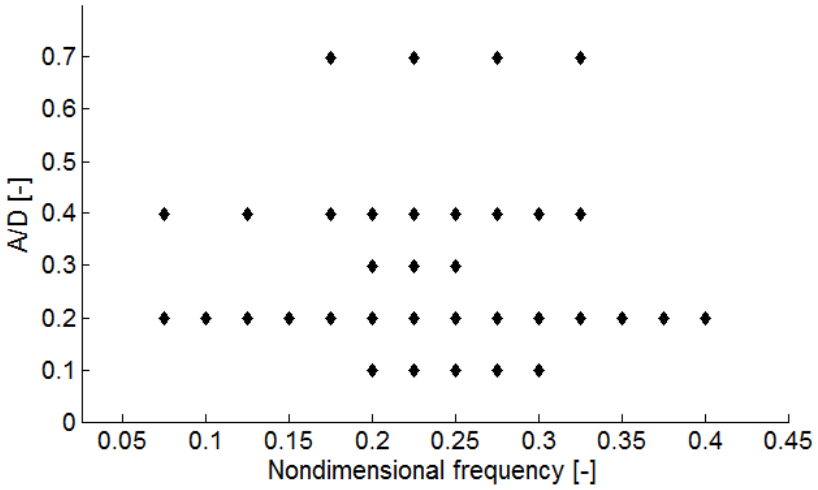

Figure 5.9: The final test matrix for pure CF, Orientation 3.

5.3.3 Combined CF/IL tests

The combined CF/IL motions were programmed using the equations 5.11 and 5.12 taken from Aronsen (2007).

$$CF : z(t) = A_{CF} \cdot cos(2\pi \cdot f_{osc,CF} \cdot t) \tag{5.11}$$

$$IL : x(t) = A_{IL} \cdot sin(2\pi \cdot f_{osc,IL} \cdot t + \alpha) \tag{5.12}$$

It is here used the relations $A_{IL} = 0.5 \cdot A_{CF}$ and $f_{osc,IL} = 2 \cdot f_{osc,CF}$ to limit the number of variables in the experiments. α is the phase angle which is varied. In these experiments it was used $\alpha = 0$ and $\alpha = \pi$ (radians). The orbital paths created from these phase angles are shown in Figure 5.10.

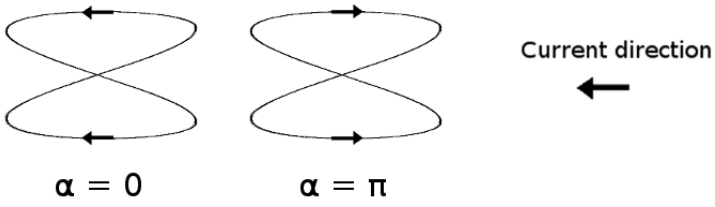

Figure 5.10: The orbital paths resulting from using phase angles $\alpha = 0$ and $\alpha = \pi$

The reason for only testing with two values of α was the limited time for the experiments.

The test matrices used for the combined CF/IL tests were based on the excitation regions found from the pure CF tests. In Orientation 1 and 2, the combined CF/IL tests were all done inside this region. This was because finding the positive excitation coefficients were prioritized. The excitation region in Orientation 3 turned out to be very small, however. Due to this, many of the tests in Orientation 3 were done outside the CF excitation region.

Orientation 1

A total of 32 unique combined CF/IL runs were done in Orientation 1. 16 runs were done with $\alpha = 0$ and another 16 with $\alpha = \pi$. The combined CF and IL test matrix in Orientation 1 is shown in Figure 5.11.

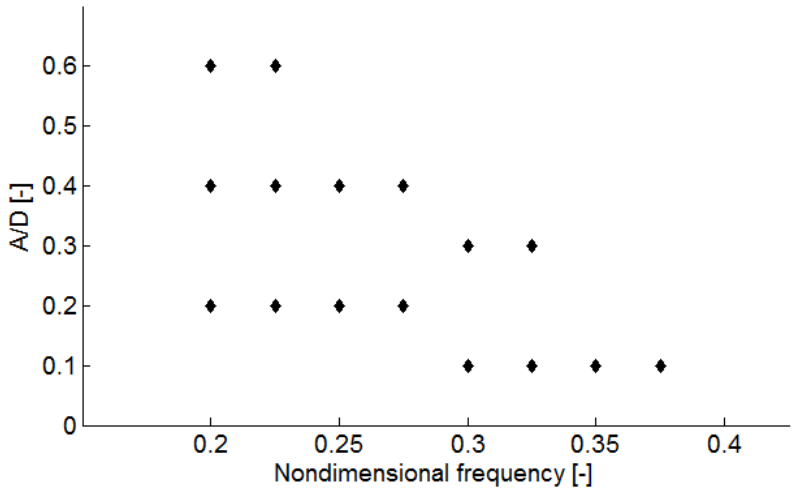

Figure 5.11: The test matrix for combined CF and IL motions, Orientation 1.

Orientation 2

With Orientation 2, 26 unique runs were done. 13 runs with $\alpha = 0$ and 13 with $\alpha = \pi$. The combined CF and IL test matrix for Orientation 2 is shown in Figure 5.12.

Orientation 3

22 runs were done in Orientation 3. 11 runs were done for both $\alpha = 0$ and $\alpha = \pi$. The combined CF and IL test matrix for Orientation 3 is shown in Figure 5.13.

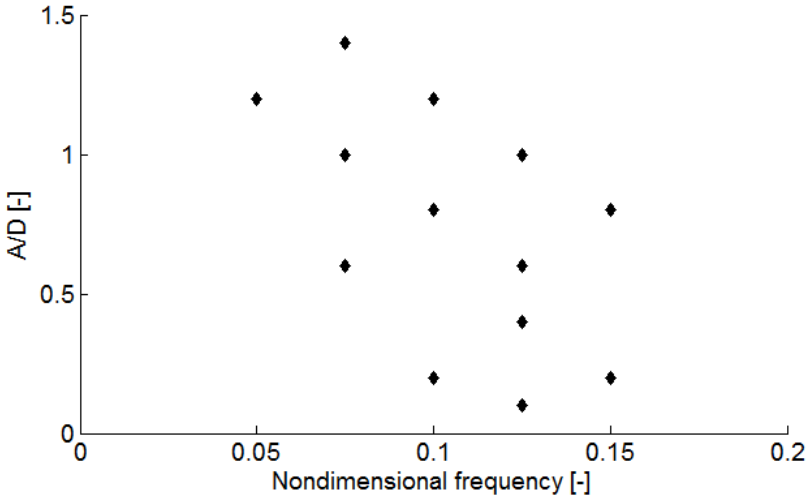

Figure 5.12: The test matrix for combined CF and IL motions, Orientation 2.

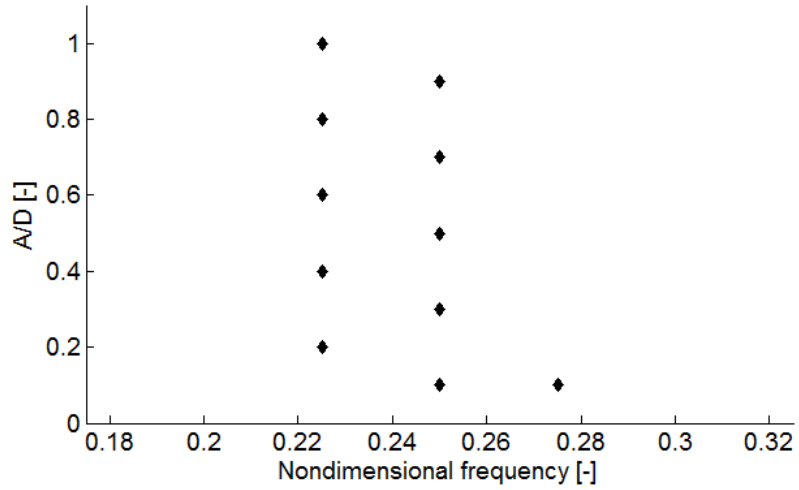

Figure 5.13: The test matrix for combined CF and IL motions, Orientation 3.

5.3.4 Repetition runs

For each orientation, one run was repeated at different times, with the same configuration each time. This was to get data giving insight into the precision (random) errors in the experiments. The repetition runs used a nondimensional frequency and amplitude of $\hat{f} = 0.175$ and $A/D = 0.2$. The number of repetition runs in each orientation are shown in Table 5.6.

Table 5.6: The repetition runs done during the experiments.

Orientation number	Direction	$\hat{f}[-]$	$A/D[-]$	Number of runs
1	CF	0.175	0.2	10
2	CF	0.175	0.2	5
3	CF	0.175	0.2	5

It should be noted that the number of repetition runs were limited due to the short time available in the MC-lab.

5.4 Procedure for each run

Each run in the test matrices described in the previous sections were performed by the following procedure:

- Load a .MCL-file with the given carriage and motion simulator displacements for the relevant run.
- Zero setting all data channels.
- Start the recording of data in the software Catman.
- Run the previously loaded .MCL-file. The carriage will accelerate towards a constant velocity and reach a steady state for the oscillating motions.
- Stop recording in Catman when carriage stops and save the data file to the hard drive.
- Return the carriage to the reference position.
- Start a timer and do a 10 minute countdown. This is to wait for the water to calm down.

The MCL files refered to in the list above are described more in detail in Section 5.6.1.

5.5 Calculation of the hydrodynamic coefficients

This section describes how the hydrodynamic coefficients were calculated. The coordinate system used in the calculations is shown in Figure 5.14. Note that the coordinate system is relative to the current direction, and that the current is going in the positive x direction. The current is going in the opposite direction of the carriage, hence the carriage is going in the negative x-direction. The z-axis is pointing upwards.

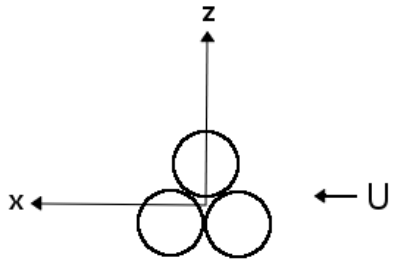

Figure 5.14: Coordinate system used when calculating the hydrodynamic coefficients.

Drag coefficient

The drag coefficient is given by:

$$C_D = \frac{1}{\frac{1}{2}\rho D_H L U_0^2} \frac{\int_t^{t+T} F_{IL}(t)dt}{T} \tag{5.13}$$

Where ρ is the water density in the tank and D_H and L the hydrodynamic diameter and length of the bundle model, respectively. U_0 is the flow velocity, measured from the average towing velocity (see the uncertainty analysis in Section 5.7.6). F_{IL} is the measured force in IL direction and T the number of oscillation periods.

T must be an integer number of periods, to avoid any random errors caused by the integration limits. This is taken care of in the post processor, starting and ending the integration at two different zero-crossing points.

Lift coefficient

The lift coefficient is given by:

$$C_L = \frac{1}{\frac{1}{2}\rho D_H L U_0^2} \frac{\int_t^{t+T} F_{CF}(t)dt}{T} \tag{5.14}$$

Where F_{CF} is the measured force in CF direction.

The lift coefficient is only calculated in Orientation 3 (see Section 5.1.7) since this is the only orientation which is not symmetric about the x-axis (using the coordinate system in Figure 5.14). Hence a resulting lift force may occur.

Dynamic excitation coefficient

The dynamic excitation coefficient is given by:

$$C_{e,IL/CF} = \frac{1}{\frac{1}{2}\rho D_H L U_0^2} F_{hydro,0,IL/CF} sin(\phi) \tag{5.15}$$

$F_{hydro,0,IL/CF}$ is the amplitude of the hydrodynamic force in IL/CF direction. ϕ is the phase angle between the motion of the bundle and the force.

In the post processor, $F_{hydro,0,IL/CF} sin(\phi)$ is estimated using the power transfer method (ref. Aronsen) and is given by:

$$F_{hydro,0} sin(\phi) = \frac{2}{x_0 \omega_{osc}} \lim_{T\to\infty} \frac{\int_t^{t+T} F_{hydro}(t) \cdot \dot{x}(t)dt}{T} \tag{5.16}$$

Where x_0 is the amplitude, ω_{osc} the angular frequency, $F_{hydro}(t)$ the hydrodynamic force and $\dot{x}(t)$ the velocity in the relevant direction (CF or IL). The hydrodynamic force is found by substracting the inertia force from the total measured force (see Section 5.6.2).

Added mass coefficient

The added mass coefficient is given by:

$$C_{e,IL/CF} = \frac{1}{\frac{\pi D_H^2}{4}\rho L \omega_{osc}^2 x_0} F_{hydro,0,IL/CF} cos(\phi) \tag{5.17}$$

$F_{hydro,0,IL/CF}cos(\phi)$ is estimated using the power transfer method by (Aronsen):

$$F_{hydro,0} cos(\phi) = -\frac{2}{x_0 \omega_{osc}^2} \lim_{T \to \infty} \frac{\int_t^{t+T} F_{hydro}(t) \cdot \ddot{x}(t) dt}{T} \tag{5.18}$$

Where $F_{hydro}(t)$ is the hydrodynamic force and $\ddot{x}$ the acceleration in the relevant direction (CF or IL).

5.6 Data handling

5.6.1 MCL files

The carriage can be set up to run from a pre-made MCL file as opposed to be run manually (NTNU, n.d.). The MCL files each contain a matrix with the displacements/rotations for all the six degrees of freedom the system can handle. This is referred to as the motion matrix. The motion matrix is of dimension $nx6$, where n is the number of displacement/rotation values. Table 5.7 shows the format of the matrix.

Table 5.7: The format of the matrix used in a MCL file

Column number	Content
1	Displacements in x-direction of the main carriage
2	Transverse carriage displacements (n/a)
3	IL displacements
4	Rotations around z-axis (n/a)
5	CF displacements
6	CF displacements

It should be noticed that column 5 and 6 take the same values. In these experiments, only CF/IL motions and carriage displacements were of relevance.

A time step, dT, is also specified in the MCL file. This is used by the carriage system to calculate the velocities. A dT value of 0.02 was used for all the runs.

Script for creating MCL files

A script was made in MATLAB to create the MCL files containing the carriage and CF/IL displacements. The script uses a pre-made function for writing the motion matrix to a .MCL file. The motion matrix is however build from scratch. The MATLAB script is included in Appendix A.

The carriage was programmed to accelerate to a constant speed of $0.2m/s$ for all test runs. A velocity of $0.2m/s$ was used when calculating all the nondimensional frequencies ($\hat{f}$) in the test matrices, using Equation 4.7. An acceleration of $0.1m/s^2$ was used while the maximum acceleration the system can handle is $0.5m/s^2$.

The CF and IL displacements were calculated using Equation 5.11 and 5.12. In addition, a "warm up" period was made based on the equation of an underdamped harmonic motion:

$$z = A \cdot e^{-\gamma t} cos(\omega t) \tag{5.19}$$

Where γ is a damping coefficient. The matrix storing the values from Equation 5.19 was flipped, giving the warm up period as shown in Figure 5.15.

The warm up period was necessary to gradually increase the amplitudes of the oscillations after advice by Torgeir Wahl (Wahl, 2015).

5.6.2 Post processor

A post processor was made prior to the experiments to calculate the hydrodynamic coefficients. The post processor was made in MATLAB and is included in Appendix B. The MATLAB code was based on various MATLAB files provided by PhD Decao Yin. The calculations were based on the equations in Section 5.5. This section will discuss some important methods and concepts used in the calculations.

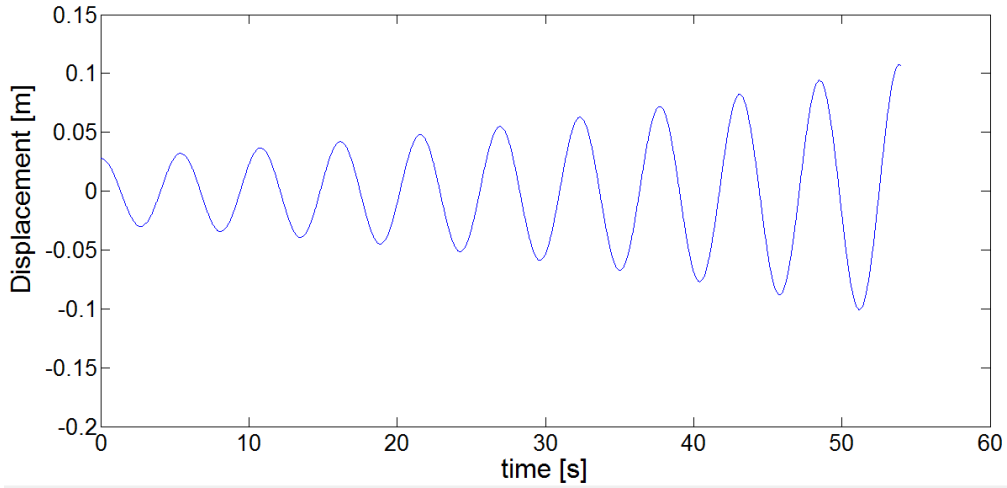

Figure 5.15: Illustration of the warm up period of the test runs.

Selecting the steady state zone

The steady state zones used in the calculations were selected where the motions and forces gave a repetetative pattern. This would obviously always be after the "warm up" period described in Section 5.6.1. The post processor was made always to start and end the steady state zone at a zero upcrossing point as shown in Figure 5.16. This was important to make an integer number of periods.

Calculating the hydrodynamic force

The excitation and added mass coefficients are calculated based on the hydrodynamic force. The hydrodynamic force is found by substracting the inertia force from the measured force:

$$F_{hydro,CF/IL} = F_{measured,CF/IL} - m \cdot a_{CF/IL} \tag{5.20}$$

The acceleration signals are calculated from the CF/IL displacements. The mass is the total mass in the configuration, including the bundle model mass as described in detail in Section 5.7.3.

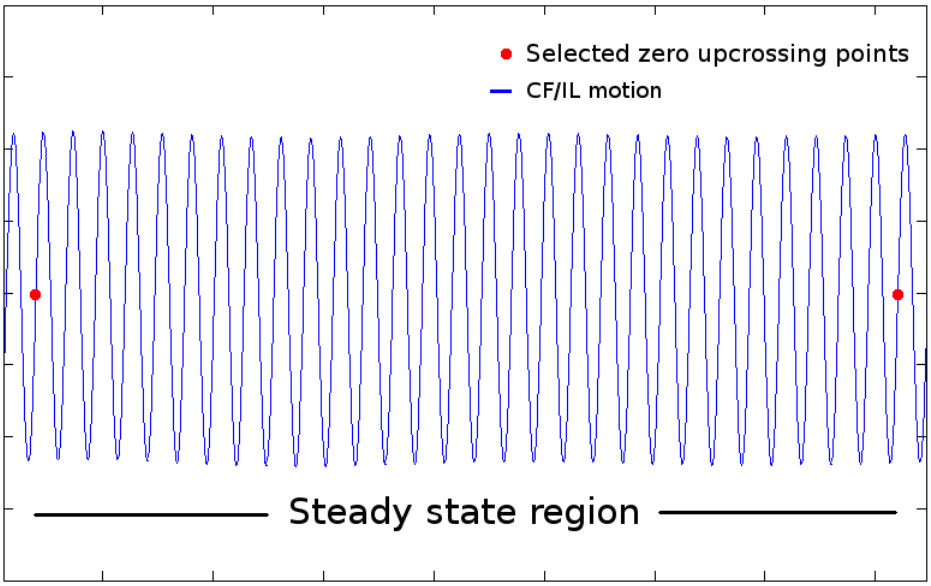

Figure 5.16: Illustration of the selected zero upcrossing points and the steady state zone for a typical run.

Estimating the limit functions

The limit functions in Equation 5.16 and 5.18 are estimated by using an integer number of oscillation periods, as Aronsen did in his experiments (Aronsen, 2007):

$$T = n \cdot T_{osc} \tag{5.21}$$

This estimation was done because $T \to \infty$ is not valid, due to the limited length of the experiments (Aronsen, 2007).

Estimating the integrals with numerical integration

The integrals in Equation 5.16 and 5.18 were estimated using the built-in function trapz() in MATLAB (MathWorks, 2015). This function uses the trapezoidal rule. The grid spacing is here $\Delta t = \frac{1}{100}$ since the sampling frequency is 100Hz as described in Section 5.1.6. For more information of the function it is referred to the MATLAB documentation.

5.7 Uncertainty analysis

This section will address the uncertainties in the experiments. Due to the limited time of the project a full data reduction equation (DRE) analysis was not performed. For DRE equations from similar experiments it is referred to the PhD theses of Aronsen (2007) and Yin (2013).

In general there are two types of errors: bias (systematic) errors and precision (random) errors (Aronsen, 2007). An example of an bias error in these experiments is the error in the CF and IL calibration factor. An example of a precision error is the error in water density due to variation in temperatures (Aronsen, 2007).

5.7.1 Uncertainty in bundle geometry

The outer and inner diameter of one pipe in the bundle was measured at one specific point using a slide caliper. The outer diameter of one pipe was used when calculating the hydrodynamic diameter of the bundle and the area of the empty space between the pipes as described in Section 5.2. It should be noted that the derived formula for the hydrodynamic diameter and the empty space between the pipes is based on an assumption that the pipes are in direct contact with each other, i.e. no space between them. To accomplish this on the fabricated bundle model used in the experiments, the pipes were pressed together and glued. Some deviation from the assumption of full contact between the pipes may however exist. The bias error of the diameter of one pipe is taken from Aronsen to be 2mm (Aronsen, 2007). This is because Aronse used the same measuring device (slide caliper).

The length of the bundle model was measured to be 2.0m using a yard-stick. The uncertainty of this length is estimated to be 5mm, the same as Aronsen used in his experiments (Aronsen, 2007).

The errors in the bundle geometry are considered to be bias errors. The errors are summarized in Table 5.8.

Table 5.8: The error in bundle geometry.

Diameter of one pipe in the bundle	$0.05m$
Error in pipe diameter, B_D	$0.002m$
Length of the bundle	$2.0m$
Error in bundle length, B_L	$0.005m$

5.7.2 Uncertainty in water density

The water temperature was measured multiple times during the experiments. The measured temperatures are shown in Table 5.9.

Table 5.9: Measured temperatures during the experimental period

Temperature	Date (dd.mm.yy)
13.8	31.03.15
13.8	01.04.15
12.8	01.04.15
15.8	07.04.15
14.2	07.04.15
14.6	08.04.15
13.8	08.04.15
14.8	09.04.15
13.6	09.04.15
14.8	10.04.15
14.2	10.04.15
14.8	11.04.15
15.2	12.04.15

The calculated mean temperature is presented in Table 5.10 along with the corresponding mean density and some statistical data.

Table 5.10: Mean temperature, density and statistical values

Mean temperature	STD,temp.	t-value	Mean density	Density error B_ρ
14.3°C	0.773	2.179	$999.2\frac{kg}{m^3}$	0

Since a constant density was used in all the calculations, the density error will be treated as a bias error (Aronsen, 2007). The reason why the error is presented as 0 in Table 5.10 is that the hydrodynamic coefficients were calculated a second time after the experiments using the mean density found from the temperature measurements.

The density in Table 5.10 is found from Table 5.11 provided by Faltinsen (1990). Linear interpolation is used to find the exact value.

When calculating the standard deviation of the temperature the standard deviation formula of a sample has been used (Guttman & Wilks, 1965):

Table 5.11: Density of fresh water as a function of temperature (Faltinsen, 1990).

Temperature [°C]	$\rho_{fw}[kg/m^3]$
0	999.8
5	1000.0
10	999.7
15	999.1
20	998.2

$$s = \sqrt{\frac{1}{n-1}\sum_{j=1}^{n}(x_j - \bar{x})^2} \tag{5.22}$$

where s is the standard deviation of the sample, $\bar{x}$ the sample mean value and x_i each of the values in the sample. n is the sample size.

5.7.3 Uncertainty in mass

As described in Section 5.1.2 the bundle model was connected to a shaft and bearing (including a cylinder). The mass of each of these parts contribute to the total mass used in the hydrodynamic calculations. The mass of each part was measured by an electronic weight and the results are shown in Table 5.12.

Table 5.12: Measured mass of the parts.

Part	Total mass [kg]
Bundle model	4.655
Shaft (2x)	1.450
Shaft housing (2x)	2.580
Cylinder (2x)	1.480

The total mass of all the parts is $10.165kg$. To reduce the buoyancy of the bundle, holes were made close to the end of the pipes to allow them to be filled with water. Because of this, the mass of the water inside the bundle had to be accounted for when calculating the inertia forces. As described in Section 5.6.2 the inertia forces were substracted from the total measured force to get the hydrodynamic force. The hydrodynamic force was used when

calculating the hydrodynamic coefficients as described in Section 5.5. The mass of the water inside the bundle pipes was calculated using the following equation:

$$M_{w,pipes} = 3 \cdot \frac{\pi}{4} D_i^2 L \rho = 3 \cdot \frac{\pi}{4} * (0.047m)^2 * 2m * 999.2kg/m^3 = 10.4kg \quad (5.23)$$

Where D_i is the internal diameter of one pipe, L the length of the bundle model, and ρ the density of the water in the tank. The values are taken from Table 2.1.

Also the water in the space between the pipes in the bundle had to be included in the total mass. The mass of this water is calculated using:

$$M_{w,void} = A_{void} L \rho = 1.0 \cdot 10^{-4} m^2 \cdot 2m \cdot 999.2kg/m^3 = 0.2kg \quad (5.24)$$

Where A_{void} is the area of the space between the pipes in the bundle. The value of A_{void} is taken from Section 5.2. The mass of the water is presentend in Table 5.13.

Table 5.13: Calculated mass of the water.

Section	Calculated mass [kg]
Water inside the three pipes in the bundle	10.4
Water inside the void between the pipes	0.2

The total mass used in the calculation of the inertia forces is then the sum of the total mass of the parts and the total mass of the water:

$$M_{tot} = M_p + M_w = 10.165kg + 10.6kg = 20.765kg \quad (5.25)$$

In the IL direction the mass of the CF force sensors will contribute to the inertia forces in the IL direction. This mass is not included in the calculations of the hydrodynamic coefficients and will hence give a bias error. The mass of the CF force sensors is estimated to be 2x0.12kg.

The uncertainty in the bundle geometry described in Section 5.7.1 and the uncertainty in water density will contribute to the uncertainty of the calculated water mass. These uncertainties are however assumed small and will not be discussed any further.

The uncertainties in mass are summarized in Table 5.14.

Table 5.14: Total mass with calculated errors.

Total mass (CF/IL)	$20.765kg$
Error in mass of the IL calculations (B_M)	0.24kg

5.7.4 Uncertainty due to 3D end effects

Due to the finite length of the bundle 3D effects may give errors to the results (Aronsen, 2007). To reduce the 3D effects one circular plate was mounted at each end. The end plates were the same as Hidetaka Senga used in his experiments are were of diameter 0.23m and thickness 0.005m (Senga & Larsen, 2014).

5.7.5 Uncertainty in the CF/IL motions

The CF and IL motions are measured using potentiometers. These potentiometers are factory calibrated with precision errors that may cause bias errors to the displacements (Yin, 2013). The velocities and accelerations used when calculating the hydrodynamic coefficients are based on the motions from the potentiometers and hence these will also have an bias error.

5.7.6 Uncertainty in towing velocity

The towing carriage position was measured and the average towing velocity was calculated based on these measurements. The flow velocity (U_0) is of the same magnitude as the average carriage velocity, with opposite sign. This is because the flow is going in the opposite direction of the carriage motion. The flow velocity (U_0) is used in the calculation of the hydrodynamic coefficients as described in Section 5.5.

There will be an bias error in the average towing velocity, and hence in the flow velocity (U_0). The bias error origins from an error in the calibration factor in the motion control system of the carriage. This bias error was measured by Aronsen in his experiments to be 1% of the towing velocity (Aronsen, 2007), and hence the flow velocity. The same error will be used here:

Table 5.15: Bias error in the flow velocity.

Flow velocity	Bios error ($\frac{B_{U0}}{U_0}$)
U_0	0.01

5.7.7 Uncertainty in calibration coefficients

When calibrating the CF and IL force signals the calibration factors used in the experiments by Senga and Larsen (2014) was used. The CF and IL force was then tested using a 5kg weight. The results are shown in Table 5.16.

Table 5.16: Calibration errors in force measurements.

Force direction	Applied weight [N]	Measured weight [N]	Error [N]
IL (x)	49.05	48.5	0.55
CF (z)	49.05	49.3	0.25

In the calculations in Table 5.16 the gravity constant used is $9.81\frac{m}{s^2}$. The error is 1.13% in IL direction and 0.51% in CF direction. Both errors represent an bias error. It should however be noted that any bias errors in the applied weight is unknown (the actual weight may not be exactly 5kg). Also, when measuring the force in IL direction a rope and pulley system was used which may give an error due to e.g. friction in the system.

5.7.8 Uncertainty in drag force

The drag force is measured by taking the mean of the IL force in the steady state region. The steady state region is always chosen from one zero upcrossing point to another. This prevents any precision errors due to a random start and end point of the steady state region. The mean drag force is however never completely constant so a precision error will exist depending on what zero upcrossing points are chosen as the start and end of the steady state region. Also a bias error due to the IL calibration error described in Section 5.7.7 is contributing to the total uncertainty of the drag force.

5.7.9 Uncertainty in orientation relative to the fluid flow

Ideally the bundle model should be oriented exactly as in the three configurations described in Section 5.1.7 when running the tests. Obviously there will always exists a deviation from these orientations in the real configuration. To make the configurations as close to the wanted orientations as possible a level of type Hultafors PT25 was used. For Orientation 1 and 2, the level was the only evidence of a good configuration. For Orientation 3, the configuration was also tested by running a few repetition runs in the opposite direction. In Orientation 3 the bundle is symmetric about the z-axis, and hence a run with the same $\hat{f}$ and A/D in each direction should give approximately the same result if the orientation is properly leveled. The results from these runs are shown in Section 5.8.3.

5.7.10 Limited towing tank length

The towing tank is of a limited length. It is important that the steady state of the measured data in the time domain is of a certain length (Aronsen, 2007). This is to get a number of oscillations that will give an acceptable mean value.

5.7.11 Repetition Runs and 95% Confidence Interval

Multiple test runs with the exactly same configuration will give different results. This is due to the precision (random) errors (Aronsen, 2007). To get an estimate of these errors, some tests were run multiple times, as described in Section 5.3.4. These test runs are referred to as the repetition runs. The results from the repetition runs will be used to make a 95% confidence interval of the population mean (μ) for each of the following values:

- Nondimensional amplitude (A/D)
- Excitation coefficient (C_e)
- Added mass coefficient (C_a)
- Drag coefficient (C_D)

In addition the lift coefficient (C_L) will be handled in Orientation 3. The 95% confidence intervals of μ are calculated based on the assumption that the data is normal (Gaussian) distributed, and are calculated using the following equation (Walpole et al., 2007):

$$\mu_{CI95\%} = \bar{x} \pm t_{0.05}\frac{s}{\sqrt{n}} \tag{5.26}$$

Where μ is the population mean, $\bar{x}$ the sample mean, t is the t-value and s is the standard deviation of the sample. The standard deviation of the sample is estimated using Equation 5.22. n is the sample size. The sample size is equal to the number of test runs in each orientation. The reason for using a student t test when calculating the confidence intervals is that the sample size is small (5 or 10 test runs in each orientation).

The calculated 95% confidence intervals from the repetition runs are presented in Section 5.8.

5.8 Results from the experiments

In this section the results from the cross-flow (CF) and combined cross-flow and in-line (IL) experiments are presented. These include the excitation, added mass and drag coefficients for all three orientations. For Orientation 3, the lift coefficients are included. The hydrodynamic coefficients are presented as contour plots made in MATLAB using linear interpolation. The Strouhals number is also calculated for each orientation. The MATLAB code for creating the contour plots are included in Appendix C.

The hydrodynamic coefficients are calculated from the formulas presented in Section 5.5. The coefficients from the repetition runs described in Section 5.3.4 are presented with calculated 95% confidence intervals.

It should be mentioned that for some orientations at specific configurations a few test runs are missing. This can be seen by comparing the test matrices defined in section 5.3 and the contour plots of the results. The test runs are presented in the contour plots to show where the data are interpolated. The missing test runs are due to individual problems with the sensors etc. for the specific runs. The problems were discovered after the experimental period.

5.8.1 Pure CF in Orientation 1

This section presents the CF results of all the runs in Orientation 1. It should be noted that the run with $\hat{f} = 0.325$ and $A/D = 0.4$ was excluded from the results due to some problems with the measured CF force for that specific run. The contour plots shown in the next sections are thus based on one run less than the test matrix described in Section 5.3.2.

St and C_D for the stationary cylinder run

One stationary cylinder run was done in Orientation 1. To find the Strouhals number (St), the power spectra was calculated and plotted as shown in Figure 5.17.

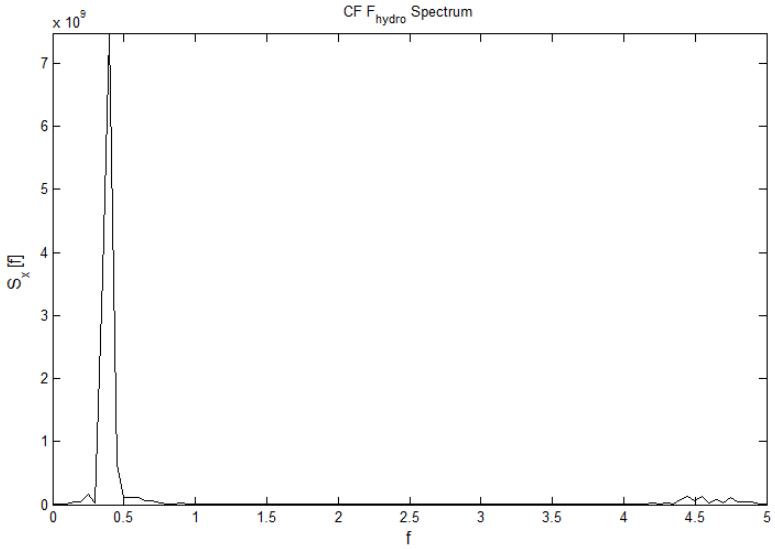

Figure 5.17: Power spectra for the CF hydrodynamic force for Orientation 1.

The vortex shedding frequency is estimated to be the same as the top frequency in the specter. The top frequency was measured to be 0.3998 and the mean velocity 0.2023. The strouhals number was then calculated based on Equation 4.5:

$$St = \frac{f_v \cdot D_h}{U_o} = \frac{0.3998[\frac{1}{s}] \cdot 0.107735[m]}{0.202[\frac{m}{s}]} = 0.213[-] \tag{5.27}$$

The mean drag coefficient, for the stationary cylinder run in Orientation 1, was calculated using Equation 5.13. The mean drag coefficient was found to be 1.1 [-].

The results are summarized in Table 5.17.

Table 5.17: The Strouhals number and drag coefficient found from the stationary cylinder run in Orientation 1.

$St[-]$	$C_D[-]$
0.213	1.1

The repetition runs and 95% confidence cntervals

The repetition runs were used to handle the uncertainty due to the precision errors in each run. The results from the 10 repetition runs done in Orientation 1 are presented in Table 5.18.

Table 5.18: Results for the 10 repetition runs with $\hat{f} = 0.175$ and $A/D = 0.2$.

Run no.	$A/D[-]$	$C_e[-]$	$C_a[-]$	$C_D[-]$
1	0.205	-0.558	-0.971	1.408
2	0.208	-0.538	-0.861	1.347
3	0.206	-0.620	-1.066	1.487
4	0.206	-0.553	-1.108	1.443
5	0.213	-0.519	-0.811	1.276
6	0.209	-0.527	-1.066	1.412
7	0.204	-0.572	-1.104	1.372
8	0.207	-0.578	-1.074	1.413
9	0.203	-0.602	-1.092	1.293
10	0.206	-0.558	-0.995	1.379

The sample mean and standard deviation was calculated for each case in Table 5.18. The 95% margin of error and confidence intervals of the population mean (μ) were then calculated using Equation 5.26. The results are presented in Table 5.19.

In Table 5.19, $\bar{x}$ is the mean value and s the standard deviation. $\mu_{CI95\%}$ is the confidence interval.

Table 5.19: Statistical data for A/D, C_e, C_a and C_D found from the repetition runs in Orientation 1.

	$\bar{x}$	s	t-value	95% margin of error	$\mu_{CI95\%}$
A/D	0.207	0.003	2.262	0.002	0.207 ± 0.002
C_e	-0.563	0.032	2.262	0.023	-0.563 ± 0.023
C_a	-1.015	0.105	2.262	0.075	-1.015 ± 0.075
C_D	1.383	0.065	2.262	0.046	1.383 ± 0.046

It is noticed from Table 5.19 that the added mass coefficient (C_a) has the widest confidence interval. This is because the data found for the added mass coefficient, presented in Table 5.19, is spread the most. The nondimensional amplitude (A/D) has the smallest confidence interval.

The excitation coefficients

Figure 5.18 shows the contour plot of the CF excitation coefficients found in Orientation 1 for the pure CF tests.

The test runs are shown as gray dots in Figure 5.18 with the values of $\hat{f}$ and A/D measured from each run. In general, it was noticed that the measured $\hat{f}$ was slightly lower than the programmed $\hat{f}$. The measured A/D on the other hand was slightly higher than the programmed A/D. These errors are representing bias errors. The excitation coefficients are however calculated using the measured values of $\hat{f}$ and A/D, and the errors will not affect these results.

Figure 5.18 shows that the positive excitation coefficients ranges from values of $\hat{f}$ between approximately 0.15 and 0.45 for low amplitudes. This is referred to as the excitation region (Aronsen, 2007). In comparison, the excitation region for a circular cylinder is between nondimensional frequencies of approximately 0.125 and 0.3 (Passano et al., 2014a). The maximum A/D ratio of the excitation region is approximately 0.8 for both the bundle model and a circular cylinder. The maximum excitation coefficient was found to be 0.715 at a nondimensional frequency and amplitude of 0.2 and 0.4, respectively.

The excitation region is where the excitation coefficients are positive. A positive excitation coefficient means that energy is transfered from the fluid to the bundle, as described in Chapter 4. The area with negative excitation coefficients is where the energy is transferred from the bundle to the fluid.

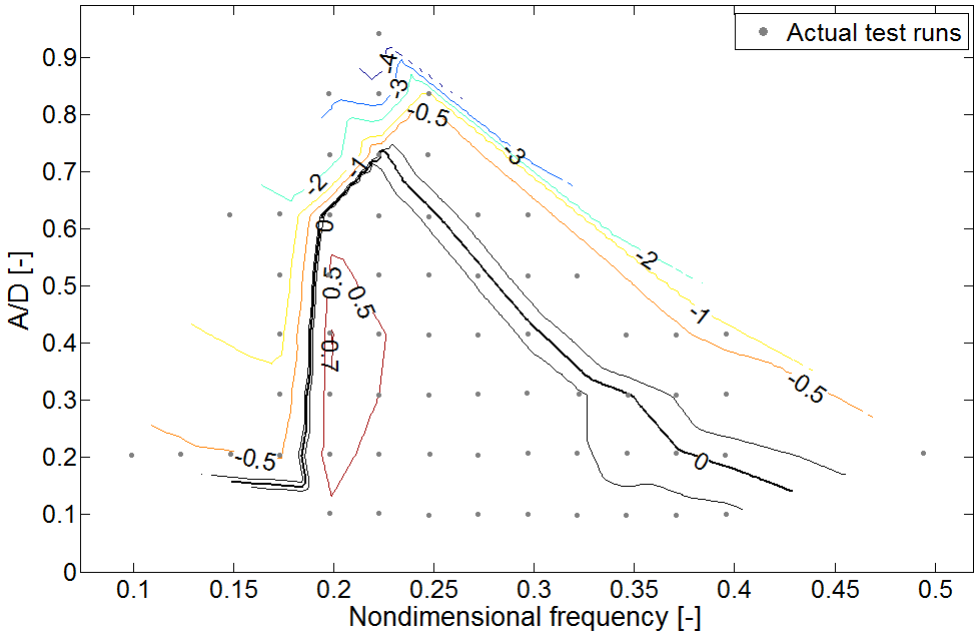

Figure 5.18: Contour plot of the CF excitation coefficients found for Orientation 1 in pure CF. The black lines shows the zero contour line including an error of ± 0.023.

The zero contour line, shown as a bold black line on Figure 5.18, seperates these two regions. The thin black lines show the zero contour with an error of ± 0.023. The lines show that the lower boundary of the excitation region is very little affected by the error. The upper boundary is however more affected by the error due to the low change in C_e values in this region.

The added mass coefficients

The contour plot of the added mass coefficients found for Orientation 1 is shown in Figure 5.19.

The added mass values in Figure 5.19 are close to independent of the A/D ratio for nondimensional frequencies of approximately $0.18 - 0.19$ at A/D ratios below 0.6. This is similar to a circular cylinder except that the vertical added mass lines are found at nondimensional frequencies of $0.16 - 0.17$ (Passano et al., 2014a). For higher frequencies the added mass coefficients are more amplitude dependent. The maximum added mass coefficient found

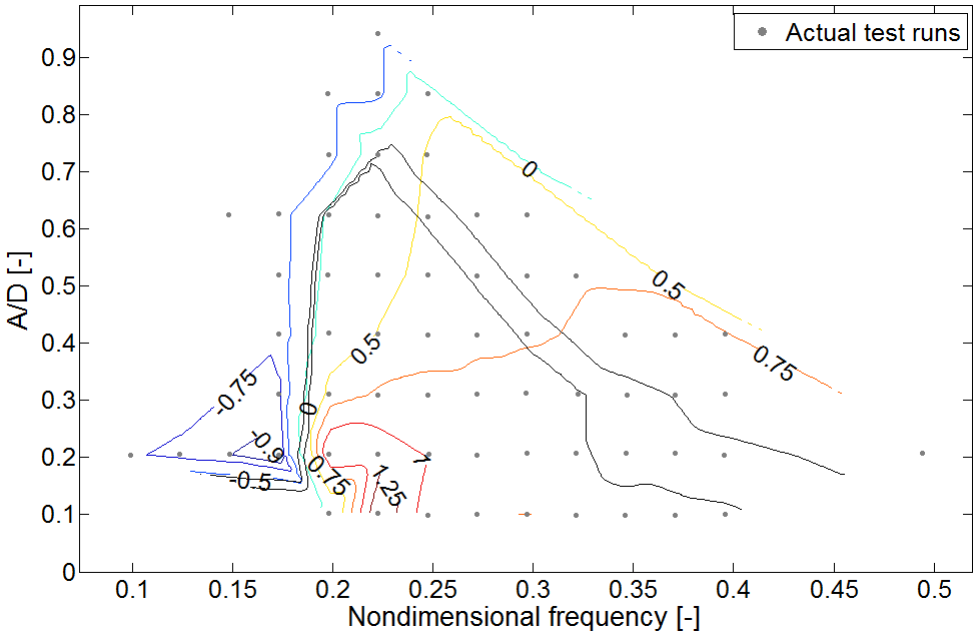

Figure 5.19: Contour plot of the CF added mass coefficients found for Orientation 1. The black lines shows the excitation zero contour line including an error of ± 0.023.

for the bundle in Orientation 1 was approximately 1.25. This is lower than for a circular cylinder which have added mass values of up to approximately 4 (Passano et al., 2014a). A region of negative added mass is also seen on Figure 5.19. This region is however based on only a few runs.

The drag coefficients

The contour plot of the drag coefficients found in Orientation 1 is shown in Figure 5.20. The drag coefficients ranges from 1.2 to 2.9. In comparison the drag coefficient found in the stationary cylinder run was 1.1 in Orientation 1. It can be seen from the contour plot that the drag coefficients are strongly dependent of the amplitude for higher nondimensional frequencies (close to horizontal lines). For lower nondimensional frequencies the drag coefficients are very dependent on the frequency (almost vertical lines).

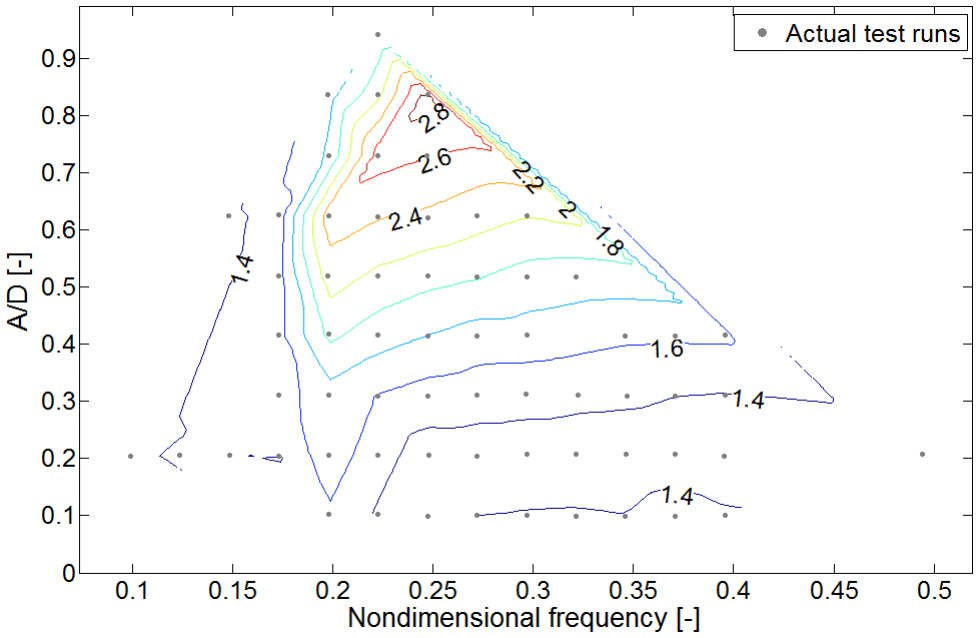

Figure 5.20: Contour plot of the drag coefficients found for Orientation 1.

5.8.2 Pure CF in Orientation 2

The results for all the pure CF runs in Orientation 2 are presented in the following sections. The run with $\hat{f} = 0.125$ and $A/D = 0.2$ was removed due to problems with the force sensor for that specific run. The run with $\hat{f} = 0.1$ and $A/D = 0.1$ was removed for the same reason.

St and C_D for the stationary cylinder run

One stationary cylinder run was done in Orientation 2. The Strouhals number (St) and drag coefficient (C_D) for this run was calculated with the same methods as for Orientation 1 (see Section 5.8.1). The results are shown in Table 5.20.

Table 5.20: Strouhals number and drag coefficient for the stationary cylinder run, Orientation 2.

$St[-]$	$C_D[-]$
0.178	1.5

Table 5.20 shows the drag coeffient in Orientation 2 was found to be 1.5. In comparison the drag coefficient found in orientat 1 was 1.1. The Strouhals number is 0.178 in Orientation 2, which is lower than for Orientation 1. In orientation the Strouhals number was found to be 0.213.

The repetition runs and 95% confidence intervals

The results for the five repetition runs done in Orientation 2 are presented in Table 5.21.

Table 5.21: Results for the 5 repetition runs with $\hat{f} = 0.175$ and $A/D = 0.2$ in Orientation 2.

Run no.	A/D	C_e	C_a	C_D
1	0.216	-0.624	3.538	1.622
2	0.209	-0.699	3.690	1.626
3	0.221	-0.656	3.211	1.633
4	0.207	-0.742	3.648	1.613
5	0.205	-0.728	3.818	1.621

The mean ($\bar{x}$), standard deviation (s), and 95% confidence interval of the population mean $\mu_{CI95\%}$ was calculated from the data in Table 5.21 using the same method as in Orientation 1. The results are shown in Table 5.22.

Table 5.22: Statistical data for A/D, C_e, C_a and C_D found from the repetition runs in Orientation 1.

	$\bar{x}$	s	t-value	95% margin of error	$\mu_{CI95\%}$
A/D	0.212	0.007	2.776	0.010	0.212 $\pm$ 0.010
C_e	-0.690	0.049	2.776	0.061	-0.690 $\pm$ 0.061
C_a	3.581	0.230	2.776	0.286	3.581 $\pm$ 0.286
C_D	1.623	0.007	2.776	0.010	1.623 $\pm$ 0.010

The margin of error of the excitation coefficient was 0.061 in Orientation 2, compared to 0.023 in Orientation 1. Thus the 95% confidence interval is wider in Orientation 2 than in Orientation 1. The added mass confidence interval is also wider in Orientation 2 than in Orientation 1. The drag coefficient margin of error is however found to be smaller in Orientation 2. It should be noticed that the confidence interval for C_a is much wider than for the other coefficients.

The excitation coefficients

The contour plot of the CF excitation coefficients found for Orientation 2 in pure CF is shown in Figure 5.21.

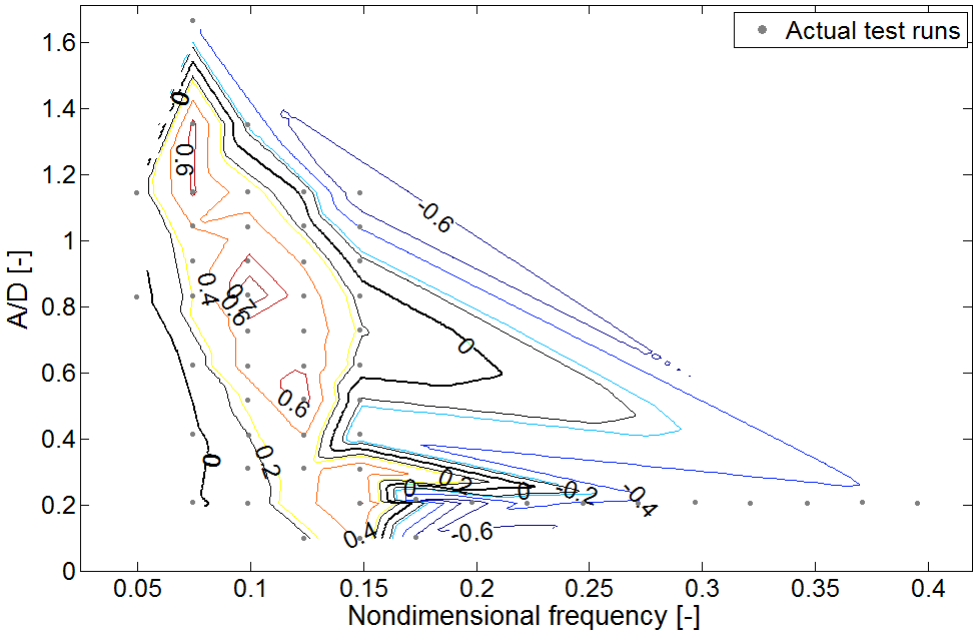

Figure 5.21: Contour plot of the CF excitation coefficients found from the pure CF tests in Orientation 2. The black lines show the zero contour line including an error of ± 0.061.

The zero line ranges from nondimensional frequency values between approximately 0.075 and 0.2 for low amplitudes. Hence the excitation region is shifted to the left compared to the excitation region found in Orientation 1 (pure CF). The excitation region is ranging vertically to nondimensional amplitudes of approximately 1.55 at the most. In comparison the excitation region found for the pure CF tests in Orientation 1 had a maximum A/D ratio of 0.8.

The maximum excitation coefficient is found to be 0.796 for Orientation 2, compared to 0.715 in Orientation 1. The maximum is found where $\hat{f} = 0.1$ and $A/D = 0.8$.

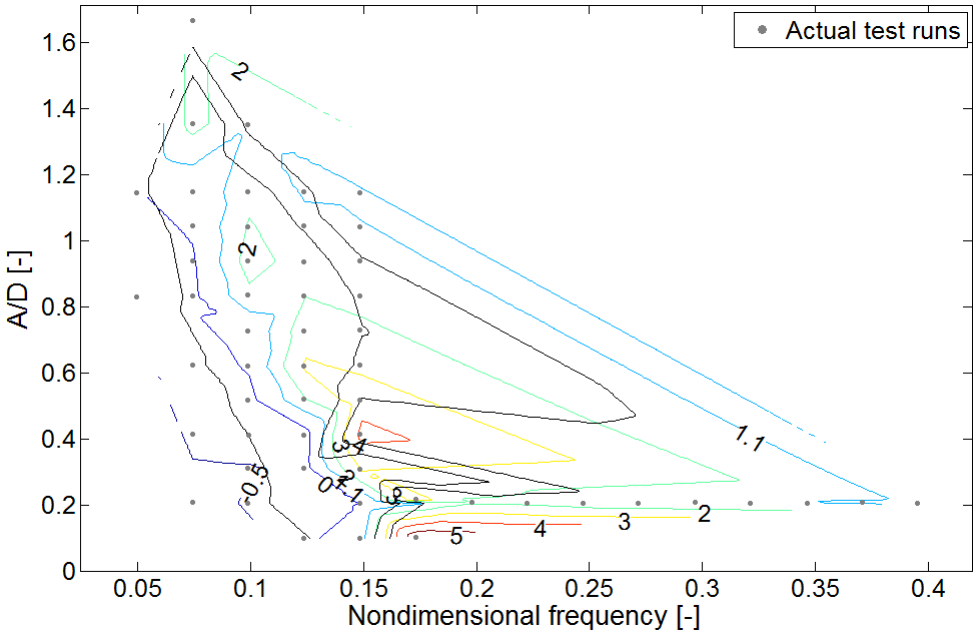

Figure 5.22: Contour plot of the added mass coefficients found for Orientation 2. The black lines shows the excitation zero contour line including an error of ± 0.061.

The added mass coefficients

Figure 5.22 shows the contour plot of the added mass coefficients found in Orientation 2. The plot shows a more frequency dependent added mass compared to Orientation 1. The maximum added mass is approximately 5 in Orientation 2, compared to approximately 1.25 in Orientation 1. For the higher nondimensional frequencies, the contour plot shows a very strong amplitude dependency. The number of test runs (data points) in this region is however very limited, and hence this should be taken into consideration when interpreting the results.

The drag coefficients

The contour plot of the drag coefficients found for Orientation 2 is shown in Figure 5.23. The values ranges from 1.4 to 2.5. In comparisson the drag coefficient for the stationary cylinder run was 1.5. It should also be noted that the drag coefficients for Orientation 1 ranged from 1.2 to 2.9. The

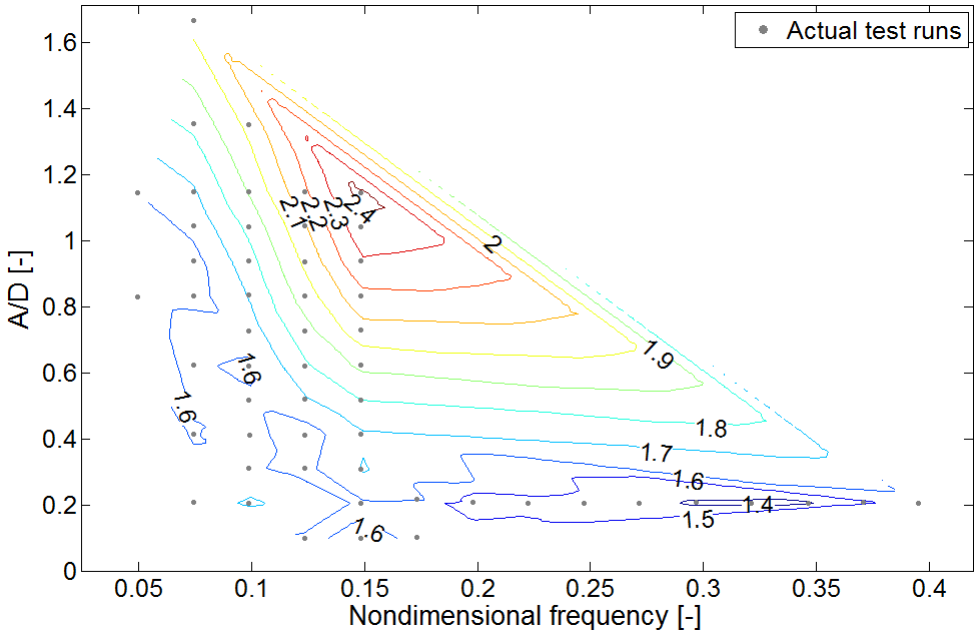

Figure 5.23: Contour plot of the drag coefficients found for Orientation 2.

figure shows an amplitude and frequency dependence of the drag coefficients for the areas with the most test runs. This is different from Orientation 1 which typically had regions of either frequency or amplitude dependent drag coefficients.

5.8.3 Pure CF in Orientation 3

The results from the pure CF experiments in Orientation 3 are presented in the following sections.

St and C_D for the stationary cylinder Run

One stationary cylinder run was done in Orientation 3. The drag coefficient and Strouhals number was calculated using the same method as for the similar test in Orientation 1. The results are shown in Table 5.23.

The results in Table 5.23 show that the drag coefficient for the stationary cylinder run in Orientation 3 is significantly lower than for the two other orientations. The drag coefficient in Orientation 1 and 2 was 1.1 and 1.5,

Table 5.23: The Strouhals number and drag coefficient calculated from the stationary cylinder run in Orientation 3.

$St[-]$	$C_D[-]$
0.248	0.5

respectively. The Strouhals number for Orientation 3 is 0.248 which is the largest of the three orientations.

The repetition runs and 95% confidence intervals

The results from the five repetition runs done in Orientation 3 are presented in Table 5.24. It should be noticed that the lift coefficient C_L is included since a net lift force was found in Orientation 3.

Table 5.24: Results for the five repetition runs with $\hat{f} = 0.175$ and $A/D = 0.2$ in Orientation 3.

Run no.	A/D	C_e	C_a	C_D	C_L
1	0.208	-0.532	-0.227	0.581	1.089
2	0.207	-0.522	-0.138	0.660	1.093
3	0.208	-0.510	-0.207	0.702	1.117
4	0.207	-0.484	-0.250	0.687	1.060
5	0.206	-0.502	-0.306	0.623	1.063

As in Orientation 1 and 2 a 95% confidence interval was calculated for the coefficients presented in Table 5.24. The lift coefficient is however unique for the CF results in Orientation 3. The confidence intervals ($CI_{95\%}$) are presented in Table 5.25 with the other statistical data calculated.

Table 5.25 shows that the 95% margin of error for the excitation coefficient (C_e) in Orientation 3 was 0.024. In comparison, the margin of error of the excitation coefficient was found to be 0.023 and 0.061 in Orientation 1 and 2 respectively.

As described in Section 5.7.9 one of the uncertainties in the experiments is the configuration of the three orientations. To check how good the configuration was in Orientation 3, two runs were done in the opposite x-direction. The test runs used the same configuration ($\hat{f}$ and A/D) as the repetition runs. The results of the two runs are presented in Table 5.26.

Table 5.25: The 95% confidence intervals and statistical data for the five coefficients A/D, C_e, C_a, C_D and C_L found from the repetition runs in Orientation 3.

	$\bar{x}$	s	t-value	95% margin of error	$\mu_{CI95\%}$
A/D	0.207	0.001	2.776	0.001	0.207 ± 0.001
C_e	-0.510	0.019	2.776	0.024	-0.510 ± 0.024
C_a	-0.226	0.061	2.776	0.076	-0.226 ± 0.076
C_D	0.651	0.049	2.776	0.061	0.651 ± 0.061
C_L	1.084	0.024	2.776	0.030	1.084 ± 0.030

Table 5.26: Results for the two runs in the opposite x-direction.

Run no.	A/D	C_e	C_a	C_D	C_L
1	0.208	-0.533	-0.200	0.903	1.160
2	0.205	-0.530	-0.356	0.862	1.132

The mean of the drag coefficients presented in Table 5.26 is 0.883. That is 35.6% higher than the mean of the drag coefficients from the repetition runs which is 0.651. The mean of the lift coefficients of the same two runs is 14.4% higher than the mean of the lift coefficient in Table 5.25. So this is a relatively smaller difference. The mean of the excitation coefficients of the two runs in Table 5.26 is -0.532. That is only 4.3% lower than the sample mean of the excitation coefficients from the repetition runs in Table 5.25. The mean of the added mass coefficients for the two runs is -0.278 which is 23.0% lower than the mean found from the five runs in the other direction. Obviously, two runs is very little data, but the results give an idea of the differences of the coefficients. The difference is probably partly due to the error in configuration of Orientation 3, but may also be due to minor differences from the fabrication of the bundle model. Other reasons may also exist, but will not be further discussed here.

Excitation coefficients

Figure 5.24 shows the contour plot of the excitation coefficients found in Orientation 3. The excitation region ranges from approximately 0.25 to 0.3 and is hence relatively small compared to Orientation 1 and 2. It is also ranging to a maximum A/D ratio of approximately 0.25. That means most combinations of A/D and $\hat{f}$ will lead to damping.

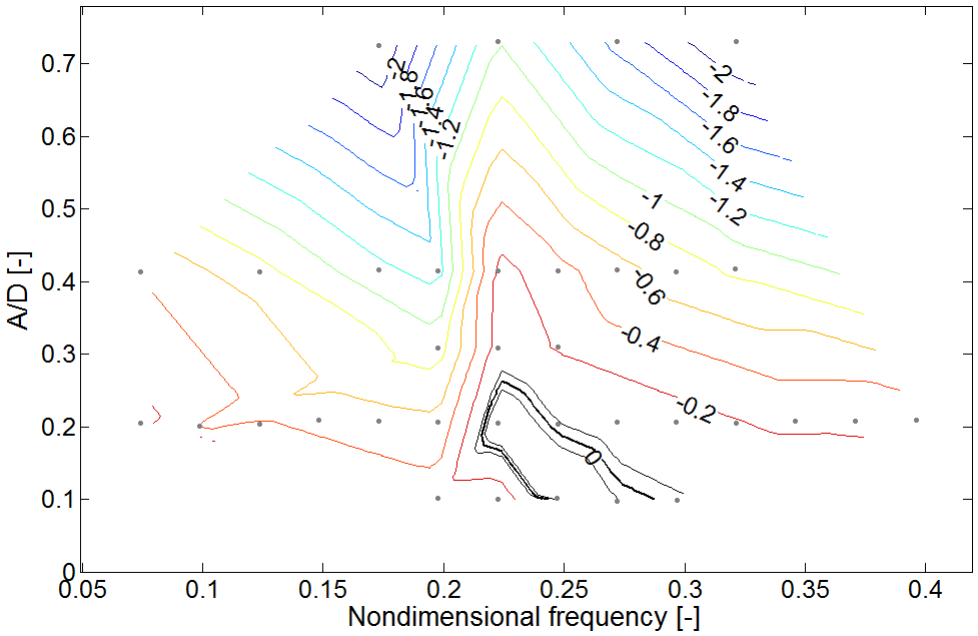

Figure 5.24: Contour plot of the excitation coefficients found for Orientation 3. The black lines shows the zero contour line including an error of ±0.026.

Added mass coefficients

The contour plot of the added mass coefficients found for Orientation 3 is shown in Figure 5.25. As in Orientation 1 the plot has a region where the added mass is very frequency dependent, and not so dependent on the amplitude. This area is seen at $\hat{f}$ of approximately 0.2 which is similar to Orientation 1. Away from this area the added mass is more amplitude dependent. The maximum value of the added mass is found to be approximately 3 which is higher than Orientation 1 but lower than Orientation 2. The minimum value of the added mass is approximately -1 for Orientation 3, which is close the minimum value of Orientation 1 and 2.

Drag coefficients

The drag coefficients are shown in Figure 5.26. In comparrison the drag coefficient of the stationary cylinder run was 0.5. The drag coefficients for Orientation 3 are very amplitude dependent. The absolute values of the drag coefficients are found to range from 0.6 to 1.8. This is significantly lower than

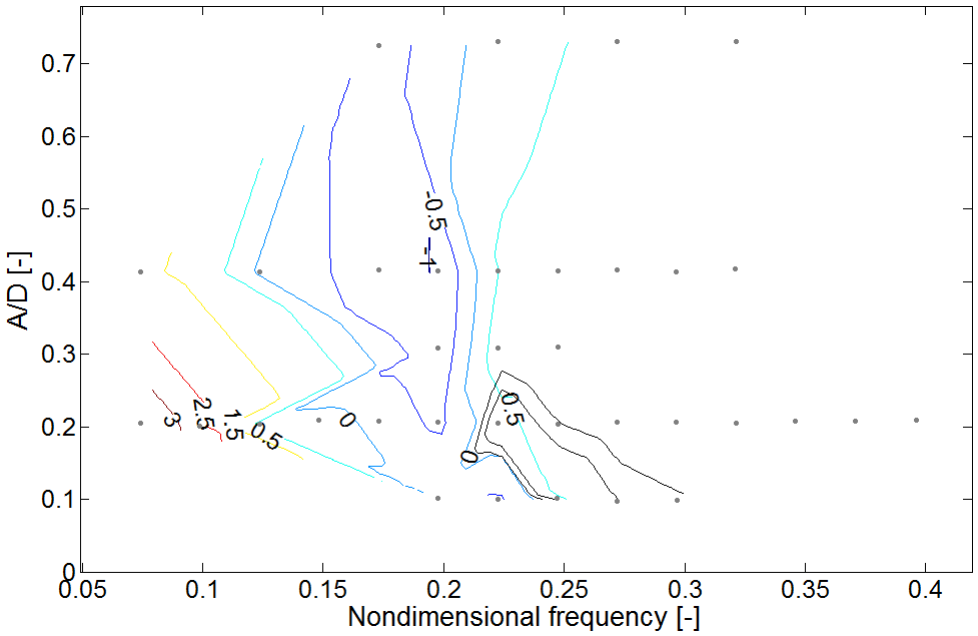

Figure 5.25: Contour plot of the added mass coefficients found for Orientation 3. The black lines shows the zero contour line including an error of ±0.026.

the drag coefficients found for Orientation 1 and 2.

Lift coefficients

The bundle is unsymmetric about the x-axis in Orientation 3 and hence it will be a net lift force. The lift coefficients found in Orientation 3 are shown in Figure 5.27. The lift force ranges from 0.6 to 2.0. The positive value of the lift coefficients indicate that the lift force works in the positive z-direction using the coordinate system in Figure 5.14.

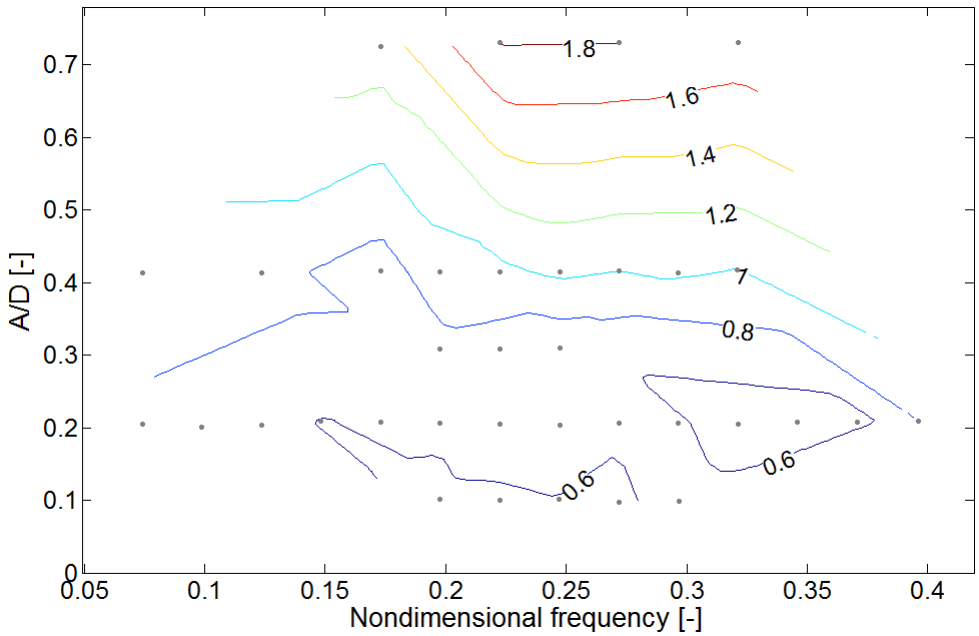

Figure 5.26: Contour plot of the drag coefficients found in Orientation 3.

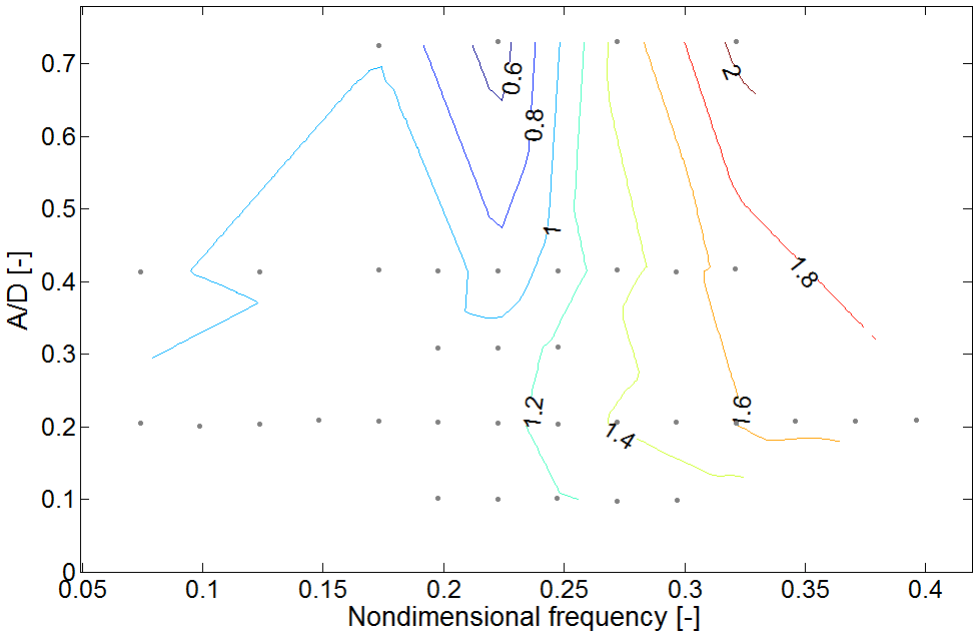

Figure 5.27: Contour plot of the lift coefficients found for Orientation 3.

5.8.4 Combined CF/IL tests in Orientation 1

In the following sections, the results from the combined CF/IL experiments in Orientation 1 are presented. All the combined CF/IL tests done were based on the zero contour line found from the similar tests in pure CF. The results showed that, for the given phase angles (α) and amplitude ratios (A/D), no VIV will occur. This is because no positive IL excitation coefficients were found. In general, the contour plots presented in this section are based on significantly less data than for the pure CF experiments. This should be taken into consideration when interpreting the results. It should be noted that when CF coefficients are presented, the axes of the contour plots represent the CF A/D and nondimensional frequency. When IL coefficients are presented, the axes of the contour plots represent the IL A/D and nondimensional frequency. The IL frequency is twice the CF frequency and the IL amplitude is half the CF amplitude in all test runs, as described in Section 5.3.

Excitation coefficients, $\alpha = \pi$

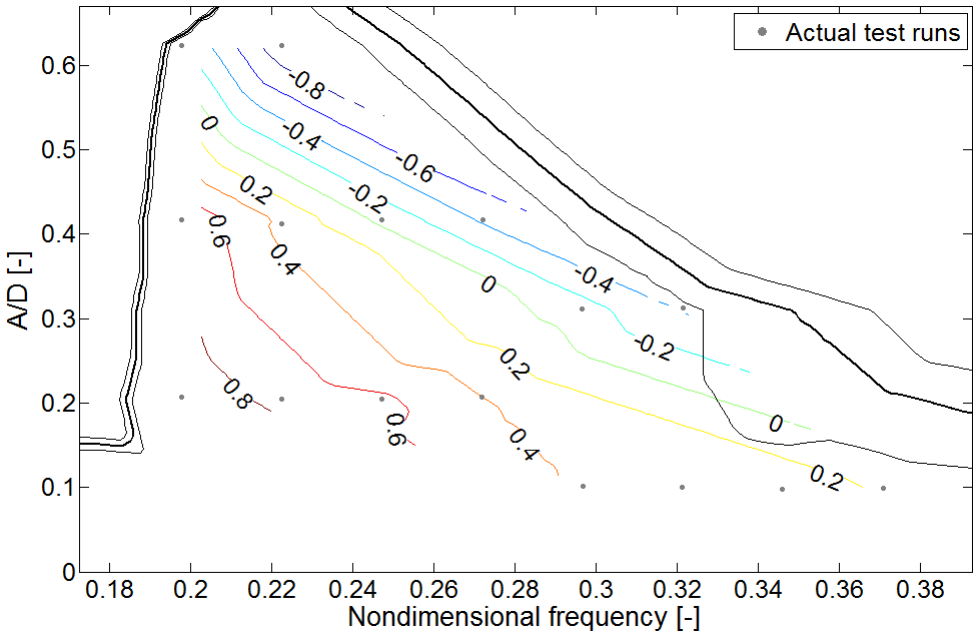

Figure 5.28: Contour plot of the CF excitation coefficients found for combined CF/IL motions ($\alpha = \pi$) in Orientation 1.

Figure 5.28 shows the CF excitation coefficients found from combined CF/IL motions in Orientation 1 ($\alpha = \pi$). The equivalent zero line in pure CF is shown as a black bold line. It should be noticed that the zero line from the combined CF/IL tests is not complete due to the limited number of test runs. The results does however indicate a shift to the left of the combined zero line compared to the pure CF zero line. The values of the excitation coefficients are increasing for decreasing nondimensional frequencies at a fixed A/D ratio. The maximum C_e value is found where $\hat{f} = 0.2$ and $A/D = 0.2$ to be 0.956.

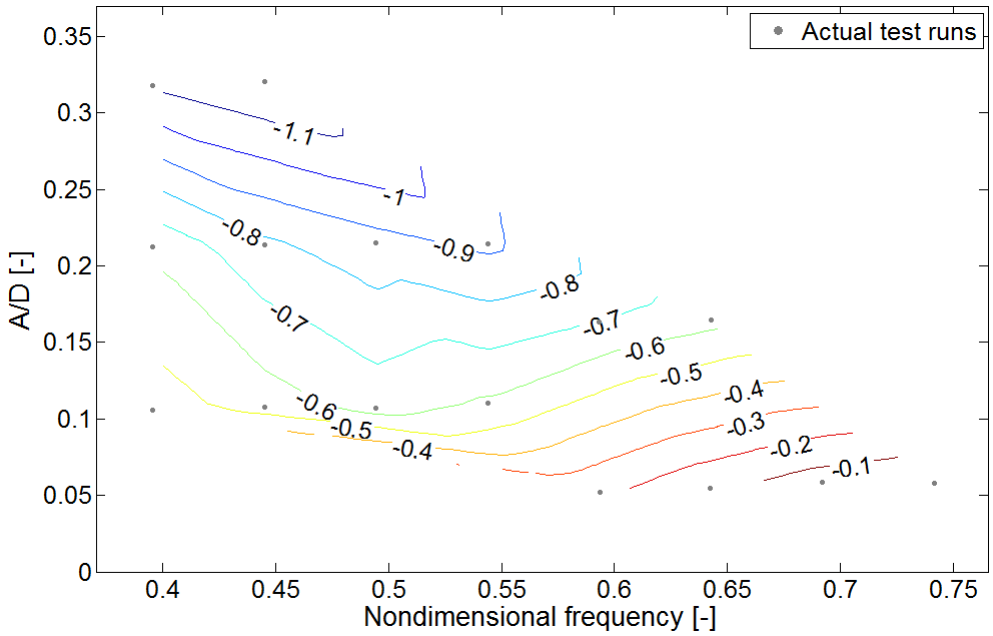

Figure 5.29: Contour plot of the IL excitation coefficients found for combined CF/IL motions ($\alpha = \pi$) in Orientation 1.

Figure 5.29 shows the IL excitation coefficients found from combined CF/IL motions in Orientation 1 ($\alpha = \pi$). The IL frequencies were programmed to be twice the value of the CF frequencies, as described in Section 5.3.3. The IL amplitudes were half of the CF amplitudes. The figure shows no excitation region for the IL excitation coefficients. This indicates that no excitation will occur for the given configuration.

Excitation coefficients, $\alpha = 0$

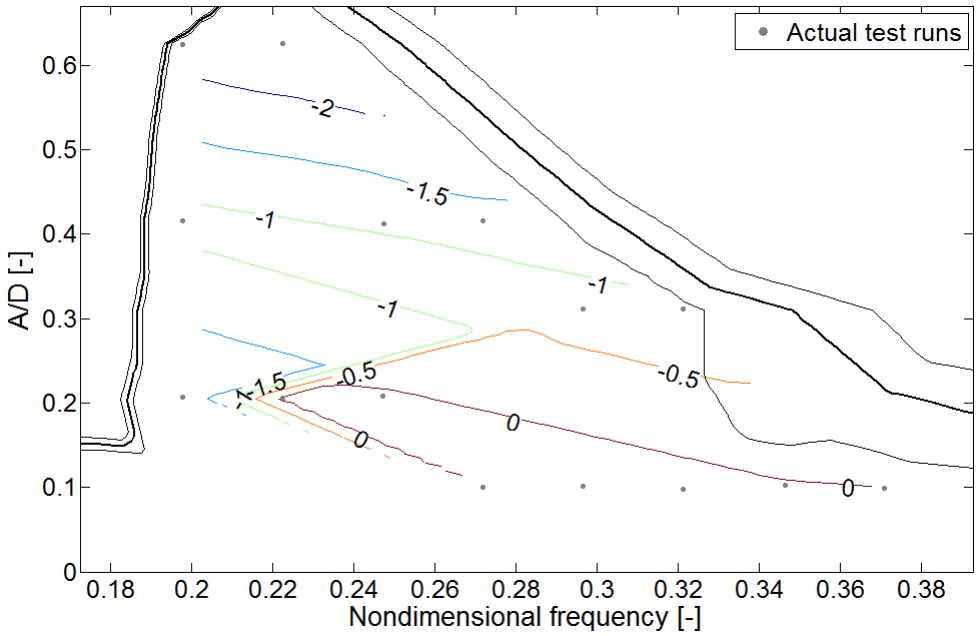

Figure 5.30: Contour plot of the CF excitation coefficients found for combined CF/IL motions ($\alpha = 0$) in Orientation 1.

Figure 5.28 shows the CF excitation coefficients found from combined CF/IL motions in Orientation 1 ($\alpha = 0$). The figure shows that the excitation region is significantly smaller than for the combined CF/IL case with $\alpha = \pi$. The combined CF/IL tests done by Aronsen (2007) with a circular cylinder, also shows that the direction of the periodic motion is of significant importance.

Figure 5.29 shows the IL excitation coefficients found from combined CF/IL motions in Orientation 1 ($\alpha = 0$). As with the similar $\alpha = 0$ tests, no excitation region is found. Hence no VIV will occur with the given combination of α, A/D and $\hat{f}$.

Added mass coefficients, $\alpha = \pi$

Figure 5.32 shows the CF added mass coefficients found from combined CF/IL motions in Orientation 1 ($\alpha = \pi$). The zero contour lines from the

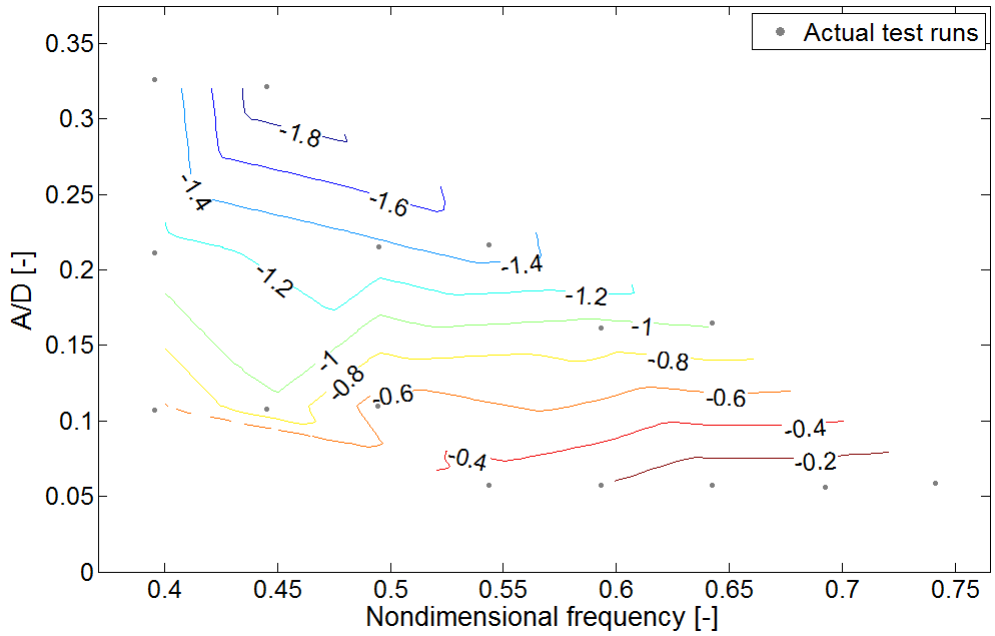

Figure 5.31: Contour plot of the IL excitation coefficients found for combined CF/IL motions ($\alpha = 0$) in Orientation 1.

pure CF experiments in Orientation 1 are included to put the data in context. The added mass coefficients ranges from values between approximately -0.2 and 1. The contour plot shows that the added mass coefficients are both amplitude and frequency dependent. It should be noted that the plot is based on little data, however.

Figure 5.33 shows the IL added mass coefficients found from combined CF/IL motions in Orientation 1 ($\alpha = \pi$). The values have a relatively short range going from approximately 0.6 to 0.7. The added mass coefficients shows both an amplitude and frequency dependence.

Added mass coefficients, $\alpha = 0$

Figure 5.34 shows the CF added mass coefficients found from combined CF/IL motions in Orientation 1 ($\alpha = 0$). The values ranges from approximately -2 to 1. The negative added mass of -2 may be a little suspicious. Aronsen (2007) did however also find regions of relatively large negative added mass coefficients, in his experiments using a circular cylinder. The

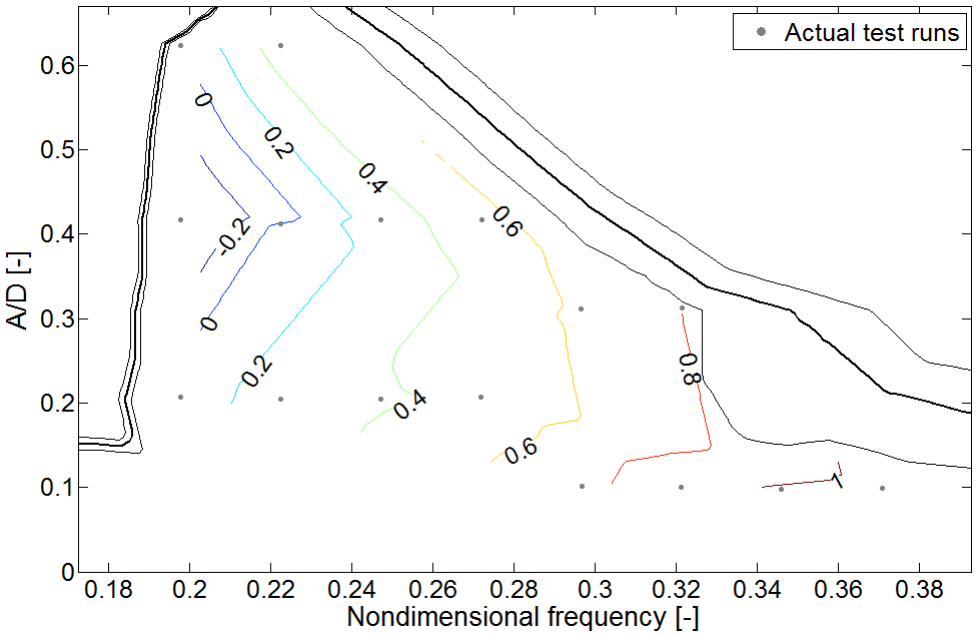

Figure 5.32: Contour plot of the CF added mass coefficients found for combined CF/IL motions ($\alpha = \pi$) in Orientation 1.

contour plot shows that the added mass coefficients are both dependent on the nondimensional amplitude and frequency. The contour plot is however based on little data compared to the pure CF experiments.

The IL added mass coefficients shown in Figure 5.35 are found from combined CF/IL experiments with $\alpha = 0$. The values are higher and the range in values wider than for the similiar experiments with $\alpha = \pi$. For A/D values below 0.2 the added mass coefficients are often more amplitude dependent than frequency dependent. Above $A/D = 0.2$ the added mass coefficients are very frequency dependent only. This area is based on very few data points however.

Drag coefficients, $\alpha = \pi$

Figure 5.36 shows the drag coefficients found from combined CF/IL motions in Orientation 1 ($\alpha = \pi$). The maximum drag coefficient is approximately 3, located . In comparrison the maximum drag coefficient in pure CF for Orientation 1 was 2.8. The lowest drag coefficient is 1.2 compared to 1.4 for

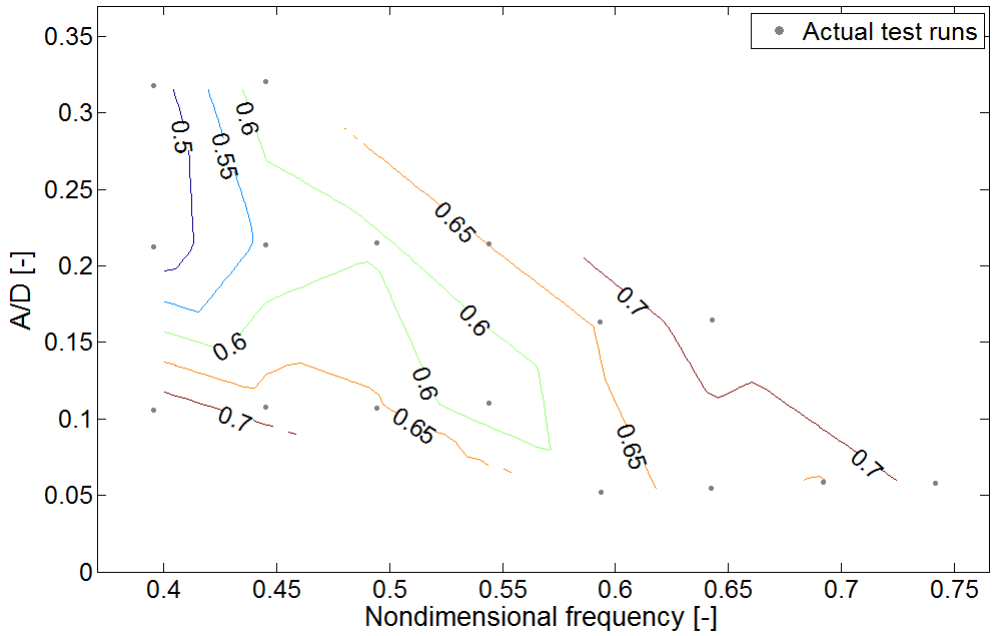

Figure 5.33: Contour plot of the IL added mass coefficients found for combined CF/IL motions ($\alpha = \pi$) in Orientation 1.

the pure CF experiments in Orientation 1.

Drag coefficients, $\alpha = 0$

Figure 5.37 shows the drag coefficients found from combined CF/IL motions in Orientation 1 ($\alpha = 0$). These values are significantly lower than for the same case with $\alpha = \pi$ and also the pure CF drag coefficients in Orientation 1.

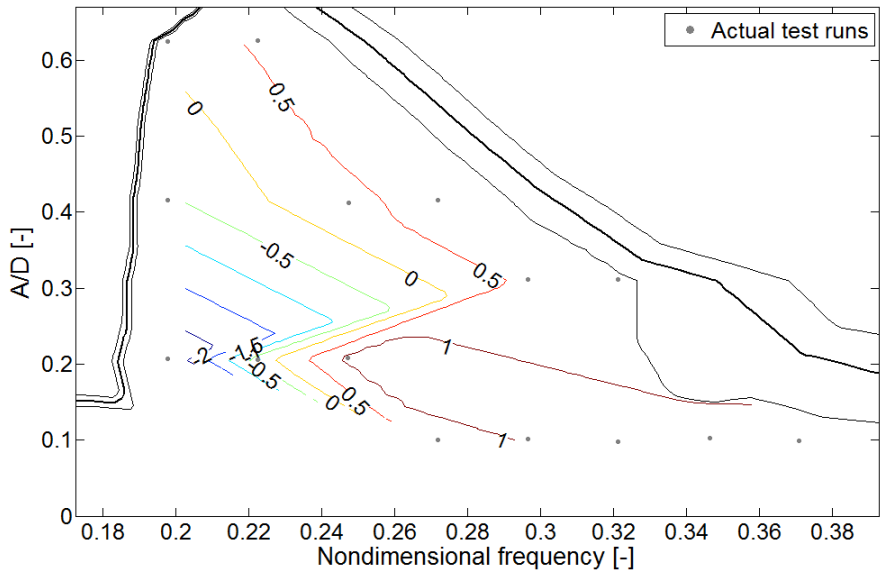

Figure 5.34: Contour plot of the CF added mass coefficients found for combined CF/IL motions ($\alpha = 0$) in Orientation 1.

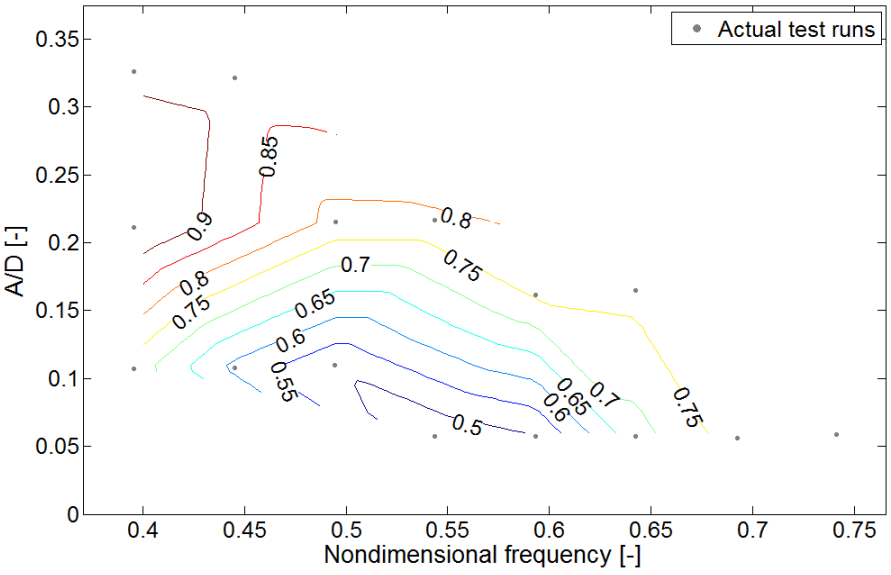

Figure 5.35: Contour plot of the IL added mass coefficients found for combined CF/IL motions ($\alpha = 0$) in Orientation 1.

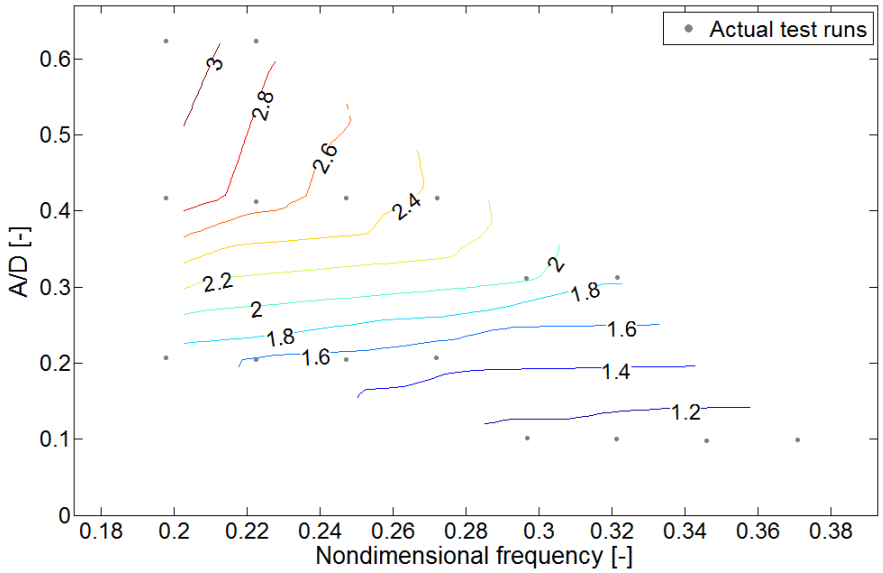

Figure 5.36: Contour plot of the drag coefficients found for combined CF/IL motions ($\alpha = \pi$) in Orientation 1.

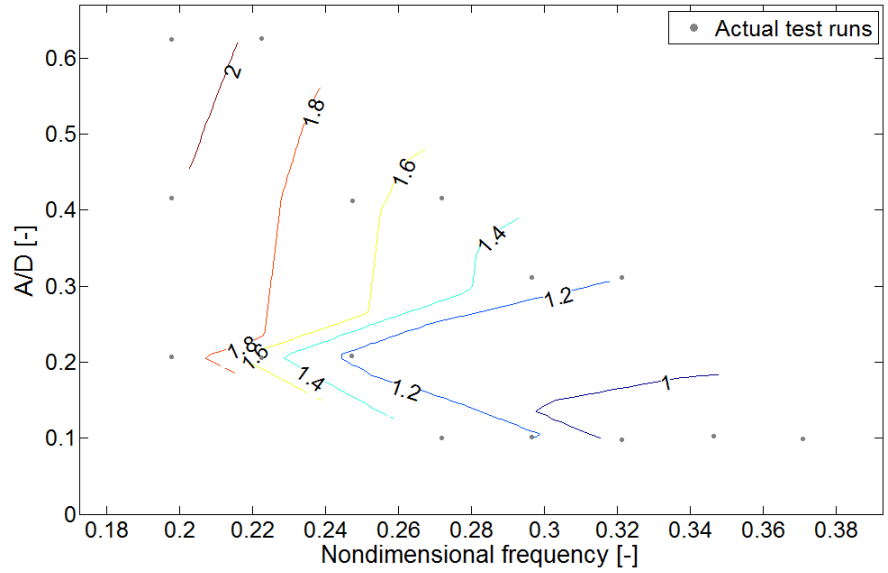

Figure 5.37: Contour plot of the drag coefficients found for combined CF/IL motions ($\alpha = 0$) in Orientation 1. The axes represent CF A/D and nondimensional frequencies.

5.8.5 Combined CF/IL tests in Orientation 2

Excitation coefficients, $\alpha = \pi$

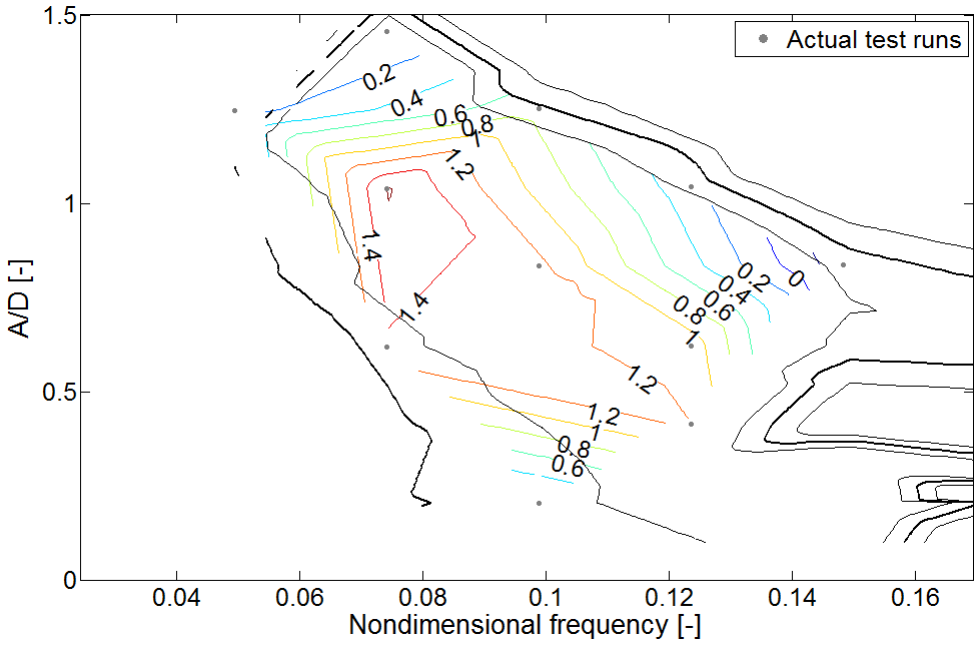

Figure 5.38: Contour plot of the CF excitation coefficients found for combined CF/IL motions ($\alpha = \pi$) in Orientation 2. The axes represent CF A/D and nondimensional frequencies.

Figure 5.38 shows the CF excitation coefficients found from combined CF/IL motions in Orientation 2 ($\alpha = \pi$). The values inside the excitation region are significantly higher than for the pure CF experiments in Orientation 2. The maximum value is approximately 1.4 compared to approximately 0.7 in the pure CF experiments in Orientation 2.

Figure 5.39 shows the IL excitation coefficients found from combined CF/IL motions in Orientation 2 ($\alpha = \pi$). As with the combined CF/IL experiments in Orientation 1, no excitation region is found in the IL direction. This implies that the prescribed combined CF/IL motions for this case are not realistic. The IL excitation coefficients will only lead to damping.

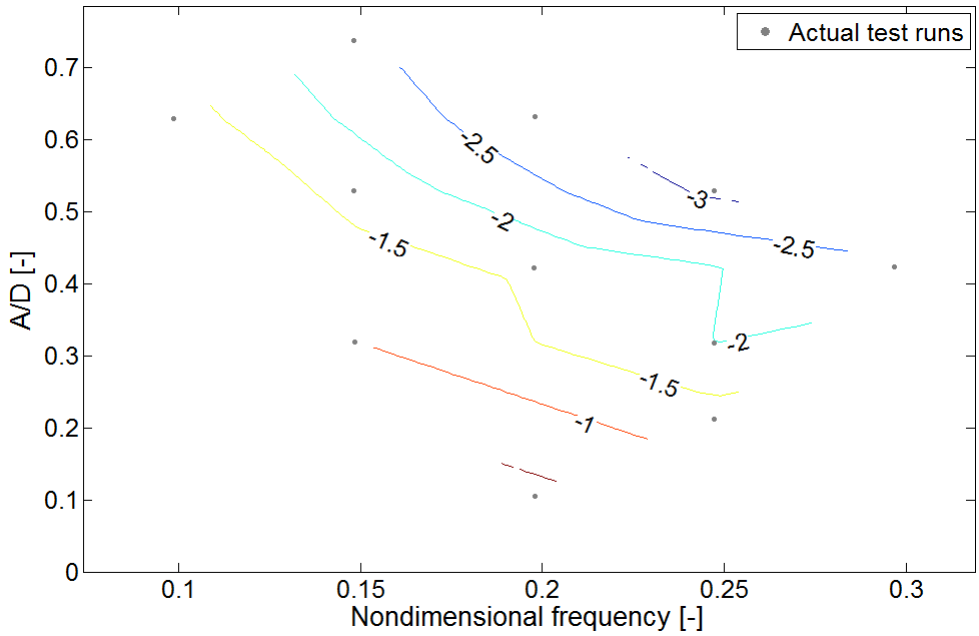

Figure 5.39: Contour plot of the IL excitation coefficients found for combined CF/IL motions ($\alpha = \pi$) in Orientation 2.

Excitation coefficients, $\alpha = 0$

Figure 5.40 shows the CF excitation coefficients found for combined CF/IL motions in Orientation 2 ($\alpha = 0$). Even though the excitation region is not completed due to few data points, the trend shows a left shift compared to the pure CF excitation region. The exictation region is also smaller and with lower excitation coefficient values than in pure CF and the similar tests with $\alpha = \pi$.

Figure 5.40 shows the IL excitation coefficients found for combined CF/IL motions in orientation 0 ($\alpha = 0$). All the excitation coefficients are negative, thus no excitation region. This shows that these combined CF/IL motions will give no VIV. There may however be excitation in both CF and IL direction for other values of α and A/D ratios.

Added mass coefficients, $\alpha = \pi$

Figure 5.42 shows the CF added mass coefficients found from combined CF/IL motions in Orientation 2 ($\alpha = \pi$). The added mass coefficients ranges

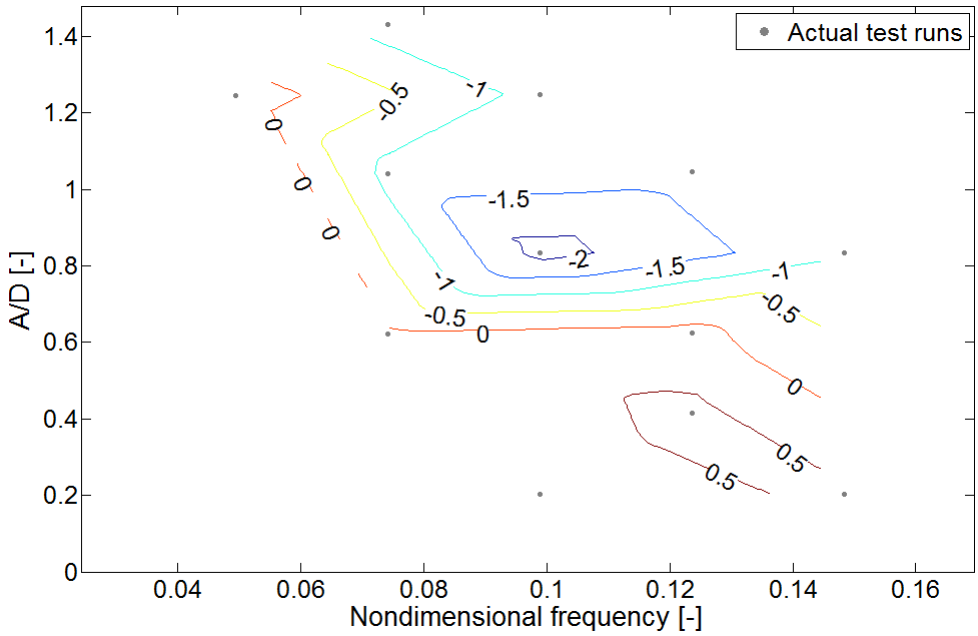

Figure 5.40: Contour plot of the CF excitation coefficients found for combined CF/IL motions ($\alpha = 0$) in Orientation 2.

from values between approximately -1.0 to 6. In comparison the added mass coefficients inside the excitation region in pure CF were in the range -0.5 to 4 approximately. The plot also shows that there are some regions were the added mass coefficients are very frequency dependent as well as regions were they are more amplitude dependent.

Figure 5.43 shows the IL added mass coefficients found from combined CF/IL motions in Orientation 2 ($\alpha = \pi$). The trend is increasing C_a values for increasing frequencies up to approximately $\hat{f} = 0.225$. After that the C_a values decreases for A/D values above 0.35 approximately.

Added mass coefficients, $\alpha = 0$

Figure 5.44 shows the CF added mass coefficients found from combined CF/IL motions in Orientation 2 ($\alpha = 0$). The plot shows that the C_a values varies both with respect to A/D ratios and nondimensional frequencies. The C_a values ranges from -2 to 7 compared to the range -0.5 to 4 for the pure CF tests in Orientation 2.

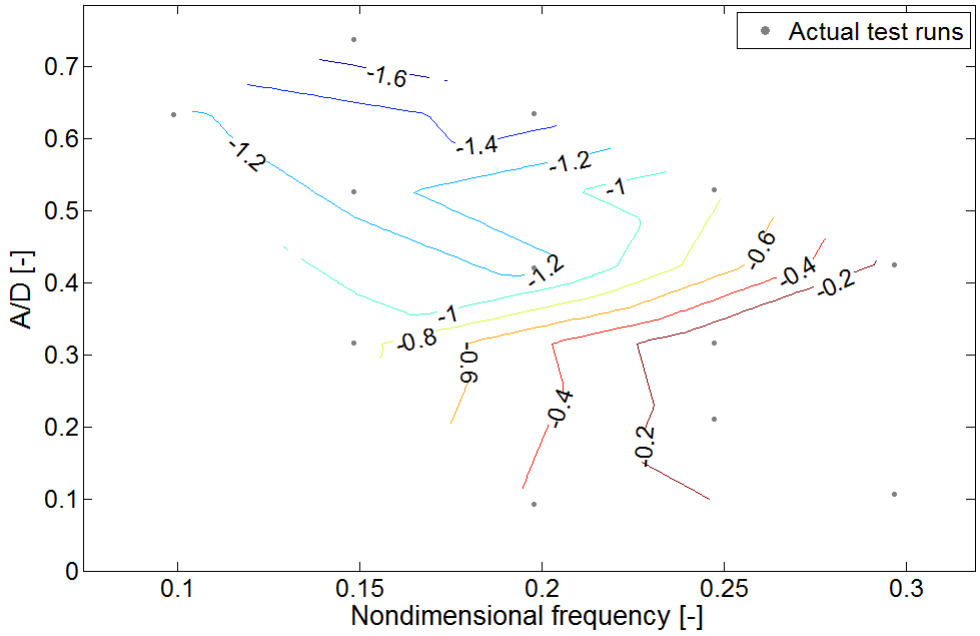

Figure 5.41: Contour plot of the IL excitation coefficients found for combined CF/IL motions ($\alpha = 0$) in Orientation 2.

Figure 5.45 shows the IL added mass coefficients found from combined CF/IL motions in Orientation 2 ($\alpha = 0$). The C_a values are increasing for increasing frequencies. This is also the trend for increasing A/D ratios up to about $A/D = 0.4$. It should be noted that the number of data points are limited as with the other combined CF/IL runs.

Drag coefficients, $\alpha = \pi$

Figure 5.46 shows the drag coefficients found from combined CF/IL motions in Orientation 2 ($\alpha = \pi$). The drag coefficients are increasing for both increasing amplitudes and frequencies. The lowest C_D value is 1.6 and the highest 2.5.

Drag coefficients, $\alpha = 0$

Figure 5.47 shows the drag coefficients found from combined CF/IL motions in Orientation 2 ($\alpha = 0$). The drag coefficients are increasing for increasing frequencies. This also seems to be the trend for increasing amplitudes except

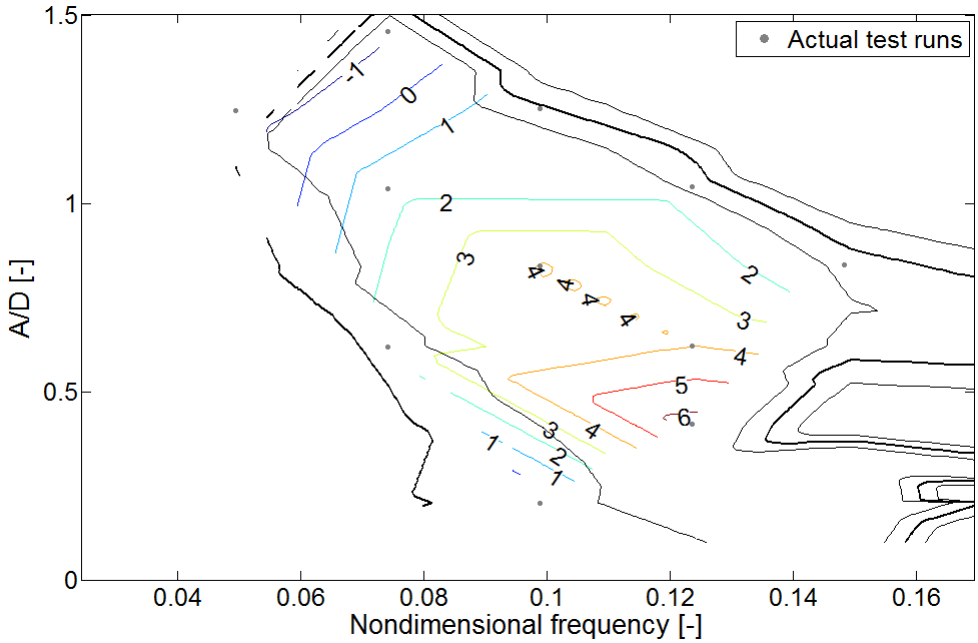

Figure 5.42: Contour plot of the CF added mass coefficients found for combined CF/IL motions ($\alpha = \pi$) in Orientation 2.

between approximately $A/D = 0.6$ and $A/D = 1.0$ for the lower frequencies. The minimum C_D value is 1.6 and the highest 2.6.

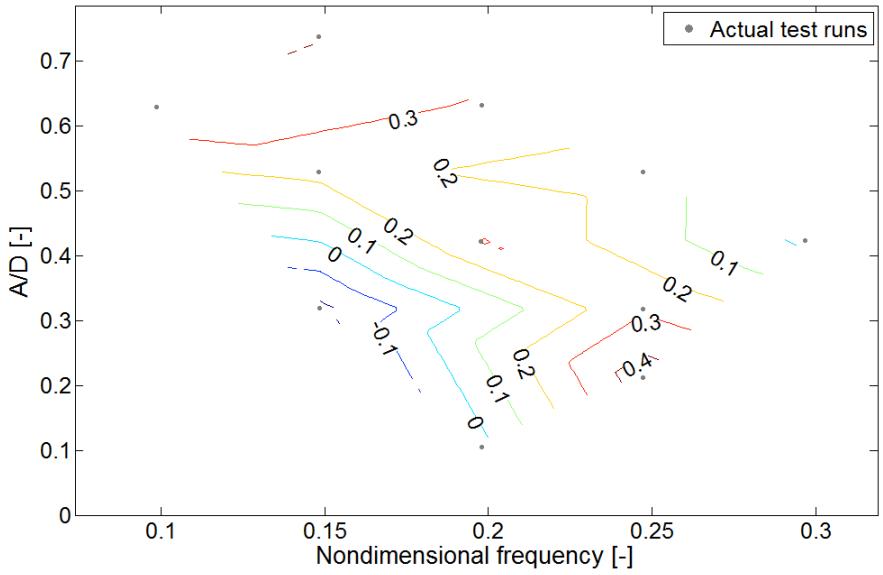

Figure 5.43: Contour plot of the IL added mass coefficients found for combined CF/IL motions ($\alpha = \pi$) in Orientation 2.

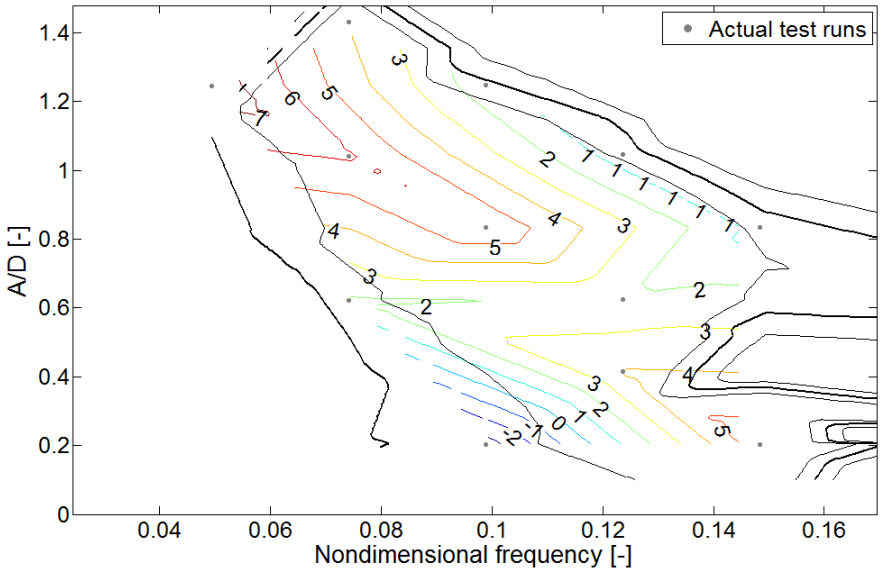

Figure 5.44: Contour plot of the CF added mass coefficients found for combined CF/IL motions ($\alpha = 0$) in Orientation 2.

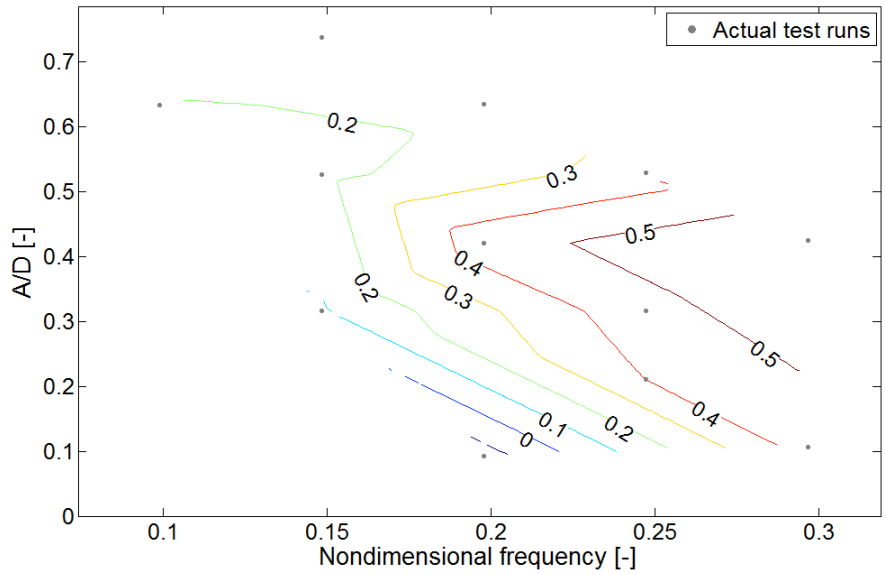

Figure 5.45: Contour plot of the IL added mass coefficients found for combined CF/IL motions ($\alpha = 0$) in Orientation 2.

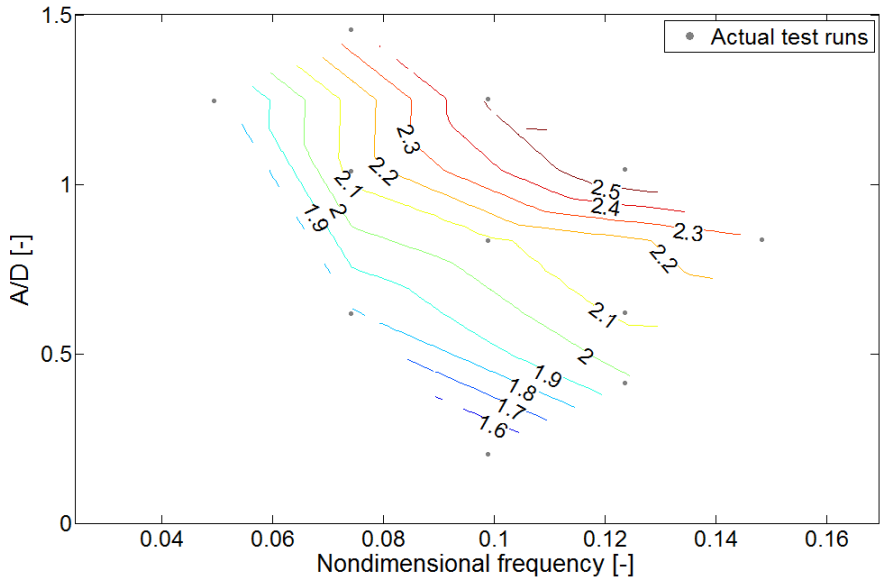

Figure 5.46: Contour plot of the drag coefficients found for combined CF/IL motions ($\alpha = \pi$) in Orientation 2. The axes represent CF A/D and nondimensional frequencies.

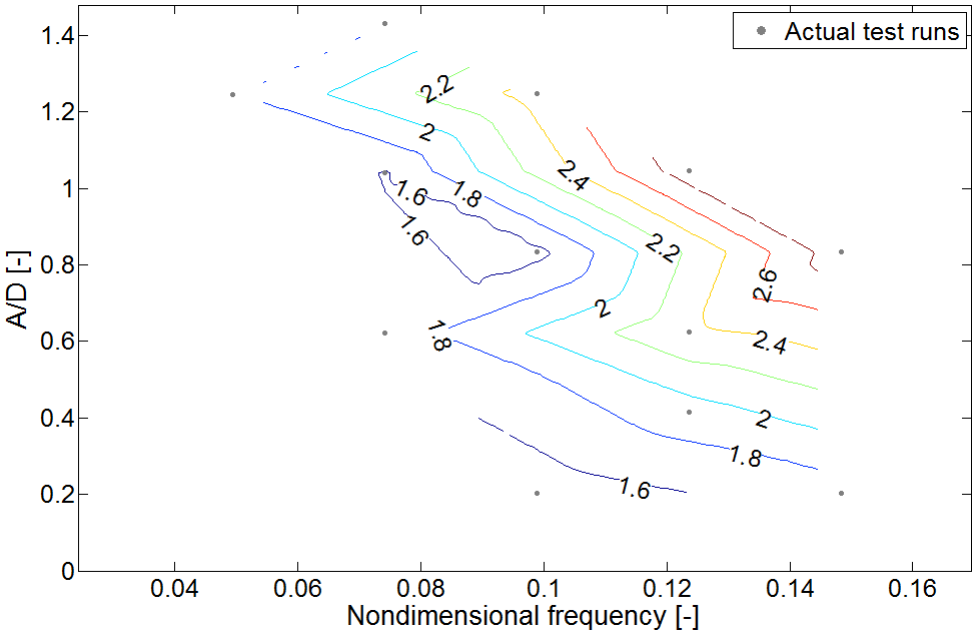

Figure 5.47: Contour plot of the drag coefficients found for combined CF/IL motions ($\alpha = 0$) in Orientation 2. The axes represent CF A/D and nondimensional frequencies.

5.8.6 Combined CF/IL tests in Orientation 3

Figure 5.48 shows the CF excitation coefficients found from combined CF/IL motions in Orientation 3 ($\alpha = \pi$). The part of the zero line found shows that the excitation region is reaching higher amplitudes than for the pure CF experiments in Orientation 3. The maximum value is found at $\hat{f} = 0.223$ and $A/D = 0.2$ and is $C_{e,CF} = 0.167$. Hence the excitation coefficients are small compared to what was found for Orientation 1 and 2. It should however be noticed that the number of data points are very few inside the excitation region.

Excitation coefficients, $\alpha = \pi$

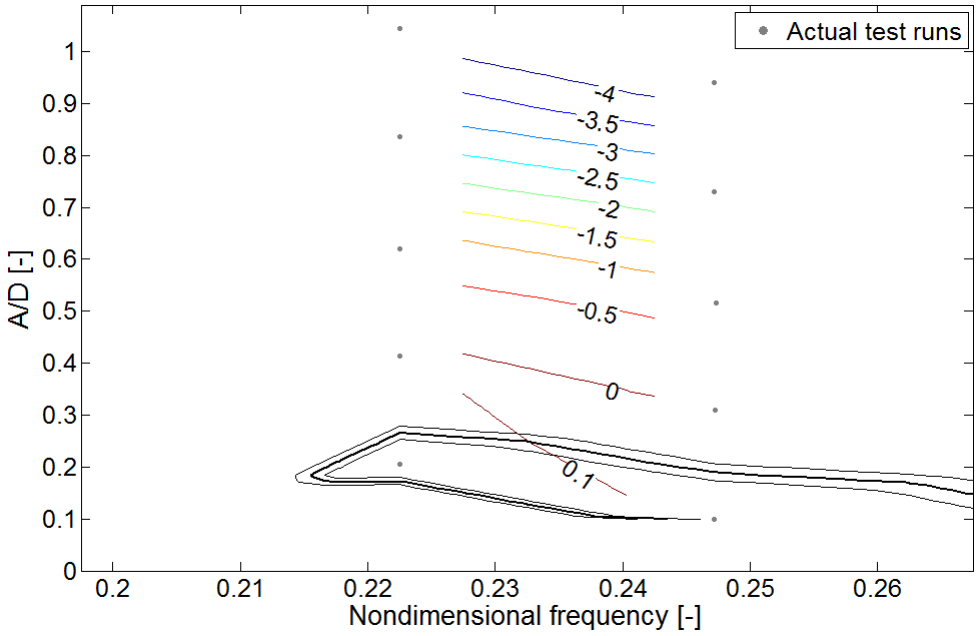

Figure 5.48: Contour plot of the CF excitation coefficients found for combined CF/IL motions ($\alpha = \pi$) in Orientation 3.

Figure 5.49 shows the IL excitation coefficients found from combined CF/IL motions in Orientation 3 ($\alpha = 0$). As in Orientation 1 and 2 no excitation region is found in the IL direction. This means that combined CF/IL motions with the given amplitudes and frequencies for $\alpha = \pi$ are

not realistic. Combined motions may occur for other A/D ratios and phase angles (α) however.

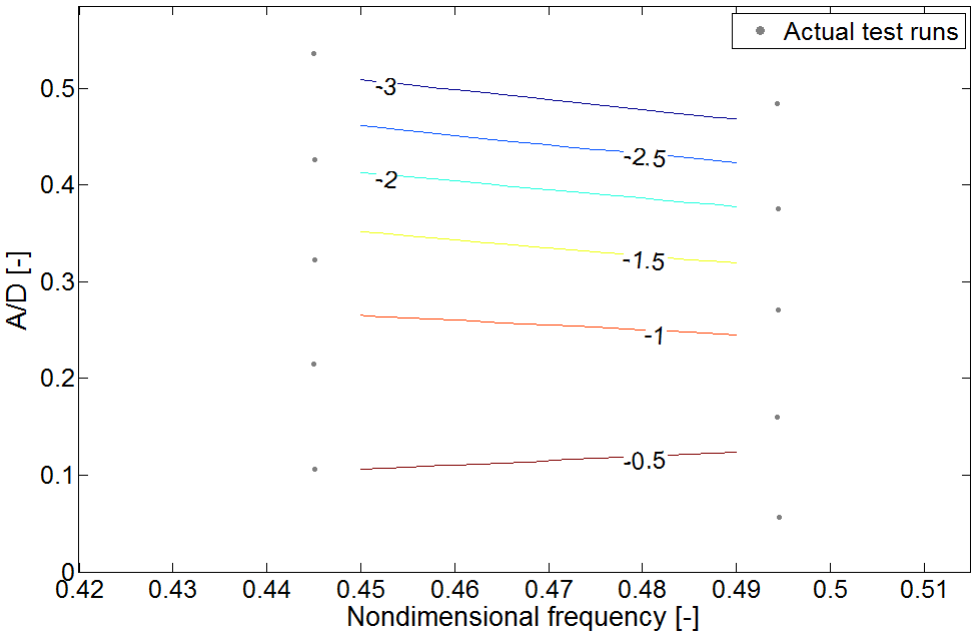

Figure 5.49: Contour plot of the IL excitation coefficients found for combined CF/IL motions ($\alpha = \pi$) in Orientation 3.

Excitation coefficients, $\alpha = 0$

Figure 5.50 shows the CF excitation coefficients found for combined CF/IL motions in Orientation 3 ($\alpha = 0$). The plot indicate that the excitation region is smaller than for the similar case with $\alpha = \pi$ but also compared to the pure CF case.

Figure 5.51 shows the IL excitation coefficients found for combined CF/IL motions in Orientation 3 ($\alpha = 0$). No positive excitation coefficient values are found, and hence the combined CF/IL motions are not realistic for the specific A/D values and phase angle ()$\alpha = 0$).

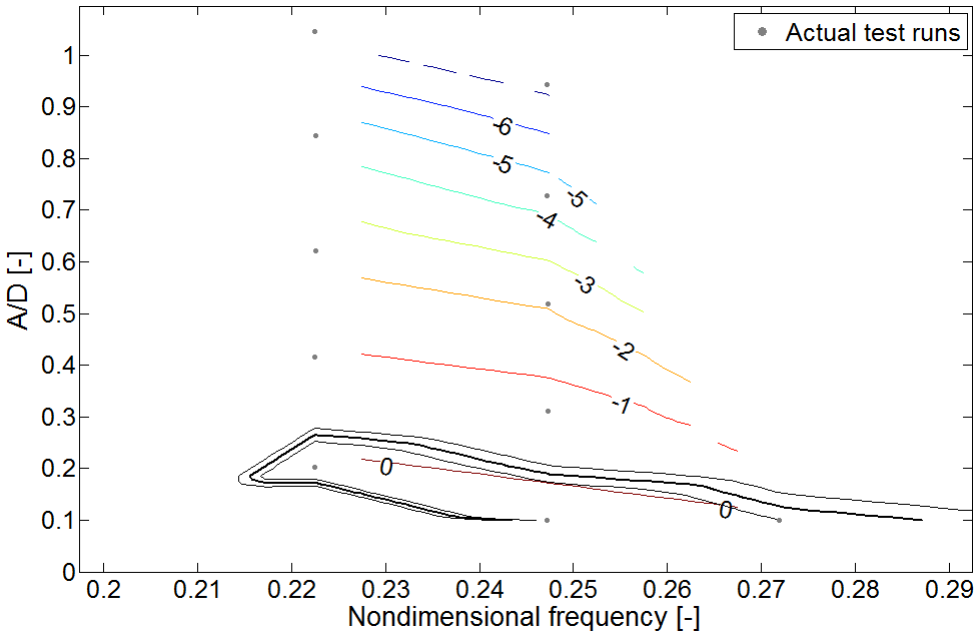

Figure 5.50: Contour plot of the CF excitation coefficients found for combined CF/IL motions ($\alpha = 0$) in Orientation 3.

Added mass coefficients, $\alpha = \pi$

The CF added mass coefficients presented in Figure 5.52 are found from combined CF/IL motions in Orientation 3 ($\alpha = \pi$). The added mass coefficients ranges from 0 to 1 approximately. Inside the excitation region the added mass value is about 1. In comparrison the added mass was approximately 0.5 inside the excitation region for the pure CF tests in Orientation 3.

Figure 5.53 shows the IL added mass coefficients found from combined CF/IL motions in Orientation 3 ($\alpha = \pi$). The added mass values ranges from 0.5 to 0.7 approximately.

Added mass coefficients, $\alpha = 0$

Figure 5.54 shows the CF added mass coefficients found from combined CF/IL motions in Orientation 3 ($\alpha = 0$). The added mass coefficients ranges from -0.2 to 0.8 approximately. It should be noted that the data are based on one extra test run compared to the similar test with $\alpha = \pi$. This was because the run with $\alpha = 0$ had some problems related to it.

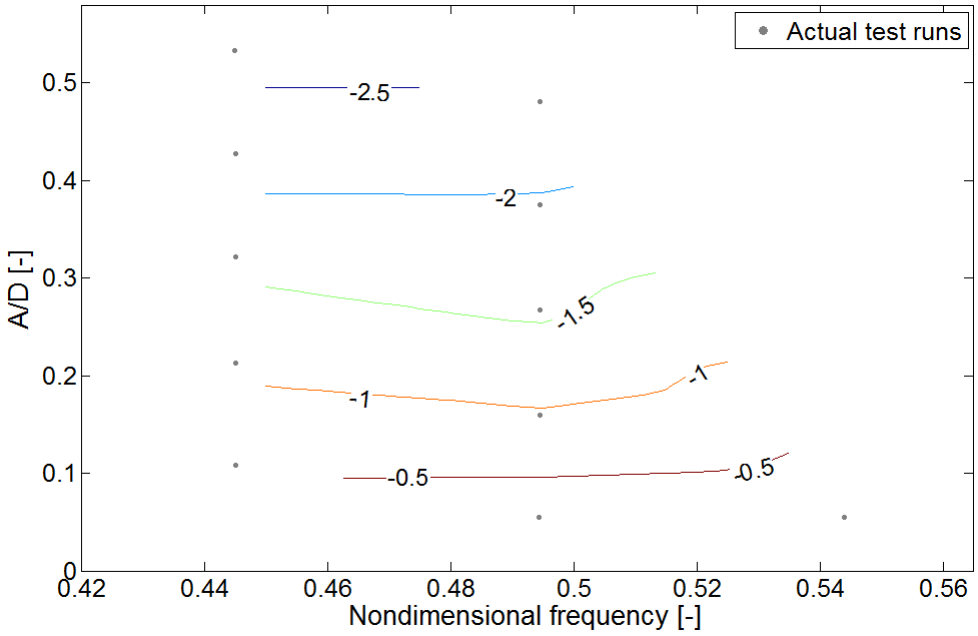

Figure 5.51: Contour plot of the IL excitation coefficients found for combined CF/IL motions ($\alpha = 0$) in Orientation 3.

Figure 5.55 shows the IL added mass coefficients found from combined CF/IL motions in Orientation 3 ($\alpha = 0$). The added mass coefficients ranges from 0.65 to 0.8 approximately.

Drag coefficients, $\alpha = \pi$

Figure 5.56 shows the drag coefficients found from combined CF/IL motions in Orientation 3 ($\alpha = \pi$). The drag coefficients show a strong amplitude dependence. The lowest C_D values are found for low A/D ratios with increasing magnitude for increasing amplitudes. The lowest C_D value is around 1 and the highest around 3.

Drag coefficients, $\alpha = 0$

Figure 5.57 shows the drag coefficients found from combined CF/IL motions in Orientation 3 ($\alpha = 0$). As with the similar runs with $\alpha = \pi$ the drag coefficients show a strong amplitude dependence. The magnitude is increasing for

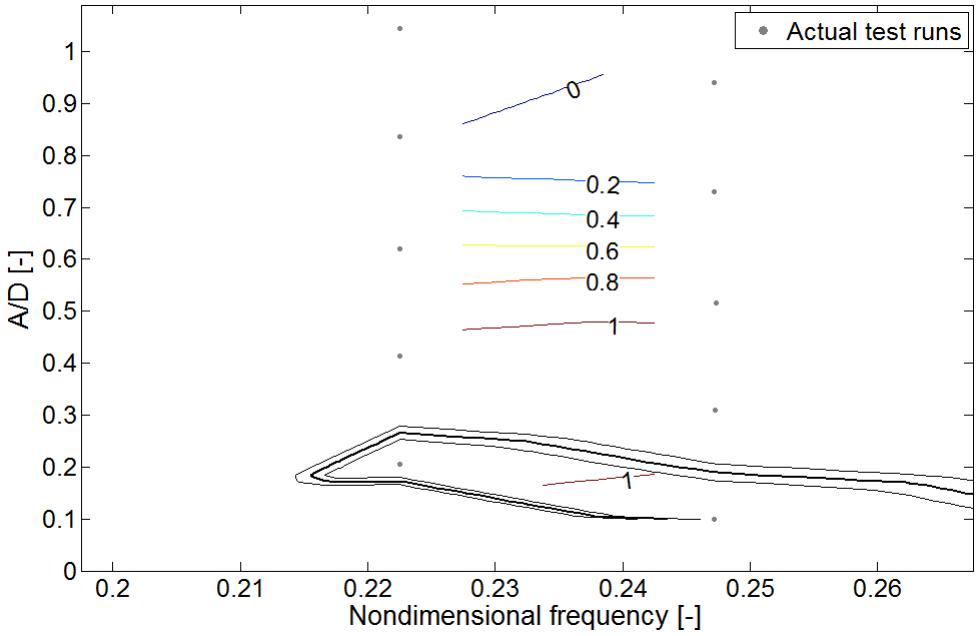

Figure 5.52: Contour plot of the CF added mass coefficients found for combined CF/IL motions ($\alpha = \pi$) in Orientation 3.

increasing amplitudes. The plot also shows a small frequency dependence, at least for A/D ratios below 0.3. The lowest C_D value is around 0.8 and the highest around 1.8.

Lift coefficients, $\alpha = \pi$

Figure 5.58 shows the lift coefficients (C_L) found from combined CF/IL motions in Orientation 3 ($\alpha = \pi$). The lift coefficients decreases in magnitude for increase amplitudes. At about $A/D = 0.35$ the lift coefficient changes sign, meaning that the lift force changes direction. The C_L values range between -0.6 and 0.6.

Lift coefficients, $\alpha = 0$

Figure 5.59 shows the lift coefficients (C_L) found from combined CF/IL motions in Orientation 3 ($\alpha = 0$). The lift coefficients decrease in magnitude for increasing A/D ratios up to about $A/D = 0.55$. Then from around

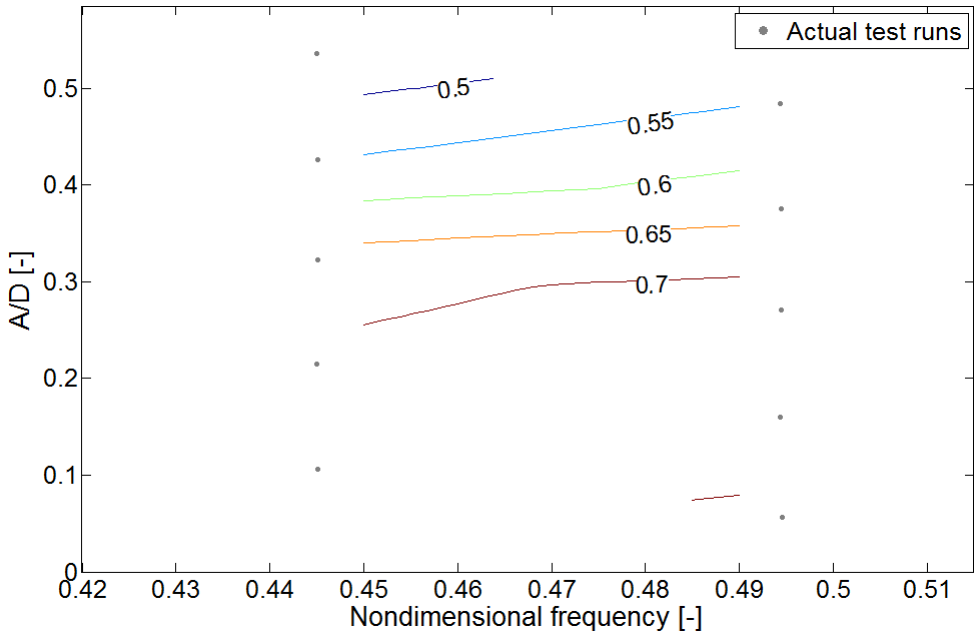

Figure 5.53: Contour plot of the IL added mass coefficients found for combined CF/IL motions ($\alpha = \pi$) in Orientation 3.

$A/D = 0.8$ the lift coefficients decreases for increasing amplitudes. Only positive C_L values are found, in contrast to the similar runs with $\alpha = \pi$.

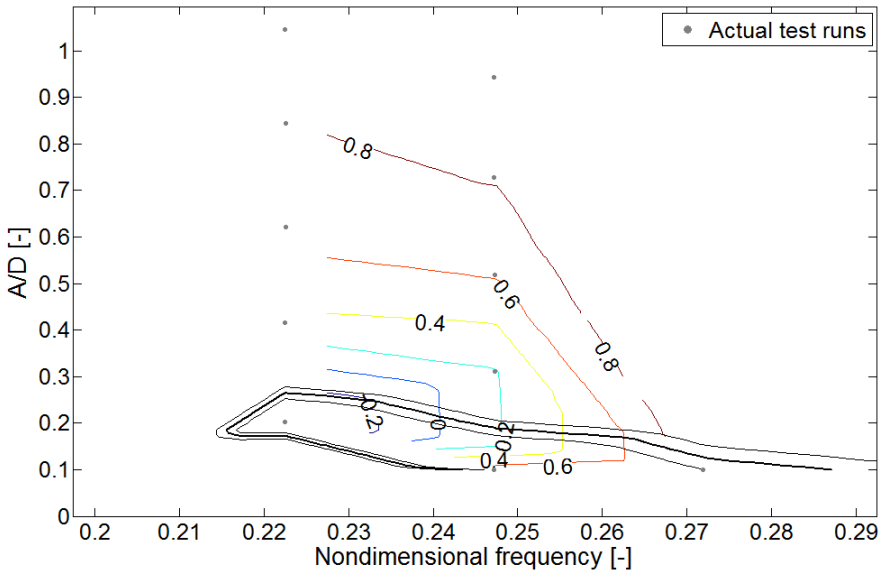

Figure 5.54: Contour plot of the CF added mass coefficients found for combined CF/IL motions ($\alpha = 0$) in Orientation 3.

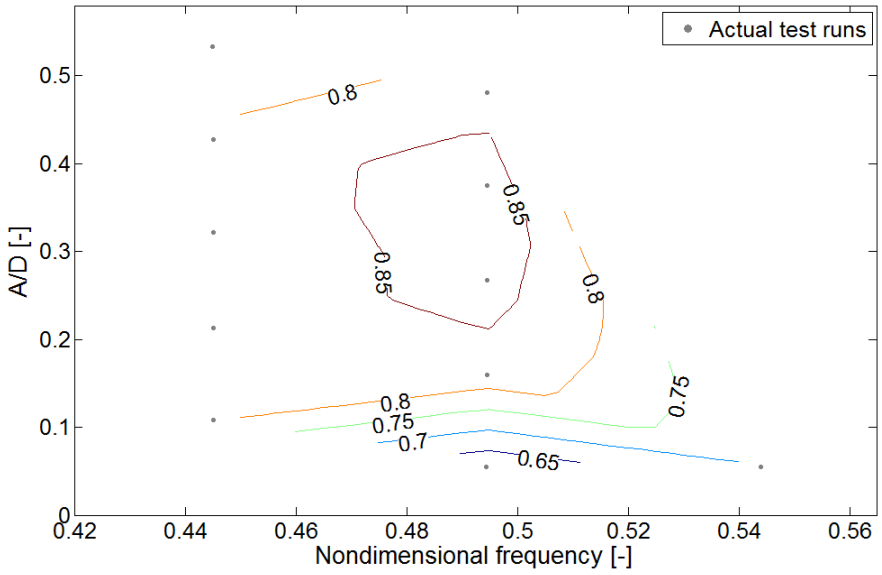

Figure 5.55: Contour plot of the IL added mass coefficients found for combined CF/IL motions ($\alpha = 0$) in Orientation 3.

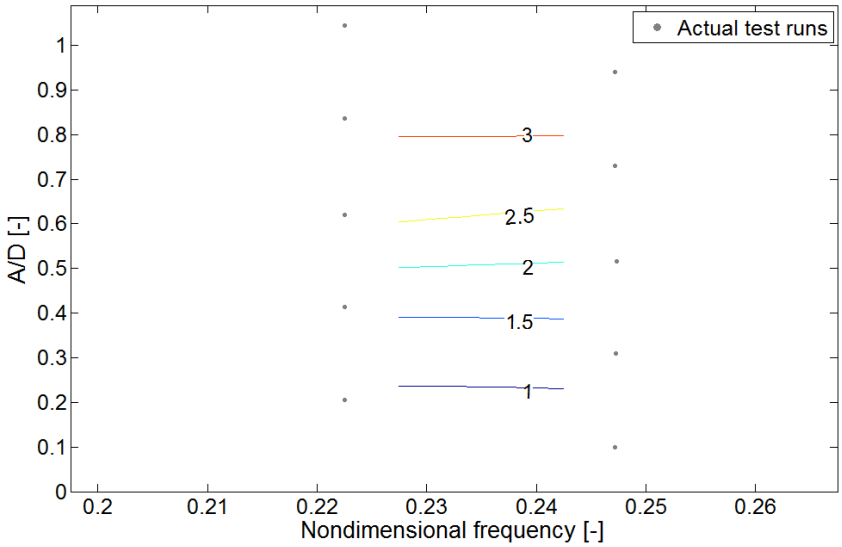

Figure 5.56: Contour plot of the drag coefficients found for combined CF/IL motions ($\alpha = \pi$) in Orientation 3. The axes represent CF A/D and nondimensional frequencies.

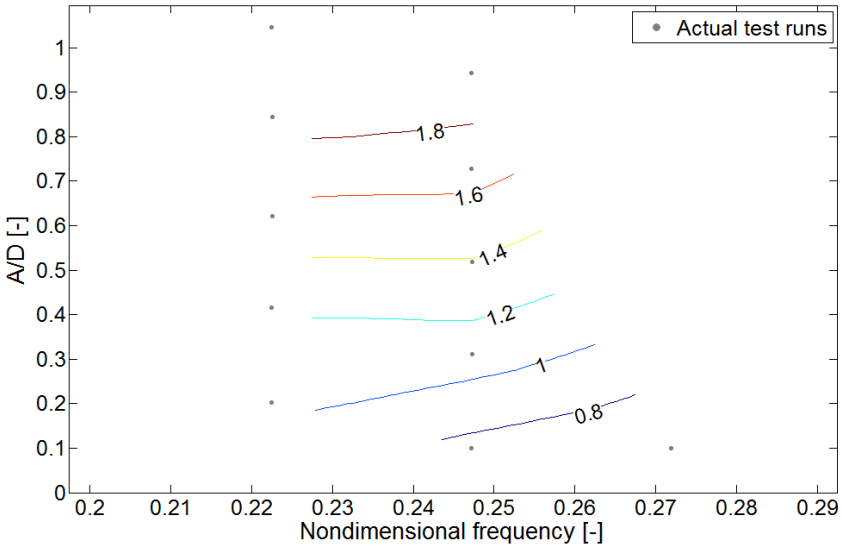

Figure 5.57: Contour plot of the drag coefficients found for combined CF/IL motions ($\alpha = 0$) in Orientation 3. The axes represent CF A/D and nondimensional frequencies.

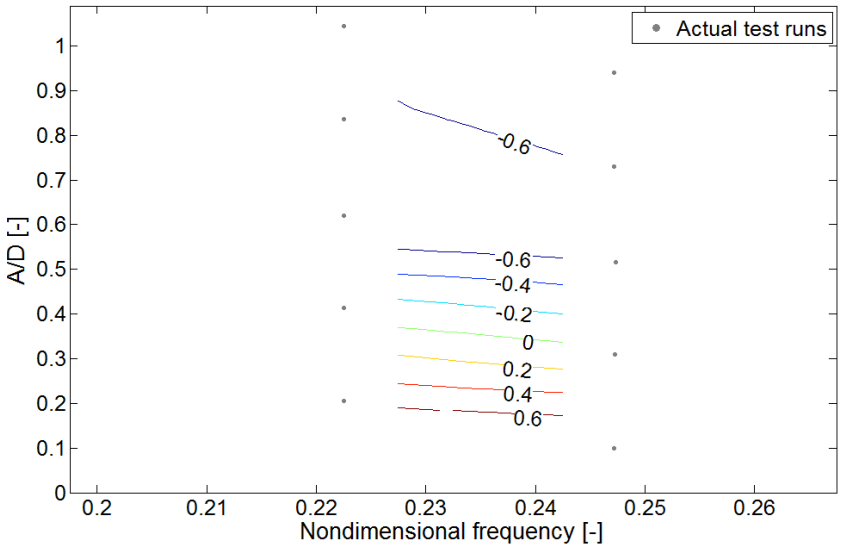

Figure 5.58: Contour plot of the lift coefficients found for combined CF/IL motions ($\alpha = \pi$) in Orientation 3. The axes represent CF A/D and nondimensional frequencies.

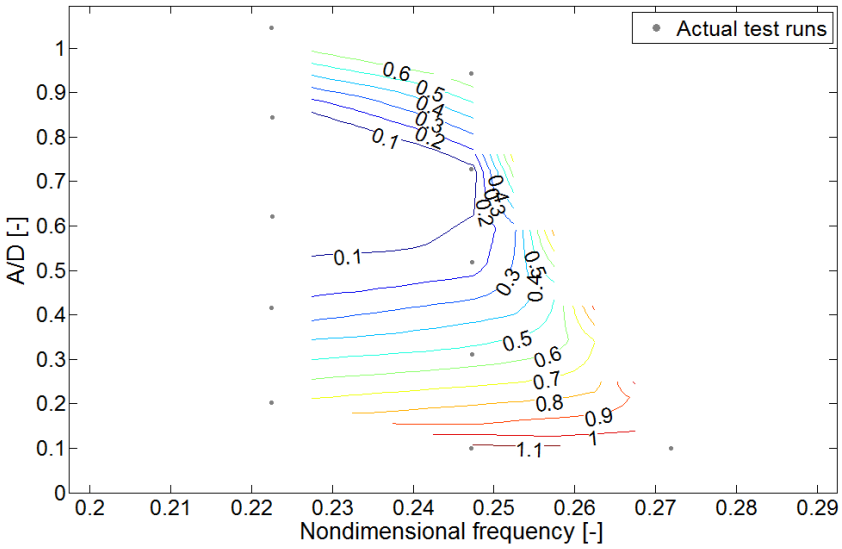

Figure 5.59: Contour plot of the lift coefficients found for combined CF/IL motions ($\alpha = 0$) in Orientation 3. The axes represent CF A/D and nondimensional frequencies.

Chapter 6

VIV analyses using VIVANA

The previous chapter described the experiments done with a bundle model of three pipes. The results from these experiments are used in the VIV analyses in VIVANA presented in this chapter. The only exception is the lift coefficient, which is not included due to the lack of support of lift coefficients in VIVANA.

As the experiments gave no excitation for the combined CF/IL tests, the VIV analyses have been done using pure CF only. The VIVANA analyses are using the same definition of orientations as discussed in Section 5.4.

The vertical stiffness from the springs discussed in Chapter 3 are used for the analyses where the artificial seabed is assumed connected to the floating bridge and tunnel. The artificial seabed may be detached from the floating bridge and tunnel up to a year during the installation phase (Reiso, 2015). Because of this, VIV calculations on the artificial seabed alone was also performed.

The models of the artificial seabed used in this chapter were based on the models build in the project thesis done by Grevstad (2014).

6.1 About the software

The software RIFLEX and VIVANA developed at MARINTEK has been used in the analyses. RIFLEX is used for modelling the artificial seabed and running static analyses. VIVANA is using the results from the INPMOD and STAMOD modules of RIFLEX to calculate vortex induced vibrations (Passano et al., 2014b). An illustration of the VIVANA and RIFLEX mod-

ules and their relationship is shown in Figure 6.1.

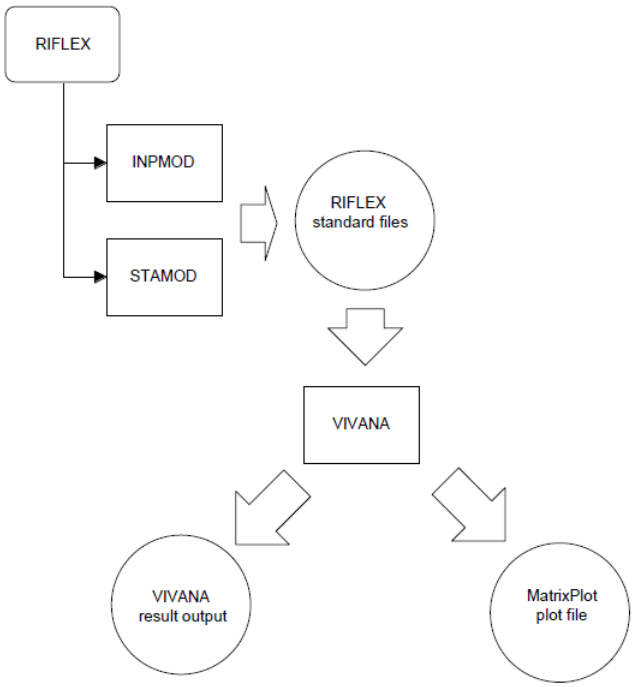

Figure 6.1: An illustration of the the VIVANA and RIFLEX modules and their relationship (Passano et al., 2014b).

The configurations of the software are done using one input file for each of the INPMOD, STAMOD and VIVANA modules.

For more information about the software it is referred to the RIFLEX and VIVANA manuals.

6.2 The artificial seabed models

Two models were used in the calculations: a simplified and full model. The simplified model was necessary to calculate VIV using VIVANA. This is because VIVANA will have some problems with the complexity of the full model (Grevstad, 2014). The main aspects of the two models are discussed in the following sections. For more details of the two models, it is referred to the project thesis (Grevstad, 2014).

6.2.1 The full model

The full model includes the two bundles of the artificial seabed and all the 13 cross pipes. Thus the full model will look similar to the artificial seabed illustration in Figure 2.2. The same coordinate system as in Figure 2.2 is used for the full model. The model is build using lines and nodes in RIFLEX. A total of 41 lines and 30 nodes were used.

6.2.2 The simple model

The simple model was based on the symmetric properties of the artificial seabed. The model contains only one line representing one bundle, and the cross pipes were modelled as consentrated loads. An illustration of the simple model is shown in Figure 6.2.

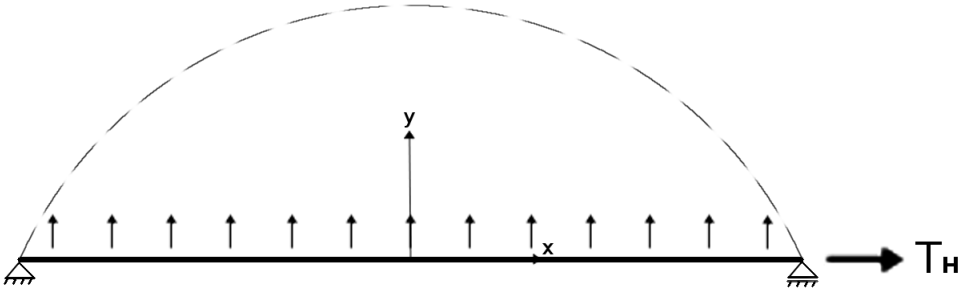

Figure 6.2: An illustration of the simple model of the artificial seabed. The stippled lines represent the model after static deformation. Please notice that the length/width ratio in the figure is different from the real model.

It should be noticed from Figure 6.2 that the coordinate system is different from the coordinate system used in the full model. The forces representing the cross pipes are taken from the static analysis of the full model, and will vary in magnitude along the x-direction.

6.2.3 Analysis procedure using the two models

The VIV analyses of each case were done using the following procedure:

1. Static analysis of the artificial seabed under the relevant current conditions, using the full model in RIFLEX.

2. Configuration of the simple model with the forces found from the previous step.

3. If the analysis was including the stiffness from the floating bridge and tunnel, the springs from Chapter 3 were added to the simple model.

4. Static analysis in RIFLEX using the simple model.

5. Adding the relevant data found from the experiments in Chapter 5 to VIVANA.

6. Run the VIVANA analysis.

The static analysis done in step 1 is necessary to find the pre-tension and forces from the cross pipes to be used in the simple model. These forces will vary with the current condition and orientation of the bundle. This is due to the change in drag force. The drag coefficients used for the three orientations are different, as was seen from the experiments in Chapter 5. It should be noted that the simple model must be configured with the same current and drag coefficient as in the static analysis with the full model.

For analyses where the artificial seabed is assumed connected to the floating bridge and tunnel, the springs from Chapter 3 are included. The vertical stiffness used are taken from table 3.2 and 3.3 in Section 3.3.2.

The excitation and added mass coefficients found from the experiments in Chapter 5 are added to the VIVANA configuration. These coefficients are different in each orientation. Also the Strouhals numbers found from the experiments are added to VIVANA.

All the VIVANA analyses are run both using the space sharing and time sharing methods discussed in Section 4.3.5.

6.3 Current profiles

A current profile was specified for each VIV analysis in VIVANA. It was decided to do analyses with two different current profiles, in each orientation. The reason for using two current profiles was to see the difference in the VIV results of the two cases. The two current profiles are shown in Figure 6.3.

Current Profile 1 from Figure 6.3 was based on taking the largest current velocity at 30m depth ($0.55\frac{m}{s}$) for the Sognefjord. This is found from Table 2.6 in Section 2.3. The choice of current velocity was conservative. The

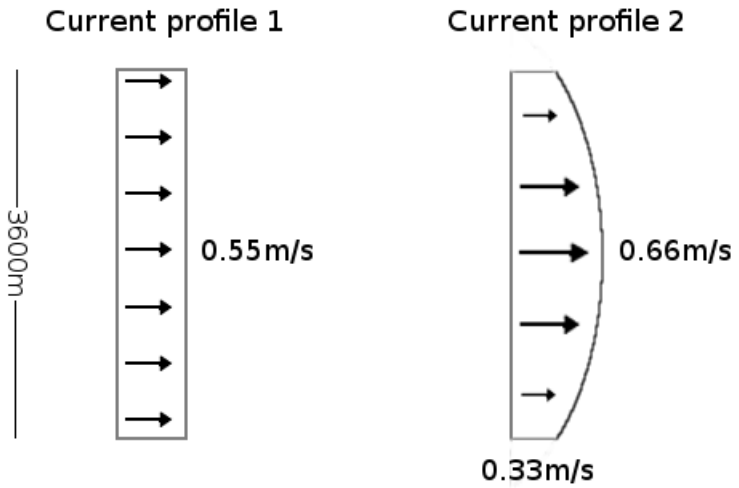

Figure 6.3: The two current profiles used in the VIVANA analyses.

choice is conservative because the vortex shedding frequency will increase for increasing current velocity (Larsen, 2010), as discussed in Chapter 4.

Current Profile 2 was based on Current Profile 1 by keeping the mass rate constant across the fjord. The profile was made to have the biggest velocity at the midpoint of the fjord. This is probably a more realistic choice since the current velocity is found by SINTEF to be largest in the middle. The current velocity function for Current Profile 2 is defined as a parabolic function on the form:

$$f_{curr2}(x) = a(x_0^2 - x^2) + C \tag{6.1}$$

Where x ranges from -1802m to 1802m as shown in Figure 2.2 in Section 2.1. C is a constant and represents the velocity at the ends of the fjord. It was decided to make a profile where C is equal to half the velocity at the midtpoint of the fjord ($x = 0$):

$$f_{curr2}(x = 0) = a \cdot x_0^2 + C = 2 \cdot C \tag{6.2}$$

Rearranging Equation 6.2 and inserting for x_0 gives:

$$C = a \cdot x_0^2 = (1802m)^2 \cdot a \tag{6.3}$$

The water transport per second should be the same for the two current profiles. This gives the equation:

$$\int_{-1802m}^{1802m} a((1802m)^2 - x^2) + C dx = U_o \cdot 3604m = 0.55m/s \cdot 3604m = 1982.2\frac{m^2}{s} \tag{6.4}$$

Insert the value of C from Equation 6.3 into Equation 6.4 gives:

$$\int_{-1802m}^{1802m} a((1802m)^2 - x^2) + a \cdot (1802m)^2 dx = \int_{-1802m}^{1802m} a((2 \cdot 1802m)^2 - x^2) dx = 1982.2\frac{m^2}{s} \tag{6.5}$$

Solving Equation 6.5 with respect to a gives:

$$a = \frac{1982.2\frac{m^2}{s}}{\int_{-1802m}^{1802m}((2 \cdot 1802m)^2 - x^2)dx} = 1.0163 \cdot 10^{-7}\frac{1}{ms} \tag{6.6}$$

The current velocity function for Current Profile 2 is then given by:

$$f_{curr2}(x) = a(x_0^2 - x^2) + C = 1.0163 \cdot 10^{-7}\frac{1}{ms} \cdot ((1802m)^2 - x^2) + 0.33\frac{m}{s} \tag{6.7}$$

It should be noticed that the function $f_{curr2}(x)$ is using a coordinate system different from Figure 2.2. This was because the function is defined in MATLAB as a matrix, and the index x must be a positive integer.

The current velocities used in VIVANA (defined in the RIFLEX module) can be specified in two ways (*RIFLEX User Manual*, 2014). The first option is to specify a constant current profile. This was the chosen option for Current Profile 1.

The second alternative is to use what is referred to as current lines in VIVANA. When using current lines, current profiles are defined at multiple points. The current velocities between these points are found by linear interpolation (*RIFLEX User Manual*, 2014). VIVANA has a limit of maximum 9 current lines. Hence Curent Profile 2 was made selecting 9 values from the function $f_{curr2}(x)$ and add as current lines. The current velocities used from the function $f_{curr2}(x)$ are presented in table 6.1.

The coordinate system used in Table 6.1 is the same as in Figure 2.2.

The linear interpolation between the values will introduce an error compared to the current profile presented in Figure 6.3. This error is however assumed acceptable for these analyses.

Table 6.1: Current velocities used for Current Profile 2

x-coordinate [m]	Current velocity [m/s]
-1802	0.330
-1350	0.474
-900	0.5773
-450	0.6393
0	0.6600
450	0.6393
900	0.5773
1350	0.474
1802	0.330

6.4 Data used from the experiments

The experiments described in Chapter 5 gave some data that were used in the VIV analyses. The data were the excitation, added mass and drag coefficients. The Strouhals number found in each orientation was also used.

6.4.1 Excitation coefficients

The excitation coefficients found in the experiments described in Chapter 5 were used instead of the default coefficients in VIVANA. The data were added to the VIVANA analysis by specifying the following four parameters for each nondimensional frequency ($\hat{f}$), inside the excitation region:

- $\frac{A}{D}$ ratio for when the excitation coefficient is 0 at the given $\hat{f}$.
- $\frac{A}{D}$ ratio for when the excitation coefficient has its maximum at the given $\hat{f}$.
- The value of the maximum excitation coefficient at the given $\hat{f}$.
- The excitation coefficient value when $\frac{A}{D} = 0$ at the given $\hat{f}$.

The parameters above were then used by VIVANA to make excitation coefficient curves. These curves are described more in detail in Section 4.3.3.

6.4.2 Added mass coefficients

The added mass coefficients found from the experiments were added to the VIVANA analyses instead of the default values. VIVANA only supports one single added mass coefficient per nondimensional frequency, as described in Section 4.3.1. Hence the added mass coefficients have to be determined from the countour plots using a chosen $\frac{A}{D}$ ratio.

The added mass coefficient for still water was specified in the static calculations in RIFLEX. The still water C_a value was found by taking the added mass value at the highest nondimensional frequency ($\hat{f}$) in the countour plot of the relevant orientation. This was because the nondimensional frequency is inversely proportional to the current speed (U), as shown in Equation 4.7.

6.4.3 Strouhals number

As described in Section 4.3.6, Strouhals number (St) is a function of Reynolds number (Re). Custom values of St can be specified in VIVANA in two ways:

- A constant value of St for all values of Re
- A custom St curve as a function of Re

The Strouhals number for the bundle was found in each orientation from the stationary test runs presented in Chapter 5. All the runs were done at a Reynolds number of approximately $2.0 \cdot 10^4$. Hence there was no data of the Strouhals number for higher or lower Re values.

The choice of what St values to use was based on comparing the Strouhals number from the experiments with the Strouhals number of a circular cylinder at the relevant Reynolds number. If the Strouhals number of the bundle was significantly higher or lower than for a circular cylinder at this Re, the measured St value of the bundle was used for all Reynolds numbers. For a circular cylinder, St is increasing for increasing values of Re. Hence this choice would probably be conservative for low values of Re, but underestimate at values of Re above $2.0 \cdot 10^4$. If the Strouhals number was approximately the same as for a circular cylinder, at a Re of $2.0 \cdot 10^4$, the default St curve presented in Section 4.3.6 was used.

6.4.4 Drag coefficients

The drag coefficients from the stationary bundle runs done in the experiments described in Chapter 5 were used in the static calculations. For each analysis a static calculation was done both for the full model and simple model. Thus the drag coefficient had to be included for both the models.

6.4.5 The hydrodynamic diameter

The hydrodynamic diameter used in the VIVANA analyses was calculated from Equation 6.8:

$$D_{H,fullscale} = 2.1547 \cdot D_{pipe,fullscale} = 2.1547 \cdot 0.9144m = 1.970m \qquad (6.8)$$

Equation 6.8 is the same as Equation 5.6, except that the outer diameter of a pipe in the full scale bundle was used as the diameter (see Table 2.1).

6.5 VIV analyses of pure CF in Orientation 1

This section describes the setup and results from the pure CF analyses done in Orientation 1 in VIVANA. The analyses were done using the procedure described in Section 6.2.3. This procedure includes a static analysis in RIFLEX for the full and simple model, and a VIVANA analysis using the simple model.

6.5.1 Experimental results used in the static analysis

The following values from the experiments in Orientation 1 were used for the static analyses in RIFLEX:

Table 6.2: Parameters from the experimental results used in the static analysis in RIFLEX.

Parameter	Value
C_D	1.1 [-]
$C_{a,CF}$ (still water)	0.75 [-]

The values in Table 6.2 were added to the static analysis in both the full and simple model.

6.5.2 Excitation coefficients and excitation region used in the VIVANA analyses

Figure 6.4 shows the countour plot of the excitation coefficients found from the experiments in Orientation 1. The borders of the excitation region used in the VIVANA analyses are shown as red lines.

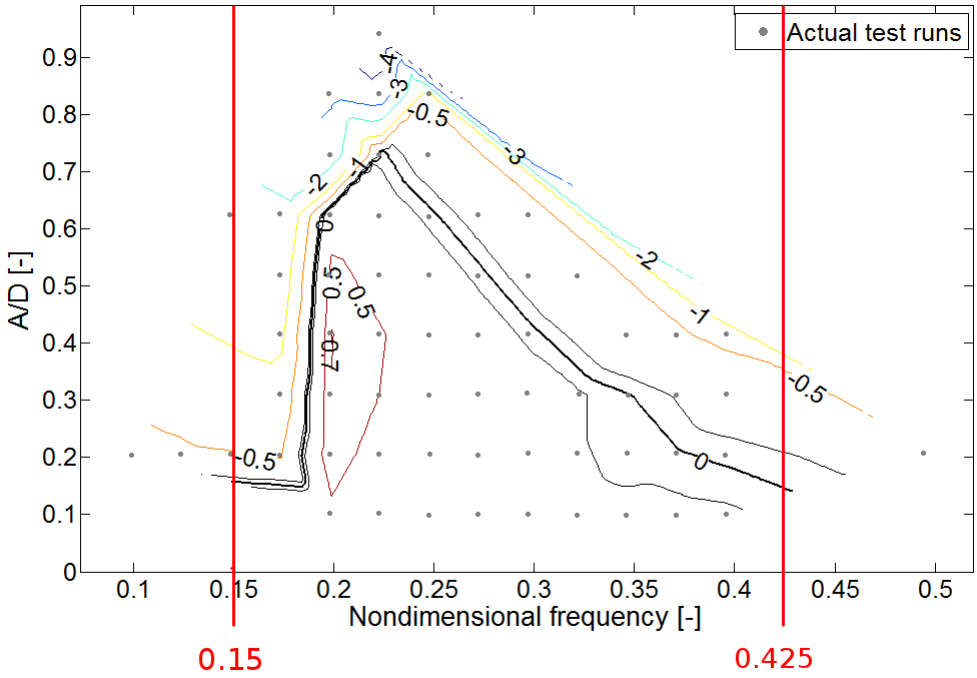

Figure 6.4: The excitation region used for the Orientation 1 VIVANA analyses.

The excitation coefficient curves described in Section 6.4.1 were build for each frequency in the excitation region ($\hat{f}$ between 0.15 and 0.425). This gave a total of 56 excitation coefficient curves for Orientation 1. It should be noted that the resolution of the matrix with the interpolated C_e values was 0.005. The contour plot was made from this matrix.

6.5.3 Added mass coefficients in the VIVANA analyses

As described in Section 4.3.1 VIVANA is limited to use only one added mass coefficient per nondimensional frequency in its calculations. Figure 6.5 shows that the added mass coefficients in Orientation 1 were selected at an A/D ratio of 0.45.

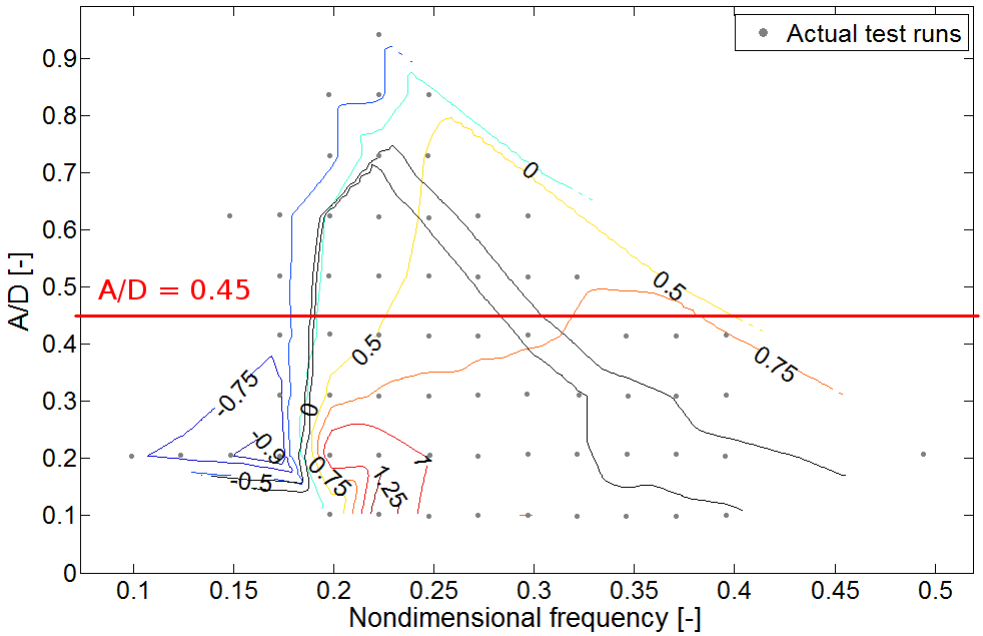

Figure 6.5: The added mass used for Orientation 1 VIVANA analysis.

The A/D ratio was selected to be approximately in the middle of the excitation zone. It should be mentioned that it is no clear rule to where the A/D ratio should be set.

6.5.4 Strouhals number and drag coefficient for the VIVANA analyses

As described in Section 5.8.1, the Strouhals number was found to be 0.213 in Orientation 1. This is about the same value as the default Strouhals curve in VIVANA has at the same Reynolds number ($Re \approx 2.0 \cdot 10^4$). Hence it was decided to use the default Strouhals number curve in VIVANA (see Section 6.4.3).

6.5.5 VIV results from VIVANA in Orientation 1

In total 8 VIV analyses were done in Orientation 1. The analyses were done using both the space sharing and time sharing methods discussed in Chapter 4. The results from the two methods are presented in Table 6.3 and 6.4.

Table 6.3: VIV results in Orientation 1 using the space sharing method.

Current profile	Springs	Dominating mode	Fatigue life [years]
1	no	4	$0.35928 \cdot 10^6$
1	yes	1	$0.25852 \cdot 10^6$
2	no	4	$0.27456 \cdot 10^6$
2	yes	1	$0.25999 \cdot 10^6$

Table 6.4: VIV results in Orientation 1 using the time sharing method.

Current profile	Springs	Dominating mode	Fatigue life [years]
1	no	4	$0.30831 \cdot 10^6$
1	yes	1	$0.23919 \cdot 10^6$
2	no	4	$0.24240 \cdot 10^6$
2	yes	1	$0.24040 \cdot 10^6$

It is noted from Table 6.3 that the lowest fatigue life found, using the space sharing method, was for the case of constant current velocity and springs attached. The springs represent the stiffness from the mounting bars between the artificial seabed and the floating bridge and tunnel (see Chapter 3). The fatigue life is calculated as the inverse of the maximum fatigue damage in the analysis. The maximum fatigue damage was found on an element where one of the springs are attached. This shows that the springs can give large local stresses.

The potential response frequencies found for the case with constant current velocity and no springs attached are shown in Table 6.5.

The ranking of the response frequencies are based on the calculation of the excitation parameter from Equation 4.8. In an uniform flow, $(A/D)_{Ce=0}$ is the only parameter different for the response frequencies (Passano et al., 2014a). Figure 6.6 shows the approximate $(A/D)_{Ce=0}$ values for the response frequencies.

The nondimensional frequencies were calculated using Equation 4.7 with $D_H = 1.97m$ and $U_N = 0.55m/s$. It can be seen from Figure 6.6 that mode

Table 6.5: Potential response frequencies found with constant current velocity and no springs attached

Mode no.	$f_{osc}[Hz]$	$\hat{f}[-]$	Rank	$L_{exc.zone}[m]$
1	0.0271	0.097	7	0
2	0.0522	0.187	4	3604
3	0.0545	0.195	2	3604
4	0.0639	0.229	1	3604
5	0.0772	0.277	3	3604
6	0.0895	0.321	5	3604
7	0.1045	0.374	6	3604

number 4 has the highest $(A/D)_{Ce=0}$ and hence will get the highest excitation parameter score , and thus rank. The same relationship between $(A/D)_{Ce=0}$ and rank is seen for the other modes as well. It is also seen from Figure 6.6 that mode number 1 is outside the excitation region.

By comparing the results in Table 6.3 and 6.4 it is noticed that the time sharing method gives a shorter fatigue life than the space sharing method. One reason for this could be that in time sharing, many of the respone frequencies get to dominate for a certain amount of time, as described in Section 4.3.5. Hence the higher order modes will contribute to the fatigue damage. For the case of an uniform flow with no springs attached, all the response frequencies inside the excitation region have an excitation zone length of 3604m. This means that the higher order modes will get to act along the whole length of the artificial seabed. In the space sharing method, mode number 4 will occupy the whole length of the model and no other modes will get an excitation length.

6.6 VIV analyses of pure CF in Orientation 2

This section presents the VIV analyses in Orientation 2 done in VIVANA. The methods used are the same as in Orientation 1.

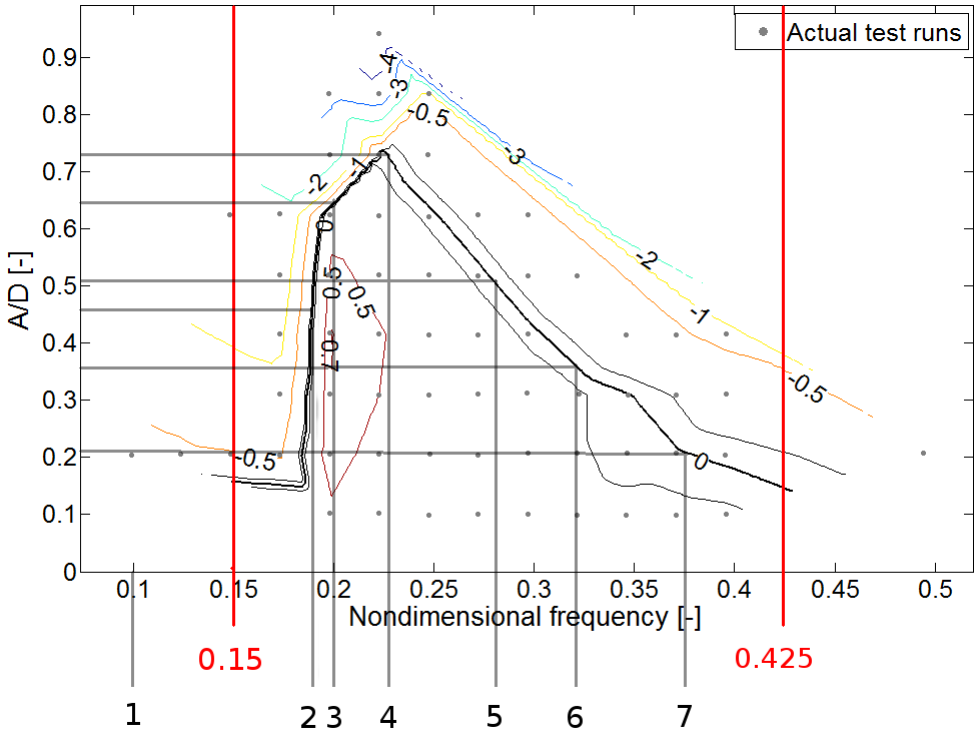

Figure 6.6: The approximate $(A/D)_{Ce=0}$ values of the response frequencies. The numbering refers to the mode number of the response frequencies.

6.6.1 Experimental results used in the static analyses

The drag and added mass coefficients used in the static analyses in Orientation 2 are presented in Table 6.6.

The drag coefficient (C_D) in Table 6.6 is the same as the one calculated from the stationary bundle runs in Orientation 2. The added mass coefficient in still water (C_a) is found by taking the added mass from the contour plot shown in Figure 5.22 where the nondimensional frequency is the highest.

6.6.2 Excitation coefficients and excitation region used in the VIVANA analyses

Figure 6.7 shows the countour plot of the excitation coefficients from the experiments with the excitation region used in this analysis.

Table 6.6: Coefficients from the experimental results used in the static analysis in Orientation 2.

Parameter	Value
C_D	1.5 [-]
$C_{a,CF}$ (still water)	1.1 [-]

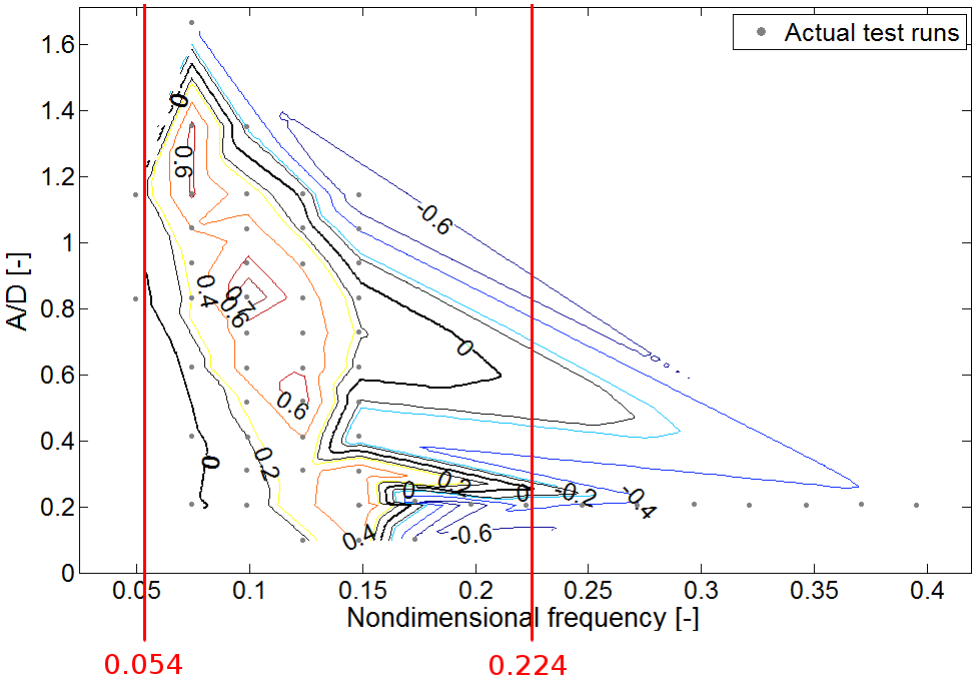

Figure 6.7: The excitation region used for Orientation 2 VIVANA analysis.

The excitation coefficient curves were build for each frequency in the excitation region ($\hat{f}$ between 0.054 and 0.224). This gave a total of 35 excitation coefficient curves.

6.6.3 Added mass for the VIVANA analyses

As described in Section 6.4.2 VIVANA is limited to use only one added mass coefficient per nondimensional frequency in its calculations. Figure 6.8 shows that the added mass coefficients for Orientation 1 were selected at an A/D ratio of 0.6.

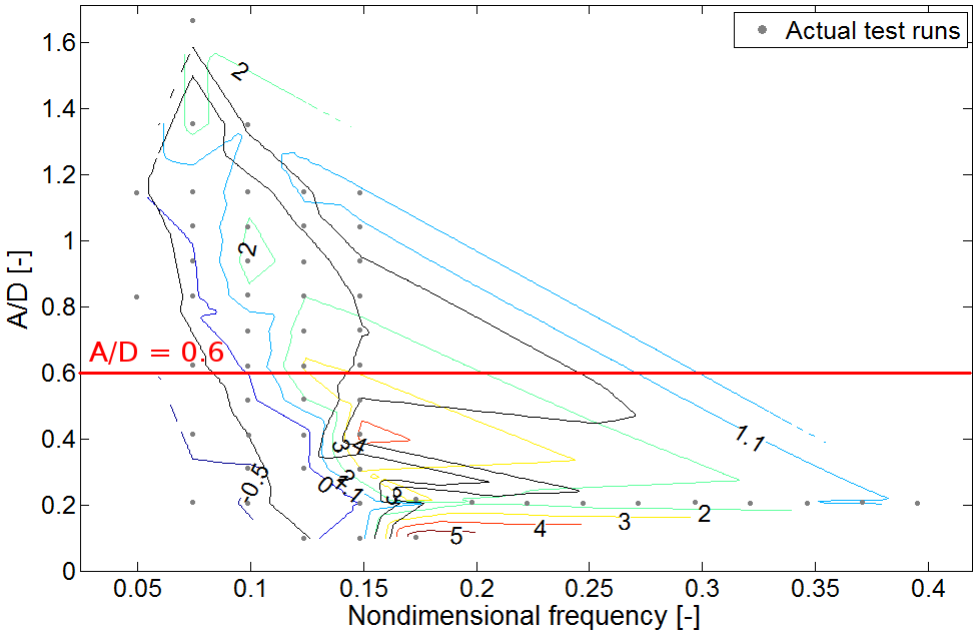

Figure 6.8: The added mass used for Orientation 2 VIVANA analysis.

The A/D ratio was used as an compromise between the lower and higher A/D ratios. As previously discussed it is no clear rule to where this A/D ratio should be.

6.6.4 Strouhals number and drag coefficient for the VIVANA analyses

The Strouhals number was found to be 0.178 in Orientation 2, as described in Section 5.8.2. This is significantly lower than the default Strouhals curve in VIVANA for the same Reynolds number $Re \approx 2.0 \cdot 10^4$. The Strouhals number in Orientation 2 is unknown for other Re values. It may however be assumed that the St will be lower than the default curve for other Re too. Due to this the Strouhals number has been set to be a constant 0.178 for all Re.

6.6.5 VIV results for Orientation 2

The results from the VIVANA analyses using the space sharing and time sharing methods are presented in Table 6.7 and 6.8 respectively.

Table 6.7: VIV results for Orientation 2 using the space sharing method.

Current profile	Springs	Dominating mode	Fatigue life [years]
1	no	1	n/a
1	yes	n/a	n/a
2	no	1	n/a
2	yes	n/a	n/a

Table 6.8: VIV results for Orientation 2 using the time sharing method.

Current profile	Springs	Dominating mode	Fatigue life [years]
1	no	1	$0.27536 \cdot 10^6$
1	yes	n/a	n/a
2	no	1	$0.28485 \cdot 10^6$
2	yes	n/a	n/a

Table 6.7 shows that VIV may only occur for the cases with no springs attached to the model. However the amplitudes of the active modes (mode number 1) are so small that VIVANA skips the fatigue damage calculation (knowing the damage will be very small). Hence the "n/a" under the fatigue life column. No VIV occurs when the artificial seabed model is connected to the springs.

Table 6.8 shows that VIV is possible for the cases without springs attached, and the amplitudes are big enough to give a fatigue damage (and thus a fatigue life). The fatigue life is however of magnitude 10^6 [years] which is very large.

All the potential response frequencies for the case of uniform flow with no springs attached (Orientation 2) are listed in Table 6.9.

Table 6.9 shows that the length of the excitation zone for all the response frequencies is 3604m. Hence the higher order modes, wich have the lowest ranks, will excitate along the whole length of the model in the time sharing method. In the space sharing method only mode number 1 will be active however. This is because it is occupying the whole length of the model. This

Table 6.9: Potential response frequencies found with constant current velocity and no springs attached in Orientation 2

Mode no.	$f_{osc}[Hz]$	Rank	$L_{exc.zone}[m]$
1	0.0271	1	3604
2	0.0522	2	3604
3	0.0545	3	3604
4	0.0639	4	3604

could be an explanation why the time sharing method gives more fatigue damage than the the space sharing method.

6.7 VIV analysis of pure CF in Orientation 3

6.7.1 Experimental results used in the static analysis

The following values from the experiments were used in the static analyses in Orientation 3:

Table 6.10: Parameters from the experimental results used in the static analysis in Orientation 3.

Parameter	Value
C_D	0.5 [-]
$C_{a,CF}$ (still water)	0.7 [-]

The added mass coefficient in still water (C_a) was found from the added mass contour plot (Orientation 3) using the same method as described for Orientation 1 and 2.

6.7.2 Excitation coefficients and excitation region used in the VIVANA analyses

The excitation region used in the VIVANA analysis for Orientation 3 is shown in Figure 6.9.

Figure 6.9 shows that the excitation region is between $\hat{f} = 0.219$ and $\hat{f} = 0.284$). 14 excitation coefficient curves were made inside this region. The excitation region is the smallest of all the three orientations.

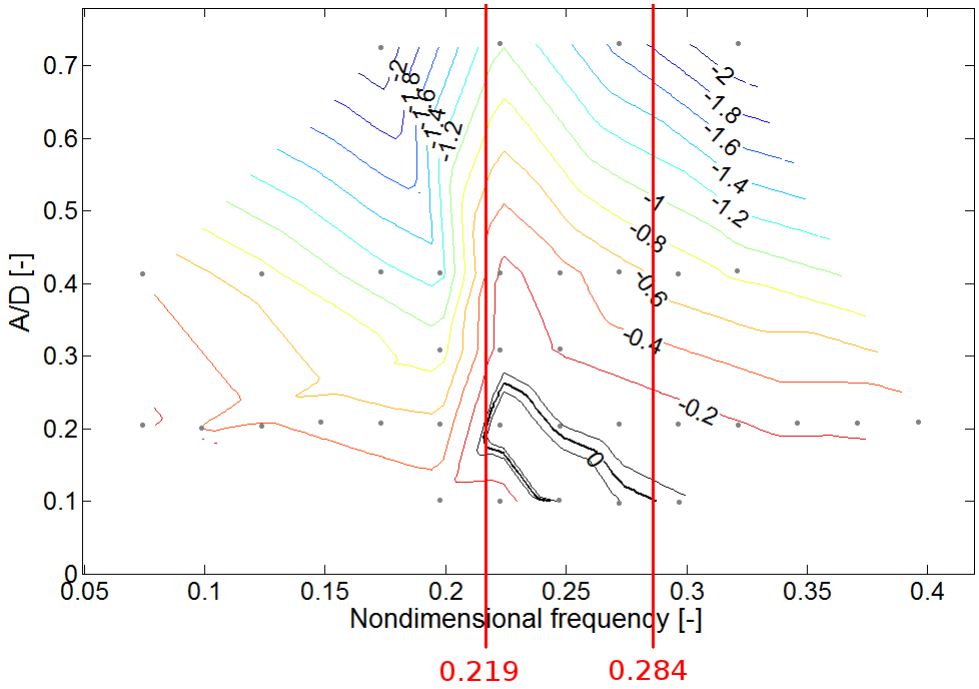

Figure 6.9: The excitation region used for the Orientation 3 VIVANA analysis.

6.7.3 Added mass for the VIVANA analyses

The added mass coefficients for Orientation 3 were selected at an A/D ratio of 0.2 as shown in Figure 6.10.

The A/D ratio was selected to be inside the A/D boundaries of the excitation region.

6.7.4 Strouhals number and drag coefficient for the VIVANA analyses

The Strouhals number was found to be 0.248 in Orientation 3, as described in Section 5.8.3. This is significantly higher than the default Strouhals curve in VIVANA for the same Re. The Strouhals number in Orientation 3 is unknown for other Re values. It may however be assumed that the St will be higher than the default curve for other Re too. Due to this the Strouhals

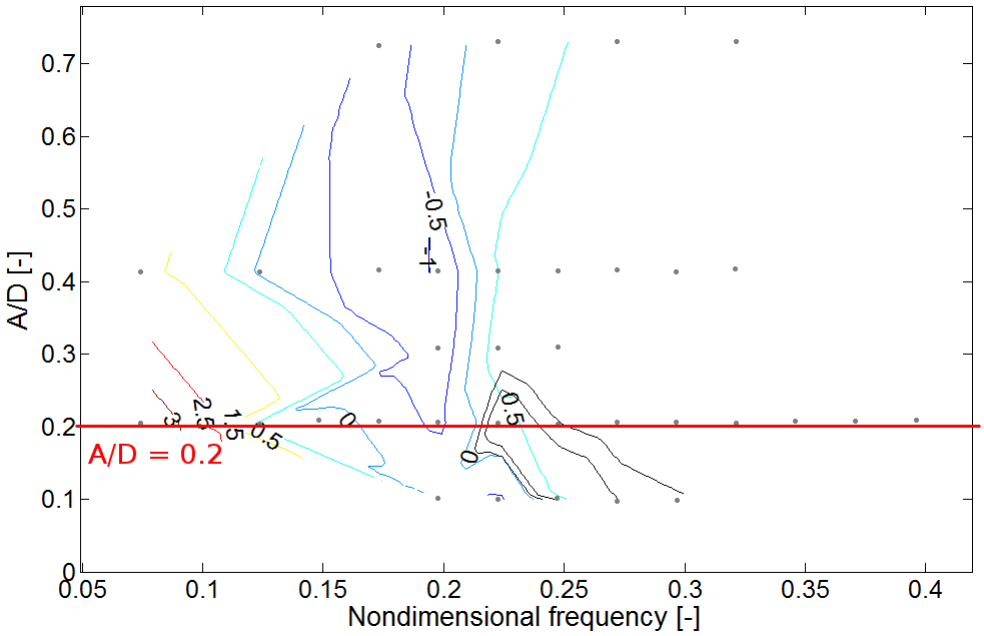

Figure 6.10: The added mass used for the Orientation 3 VIVANA analysis.

number has been set to be a constant 0.248 for all Re.

6.7.5 VIV results for Orientation 3

The VIV results in Orientation 3 are shown in Table 6.11 and 6.12.

Table 6.11: VIV results for Orientation 3 using the space sharing method.

Current profile	Springs	Dominating mode	Fatigue life [years]
1	no	5	$3.9915 \cdot 10^6$
1	yes	n/a	n/a
2	no	5	$4.5569 \cdot 10^6$
2	yes	n/a	n/a

Table 6.11 and 6.12 show that VIV will only occur when the artificial seabed is detached from the floating bridge and tunnel, in Orientation 3. That means for the cases without springs.

The potential response frequencies for the case of uniform flow with no springs attached are shown in Table 6.13.

Table 6.12: VIV results for Orientation 3 using the time sharing method.

Current profile	Springs	Dominating mode	Fatigue life [years]
1	no	5	$3.6934 \cdot 10^6$
1	yes	n/a	n/a
2	no	5	$4.5508 \cdot 10^6$
2	yes	n/a	n/a

Table 6.13: Potential response frequencies found with constant current velocity and no springs attached in Orientation 3

Mode no.	$f_{osc}[Hz]$	Rank	$L_{exc.zone}[m]$	$A_{max,ts}[m]$
1	0.0091	5	0	n/a
2	0.0181	5	0	n/a
3	0.0722	4	815	$0.71144 \cdot 10^{-10}$
4	0.0742	3	1533	0.28550
5	0.0807	1	3604	0.47734
6	0.0920	2	3400	0.23315

By comparing the results from Table 6.11 and 6.12, for the case of uniform flow with no springs attached, it is seen that time sharing gives a fatigue life only 7.46% lower than the space sharing method. The reason for this could partly be explained from the length of the excitation zones for each response frequency, shown in Table 6.13. It is seen that only mode number 5 has an excitation zone equal to the full length of the model. That means when the other modes are active in the time sharing method, they will not give as much damage as they would have done if their excitation zone was 3604m. Another possible reason is that the response frequency with the highest rank has also the second largest frequency. Hence this mode will contribute more to the fatigue damage compared to the lower frequencies. On the other hand mode number 6 has an excitation zone length of 3400m. Hence this mode would be expected to give a large contribution to the fatigue damage using the time sharing method. The amplitude of mode number 6 is however about 51% lower than the amplitude of mode number 5. This will give a lower fatigue damage than if the amplitudes for mode number 5 and 6 were the same.

6.8 Discussion of the VIVANA results

Comparing the results for Orientation 1, 2 and 3 it is seen that the shortest fatigue life is found in Orientation 1. The value is $0.23919 \cdot 10^6$ years. This was for a case where the artificial seabed was assumed connected to the floating bridge and tunnel. For the cases where the artificial seabed was assumed detached from the floating bridge and tunnel, the shortest fatigue life was found to be $0.24240 \cdot 10^6$ years. This was also found in Orientation 1.

The variation in results of the three orientations is probably mainly due to the difference in hydrodynamic coefficients, and especially the difference in the excitation coefficients. Orientation 1 is the orientation with the widest excitation region. Orientation 3 has by far the smallest excitation region of the three orientations.

The Strouhals number used is different in Orientation 1, 2 and 3. This will also probably contribute to the difference in results for the three orientations.

Chapter 7

Conclusion

The objectives of this master thesis was to calculate vortex induced vibrations (VIV) on an artificial seabed when connected to and detached from a floating bridge and tunnel. The VIV calculations were done using the software VIVANA. Another objective was to conduct experiments with a bundle model consisting of three pipes. This was to get hydrodynamic data for use in the VIV calculations in VIVANA.

The experiments were done in the Marine Cybernetics Laboratory at NTNU over a period of two weeks. The bundle model was tested in three orientations relative to the flow direction. Both pure CF and combined CF/IL tests using forced vibrations were done. The results were excitation, added mass, drag and lift coefficients from different combinations of nondimensional amplitudes and frequencies. The Strouhals number was also found for each orientation. The results from the pure CF runs were used in the VIV calculations in VIVANA. The results from the combined test runs showed that the given combinations of IL and CF motions would not give any VIV. Hence only the pure CF results were used in VIVANA.

The pure CF analyses in VIVANA were done using a full model and simple model of the artificial seabed. The full model was used for static analyses in RIFLEX only. The simple model was used for the VIV analyses in VIVANA in addition to the static analyses in RIFLEX. All the tests were done in three orientations relative to the current flow. It was focused on finding the fatigue life and dominating mode from each analysis. The shortest fatigue life found, for a case where the artificial seabed was assumed connected to the floating bridge and tunnel, was $0.23919 \cdot 10^6$ years. For the cases where the artificial seabed was assumed detached from the floating bridge and tunnel,

the shortest fatigue life was found to be $0.24240 \cdot 10^6$ years. The large values indicate that vortex induced vibrations will not be a problem for the artificial seabed. The results are however uncertain due to the limitations of the study.

Chapter 8

Recommendations for further work

The limitations in the combined tests of the experiments were done by testing only two different phase angles of the CF/IL motions. Also the number of amplitudes were limited. Hence it is recommended to do a more in-depth study of the combined CF/IL motions. The results from such a study could be used in a combined CF/IL analysis in VIVANA.

An important assumption done in the model experiments was the assumption that the three pipes in the bundles of the artificial seabed will be in direct contact with each other. If the configuration of the bundle changes significantly, it may be necessary to conduct experiments using a new bundle model.

The number and position of the crossbars going from the artifical seabed to the tunnel were based on an assumption. Since this part of the design is not ready yet, it may be of interest to do a sensitivity analysis using many different combinations of crossbars on the tunnel.

The pure cross-flow analyses done in VIVANA are based on some rough assumptions when it comes to the Strouhals number. This is because the Strouhals numbers found in the experiments were only valid for a Reynolds number of approximately $2.0 \cdot 10^4$. It is therefore suggested to find the Strouhals number curves as a function of Reynolds number. The new Strouhals number curves could then be used in a new VIVANA analysis.

References

Aronsen, K. H. (2007). *An experimental investigation of in-line and combined in-line and cross-flow vortex induced vibrations.* PhD thesis, Departement of Marine Technology NTNU.

Deepocean. (2014). *Kunstig sjøbunn.*

Faltinsen, O. M. (1990). *Sea loads on ships and offshore structures.* Cambridge.

Fjeld, A. (2013). *Mulighetsstudie for kryssing av sognefjorden.* Olav Olsen Group.

Grevstad, S. (2014). *Project thesis: Vortex induced vibrations on "artificial seabed" for floating bridge.*

Guttman, I., & Wilks, S. S. (1965). *Introductory engineering statistics.* John Wiley & Sons, Inc.

Larsen, C. M. (2010). *Viv - a short and incomplete introduction to fundamental concepts.* Departement of Marine Technology NTNU.

MathWorks. (2015). *trapz - trapezoidal numerical integration.* Retrieved from `http://se.mathworks.com/help/matlab/ref/trapz.html` ([Online; accessed 9-June-2015])

NTNU. (n.d.). *Mc lab carriage remote control user manual.*

NTNU. (2015). *Marine cybernetics laboratory (mc-lab).* Retrieved from `http://www.ntnu.no/imt/lab/cybernetics` ([Online; accessed 7-June-2015])

Passano, E., Larsen, C. M., Lie, H., & Wu, J. (2014a). *Vivana theory manual* (4.2 ed.). MARINTEK.

Passano, E., Larsen, C. M., Lie, H., & Wu, J. (2014b). *Vivana user manual* (4.2 ed.). MARINTEK.

Reinertsen. (2014). *Kunstig sjøbunn - kvalifiseringsstudie for nytt forankringskonsept.*

Reiso, M. (2015). private communication.

Riflex user manual (4.2 ed.). (2014). MARINTEK.

Senga, H., & Larsen, C. M. (2014). *Experimental investigation of cylinders with helical strakes.*

SINTEF. (2011). *Mulighetsstudie for kryssing av sognefjorden oppedal-lavik. estimat på bølger og strøm.*

Wahl, T. (2015). private communication.

Walpole, R. E., Myers, R. H., Myers, S. L., & Ye, K. (2007). *Probability & statistics for engineers & scientists.* Pearson Education International.

Yin, D. (2013). *Experimental and numerical analysis of combined in-line and cross-flow vortex induced vibrations.* PhD thesis, Departement of Marine Technology NTNU.

Appendix A

MATLAB code for creating MCL files

```
% clear
clear all;
clc;

% type of run: CF, IL or combined
run = 'Combined';

% constants for this run
U = 0.2; % max 2 m/s!
D_h = 0.107735; % hydrodynamic diameter
amps_nondim = [1.4]; % non-dim amplitudes
freqs_nondim = [0.075]; % non-dim frequencies

for i = 1:length(amps_nondim);
    for j = 1:length(freqs_nondim);

        % clear data from previous run
        clear data;

        % calc amplitude and frequency CF
        Amp = amps_nondim(i)*D_h;
        f_osc = freqs_nondim(j)*U/D_h;
        omega = f_osc*2*pi;
        period = 1/f_osc;

        % calc amplitude and frequency IL
```

```
AmpIL = Amp*0.5;
f_oscIL = f_osc*2;
omegaIL = f_oscIL*2*pi;
periodIL = 1/f_oscIL;
alpha = 0;

% constants
dT = 0.02;
acc = 0.1; % max 0.5 m/s^2
dX = 20; % tank length

% name of output file
filedir = ['./', run, '_U=',num2str(U), '/'];
mkdir(filedir);
filename = [filedir, run, '_U=',num2str(U),'...
    _nondim_amp=',num2str(amps_nondim(i)),'...
    _nondim_freq=',num2str(freqs_nondim(j))];

% program 'warm up' CF oscillations
num_amps = 10;
t_warmup = 0:dT:period*num_amps;
lambda = 0.025; % must be low to get harmonic acc
z = Amp*exp(-lambda*t_warmup).*cos(omega*t_warmup);
z = fliplr(z);
t_warmup = fliplr(t_warmup);

% program 'warm up' IL oscillations
num_ampsIL = 10;
t_warmupIL = 0:dT:periodIL*num_ampsIL;
lambdaIL = 0.025; % must be low to get harmonic acc
x = AmpIL*exp(-lambdaIL*t_warmupIL).*sin(omegaIL*...
    t_warmupIL+alpha);
x = fliplr(x);
t_warmupIL = fliplr(t_warmupIL);

% program steady CF oscillations
num_steady_osc = 200; % excess will be removed later
t_start = t_warmup(end)-dT;
t_end = t_start - num_steady_osc*period;
i_start = length(t_warmup)+1;
t_warmup = [t_warmup, t_start:-dT:t_end];
i_end = length(t_warmup);
z = [z, Amp*cos(omega*t_warmup(i_start:i_end))];

% program steady IL oscillations
```

```
        num_steady_oscIL = 200; % excess will be removed ...
            later
        t_startIL = t_warmupIL(end)-dT;
        t_endIL = t_startIL - num_steady_oscIL*periodIL;
        i_startIL = length(t_warmupIL)+1;
        t_warmupIL = [t_warmupIL, t_startIL:-dT:t_endIL];
        i_endIL = length(t_warmupIL);
        x = [x, AmpIL*sin(omegaIL*t_warmupIL(i_startIL:...
            i_endIL)+alpha)];

        % reset t_warmup matrix
        osc_before_start = 5;
        t_warmup = 0:dT:period*num_amps+dT+osc_before_start*...
            period;

        % program x displacement carriage
        T1=U/acc;
        t=[];
        x0 = 0*t_warmup;
        t1=0:dT:T1;
        x1=.5*acc*t1.^2;
        T2=(dX-2*x1(end))/U;
        t2=dT:dT:T2;
        x2=x1(end)+U*t2;
        t3 = [t1(1:end-1), t1(end)+dT];
        x3=x2(end)+(U-1/2*acc.*t3).*(t3+dT);
        t=[t_warmup, t_warmup(end)+dT+t1,t_warmup(end)+t1...
            (end)+t2+dT,t_warmup(end)+t1(end)+t2(end)+t1+2*dT...
            ];
        X=[x0,x1,x2,x3]';

        % make zero velocity at the end
        X(end) = X(end-1);

        % write to data matrix
        data(:,5) = z(1:length(t));
        data(:,6) = data(:,5);
        data(:,3) = -x(1:length(t));
        data(:,1) = X(1:length(t));

        % calculate z velocity and acc for plots
%           vel_carriage = (data(2:end,1)-data(1:end-1,1))/dT...
    ;
%           vel = (data(2:end,5)-data(1:end-1,5))/dT;
%           acc=(vel(2:end,1)-vel(1:end-1,1))/dT;
```

```
%
% %          % plots
            figure;
             plot(t,data(:,5));
%             figure;
%             plot(t,data(:,3));
%            figure;
%            plot(t(1:length(vel)), vel);
%           figure;
%           plot(t(1:length(acc)), acc);
%           figure;
%           plot(t(1:length(vel_carriage)), vel_carriage);

        % write MCL file
        write2mcl(filename, data, dT);
    end
end
```

Appendix B

MATLAB code for calculating data from test run files

```
% clear
close all;
clear all;
clc;

%runs = [256:261, 263, 264, 266, 267];% or 3 alpha pi

%runs = 193; % single run

fid=fopen('results_combined_alpha_0_or3.txt', 'r');
data = fscanf(fid, '%f %f %f %f %f %f %f %f %f %f %f %f %f...
    %f',[15 inf]);
runs = data(1,:);

for q=1:length(runs)

a = runs(q);

time_start_filter = data(2,q)/100-1;
time_end_filter = data(3,q)/100+1;

% clear
clearvars -except q i a data runs time_start_filter ...
   time_end_filter

filenr = sprintf('%03d',a);
```

```
% load file
file_name = [num2str(filenr) '.bin'];
%file_name = 'testcomb.bin'
[a1 file] = catman_read_5r8(file_name);

% data channels
channel_CF_force_starboard = 14;
channel_IL_force_starboard = 13;
channel_CF_force_port = 14;
channel_IL_force_port = 13;
channel_IL_acc_port = 5;
channel_CF_acc_port = 4;
channel_IL_acc_starboard = 5;
channel_CF_acc_starboard = 4;
channel_x_disp_carriage = 10;
channel_IL_displacement_port = 2;
channel_CF_displacement_port = 3;
channel_IL_displacement_starboard = 2;
channel_CF_displacement_starboard = 3;

% read time
ts = file(1).data;

% calibration data
calib_coeff_CF_force_starboard = 1;
calib_coeff_IL_force_starboard = 1;
calib_coeff_CF_force_port = 1;
calib_coeff_IL_force_port = 1;
calib_coeff_CF_acc_starboard = 1;
calib_coeff_IL_acc_starboard = 1;
calib_coeff_CF_acc_port = 1;
calib_coeff_IL_acc_port = 1;
calib_angle_force_starboard = 0;
calib_angle_force_port = 0;
calib_angle_acc_starboard = 0;
calib_angle_acc_port = 0;

% constants
scanfreq = 100;
L = 2.0;                              % Length of cylinder in m
rho = 999.2;                          % Water density
mass = 4.655 + 2*0.725 + 2*1.290 + 2*0.74 + 0.025^2*0.1613*L*...
    rho + 3*(pi/4)*0.047^2*L*rho; % Bundle mass in kg
D_h = 0.107735;                          % hydrodynamic diameter
```

```
dt  = 1/scanfreq;
%viscosity = 0.00000109;                % viscosity

% calculate IL and CF motion, force and acceleration (...
   including calibration factors)
motion_IL_port = -file(channel_IL_displacement_port).data;
motion_CF_port = -file(channel_CF_displacement_port).data;
force_IL_port = (file(channel_IL_force_port).data*...
   calib_coeff_IL_force_port*cos(calib_angle_force_port) - ...
   file(channel_CF_force_port).data*calib_coeff_CF_force_port...
   *sin(calib_angle_force_port));
force_CF_port = -(file(channel_IL_force_port).data*...
   calib_coeff_IL_force_port*sin(calib_angle_force_port) + ...
   file(channel_CF_force_port).data*calib_coeff_CF_force_port...
   *cos(calib_angle_force_port));
acc_IL_port = -file(channel_IL_acc_port).data*...
   calib_coeff_IL_acc_port*cos(calib_angle_acc_port) - file(...
   channel_CF_acc_port).data*calib_coeff_CF_acc_port*sin(...
   calib_angle_acc_port);
acc_CF_port = file(channel_IL_acc_port).data*...
   calib_coeff_IL_acc_port*sin(calib_angle_acc_port) + file(...
   channel_CF_acc_port).data*calib_coeff_CF_acc_port*cos(...
   calib_angle_acc_port);

i_start_filter = round(time_start_filter*scanfreq);
i_end_filter = round(time_end_filter*scanfreq);

% calculate U_mean (real U of carriage)
x_disp_carriage = file(channel_x_disp_carriage).data;
j = 0;
for i=i_start_filter:i_end_filter
   j = j+1;
   U_carriage(j) = 1/(2*dt)*(x_disp_carriage(i+1)-...
      x_disp_carriage(i-1));
end
U_mean = abs(mean(U_carriage));
motion_IL_port_mod = motion_IL_port; %- mean_IL_port;
motion_CF_port_mod = motion_CF_port; %- mean_CF_port;

j = 0;
k = 0;

for i=i_start_filter:(i_end_filter-1)
    if(motion_IL_port_mod(i+1) > 0 && motion_IL_port_mod(i) ...
       <= 0) % zero upcrossing
```

```
        j = j+1;
        zero_upcrossing_IL_port(j) = i;
    end
    if(motion_CF_port_mod(i+1) > 0 && motion_CF_port_mod(i) ...
       <= 0) % zero upcrossing
        k = k+1;
        zero_upcrossing_CF_port(k) = i;
    end
end
if exist('zero_upcrossing_IL_port') == 1
    i_start_filter_IL_port = zero_upcrossing_IL_port(1);
    i_end_filter_IL_port = zero_upcrossing_IL_port(length(...
       zero_upcrossing_IL_port));
else
    i_start_filter_IL_port = i_start_filter;
    i_end_filter_IL_port = i_end_filter;
end

if exist('zero_upcrossing_CF_port') == 1
    i_start_filter_CF_port = zero_upcrossing_CF_port(1);
    i_end_filter_CF_port = zero_upcrossing_CF_port(length(...
       zero_upcrossing_CF_port));
else
    i_start_filter_CF_port = i_start_filter;
    i_end_filter_CF_port = i_end_filter;
end

% amplitudes
amp_IL_port = mean(findpeaks(motion_IL_port(...
   i_start_filter_IL_port:i_end_filter_IL_port)));
amp_CF_port = mean(findpeaks(motion_CF_port(...
   i_start_filter_CF_port:i_end_filter_CF_port)));


% IL port
for i = 1:length(zero_upcrossing_IL_port)-1
    all_periods_IL_port(i) = ts(zero_upcrossing_IL_port(i+1))...
       -ts(zero_upcrossing_IL_port(i));
end
omega_IL_port = 2*pi/mean(all_periods_IL_port);
fcut = 2.3*omega_IL_port/(2*pi);
T_IL_port = (2*pi/omega_IL_port)*(length(...
   zero_upcrossing_IL_port)-1);
% CF port
for i = 1:length(zero_upcrossing_CF_port)-1
```

```
    all_periods_CF_port(i) = ts(zero_upcrossing_CF_port(i+1))...
       -ts(zero_upcrossing_CF_port(i));
end
omega_CF_port = 2*pi/mean(all_periods_CF_port);
fcut = 2.3*omega_CF_port/(2*pi);
T_CF_port = (2*pi/omega_CF_port)*(length(...
   zero_upcrossing_CF_port)-1);

% calculate velocity and acceleration from oscillations ...
   measured by
% potentiometer
% IL port
motion_IL_port_filtered = TSfilter(motion_IL_port_mod,0,fcut)...
   ;
j = 0;
for i = i_start_filter_IL_port-1:i_end_filter_IL_port+1
    j = j+1;
    vel_IL_port_filtered(j) = (motion_IL_port_filtered(i+1)-...
       motion_IL_port_filtered(i-1))/(2*dt);
end
j = 0;
for i = 2:length(vel_IL_port_filtered)-1
    j = j+1;
    acc_IL_port_filtered(j) = (vel_IL_port_filtered(i+1)-...
       vel_IL_port_filtered(i-1))/(2*dt);
end
% CF port
motion_CF_port_filtered = TSfilter(motion_CF_port_mod,0,fcut)...
   ;
j = 0;
for i = i_start_filter_CF_port-1:i_end_filter_CF_port+1
    j = j+1;
    vel_CF_port_filtered(j) = (motion_CF_port_filtered(i+1)-...
       motion_CF_port_filtered(i-1))/(2*dt);
end
j = 0;
for i = 2:length(vel_CF_port_filtered)-1
    j = j+1;
    acc_CF_port_filtered(j) = (vel_CF_port_filtered(i+1)-...
       vel_CF_port_filtered(i-1))/(2*dt);
end

% calc hydrodynamic force
% IL port
force_hydro_IL_port_mod = force_IL_port(...
```

```
    i_start_filter_IL_port:i_end_filter_IL_port)-mean(...
    force_IL_port(i_start_filter_IL_port:i_end_filter_IL_port)...
    );
force_hydro_IL_port = force_hydro_IL_port_mod(:) - mass*...
    acc_IL_port_filtered(:);
force_hydro_IL_port_filtered = TSfilter(force_hydro_IL_port...
    ,0,fcut)';
% CF port
force_hydro_CF_port_mod = force_CF_port(...
    i_start_filter_CF_port:i_end_filter_CF_port)-mean(...
    force_CF_port(i_start_filter_CF_port:i_end_filter_CF_port)...
    );
force_hydro_CF_port = force_hydro_CF_port_mod(:) - mass*...
    acc_CF_port_filtered(:);
force_hydro_CF_port_filtered = TSfilter(force_hydro_CF_port...
    ,0,fcut)';

end

% calculate drag coefficients
Cd_port = mean(force_IL_port(i_start_filter_IL_port:...
    i_end_filter_IL_port))/(0.5*rho*D_h*(L)*U_mean^2);
Cd_starboard = mean(force_IL_starboard(...
    i_start_filter_IL_starboard:i_end_filter_IL_starboard))/(0...
    .5*rho*D_h*(L)*U_mean^2);

% calc St
St_port = omega_CF_port/(2*pi)*D_h/U_mean;
St_SB = omega_CF_starboard/(2*pi)*D_h/U_mean;

% calculate RMS
fh_rmsA=std(force_hydro_CF_starboard_filtered);
crmsA=sqrt(2)*fh_rmsA/(0.5*rho*D_h*(L)*U_mean^2);
fh_rmsB=std(force_hydro_CF_port_filtered);
crmsB=sqrt(2)*fh_rmsB/(0.5*rho*D_h*(L)*U_mean^2);

Cl_port2 = 2*crmsB/(rho*D_h*(L)*U_mean^2);
Cl_starboard2 = 2*crmsA/(rho*D_h*(L)*U_mean^2);

% calculate lift coefficients
Cl_port = mean(force_CF_port(i_start_filter_CF_port:...
    i_end_filter_CF_port))/(0.5*rho*D_h*(L)*U_mean^2);
Cl_starboard = mean(force_CF_starboard(...
    i_start_filter_CF_starboard:i_end_filter_CF_starboard))/(0...
    .5*rho*D_h*(L)*U_mean^2);
```

```
% calculate added mass
% IL port
integrand_IL_port = -force_hydro_IL_port_filtered(:).*...
    acc_IL_port_filtered(:);
added_mass_IL_port = 2/(omega_IL_port^2*amp_IL_port)*1/...
    T_IL_port*trapz(ts(i_start_filter_IL_port:...
    i_end_filter_IL_port),integrand_IL_port)/(pi/4*D_h^2*rho*(...
    L)*omega_IL_port^2*amp_IL_port);
% CF port
integrand_CF_port = -force_hydro_CF_port_filtered(:).*...
    acc_CF_port_filtered(:);
added_mass_CF_port = 2/(omega_CF_port^2*amp_CF_port)*1/...
    T_CF_port*trapz(ts(i_start_filter_CF_port:...
    i_end_filter_CF_port),integrand_CF_port)/(pi/4*D_h^2*rho*(...
    L)*omega_CF_port^2*amp_CF_port);

% calculate excitation coefficient
% IL port
integrand_IL_port = force_hydro_IL_port_filtered(:).*...
    vel_IL_port_filtered(2:length(force_hydro_IL_port_filtered...
    )+1)';
Ce_IL_port = trapz(ts(i_start_filter_IL_port:...
    i_end_filter_IL_port),integrand_IL_port)*2/(omega_IL_port*...
    amp_IL_port*T_IL_port)/(0.5*rho*D_h*(L)*U_mean^2);
% CF port
integrand_CF_port = force_hydro_CF_port_filtered(:).*...
    vel_CF_port_filtered(2:length(force_hydro_CF_port_filtered...
    )+1)';
Ce_CF_port = trapz(ts(i_start_filter_CF_port:...
    i_end_filter_CF_port),integrand_CF_port)*2/(omega_CF_port*...
    amp_CF_port*T_CF_port)/(0.5*rho*D_h*(L)*U_mean^2);

% plots

% show tested non-dim amp and freq
x_jh=[0.23,0.3,0.35,0.4,0.5,0.62];
y_jh=[0,0.09,0.05,0.1,0.07,0.05];

x_dnv=[0.22,0.24,0.37,0.8,1];
y_dnv=[0,0.115,0.155,0.05,0];

x_ar1=[0.3,0.27,0.28,0.32,0.350,0.37,0.36];
y_ar1=[0.025,0.075,0.12,0.12,0.075,0.05,0.025];
```

```
x_ar2=[0.38,0.37,0.38,0.4,0.43,0.5,0.6,0.7,0.75];
y_ar2=[0.025,0.05,0.13,0.12,0.12,0.08,0.065,0.04,0.025];

fhat_CF = omega_CF_port*D_h/(2*pi)/U_mean;
aod_CF = amp_CF_port/D_h;

fhat_IL = omega_IL_port*D_h/(2*pi)/U_mean;
aod_IL = amp_IL_port/D_h;

% show unfiltered motions
figure(2);
subplot(4,1,1)
plot(ts,motion_CF_port,'k');ylabel('motion CF port');
subplot(4,1,2)
plot(ts,motion_CF_starboard,'k');ylabel('motion CF starboard'...
    );
subplot(4,1,3)
plot(ts,motion_IL_port,'k');ylabel('motion IL port');
subplot(4,1,4)
plot(ts,motion_IL_starboard,'k');ylabel('motion IL starboard'...
    );

% show unfiltered forces
figure(3);
subplot(4,1,1)
plot(ts,force_CF_port,'k');ylabel('force CF port');
subplot(4,1,2)
plot(ts,force_CF_starboard,'k');ylabel('force CF starboard');
subplot(4,1,3)
plot(ts,force_IL_port,'k');ylabel('force IL port');
subplot(4,1,4)
plot(ts,force_IL_starboard,'k');ylabel('force IL starboard');

% show unfiltered accelerations
figure(4);
subplot(4,1,1)
plot(ts,acc_CF_port,'k');ylabel('acc CF port');
subplot(4,1,2)
plot(ts,acc_CF_starboard,'k');ylabel('acc CF starboard');
subplot(4,1,3)
plot(ts,acc_IL_port,'k');ylabel('acc IL port');
subplot(4,1,4)
plot(ts,acc_IL_starboard,'k');ylabel('acc IL starboard');

% show filtered motions and forces
```

```
figure;
steadyzone_CF = (i_start_filter_CF_port:i_end_filter_CF_port)...
    ;
plot(ts(steadyzone_CF),motion_CF_port_mod(steadyzone_CF)/...
    amp_CF_port,ts(steadyzone_CF),force_hydro_CF_port_filtered...
    /mean(findpeaks(force_hydro_CF_port_filtered)),'k');legend...
    ('motion CF port','hydr. force CF port');

% Examine power spectra of acceleration signals
vy4_t=acc_IL_port(i_start_filter_IL_port:i_end_filter_IL_port...
    );
m=length(vy4_t)/2;
n=length(vy4_t);

fft_vy4t=fft(vy4_t);
Pyy4=fft_vy4t.*conj(fft_vy4t)/length(fft_vy4t);
Pyy4(m+2:n)=[ ];
Pyy4(2:m+1)=2*Pyy4(2:m+1);
freqshift2=1/dt*[0:length(vy4_t)/2]/length(vy4_t);
figure(6);
plot(freqshift2,Pyy4(1:length(freqshift2))/Pyy4(1),'k'); axis...
    ([0 5 0 inf]); ylabel('S_x [f] ','Fontsize',12);xlabel('f'...
    ,'Fontsize',12);
title('Accel_{CF} Spectrum for port side');

figure;
plot(motion_IL_port_mod(i_start_filter:i_end_filter),...
    motion_CF_port_mod(i_start_filter:i_end_filter));

% print St
St_port = omega_CF_port/(2*pi)*D_h/U_mean;

% print drag coeffs
Cd_port

% print lift coeffs
Cl_port

% print added mass
added_mass_CF=added_mass_CF_port
Ce_CF=Ce_CF_port

added_mass_IL=added_mass_IL_port;
Ce_IL=Ce_IL_port;
```

```
% write data to file
fid3=fopen(['results.txt'], 'a');
fprintf(fid3, '%3d\t%5d\t%5d\t%12.8f\t%12.8f\t%12.8f\t%12.8f\...
   t%12.8f\t%12.8f\t%12.8f\t%12.8f\t%12.8f\t%12.8f\t%12.8f\t...
   %12.8f\r\n', a, i_start_filter_CF_port, ...
   i_end_filter_CF_port, U_mean, fhat_CF, aod_CF, Ce_CF, ...
   added_mass_CF, Cd_port, Cl_port, Cl_port2, fhat_IL, aod_IL...
   , Ce_IL, added_mass_IL);
fclose(fid3);

% print non-dim diameter and freq
U_mean
fhat_CF
aod_CF

% %%% TRANSFORM ACCELERATION INTO VELOCITY AND DISPLACEMENT
fcut_accel=1.2;
fs_accel=0.2;

facc_bil=fft(-acc_IL_port);
facc_bcf=fft(-acc_CF_port); % positive displacement in 180 ...
   deg out of phase of acceleration
facc_ail=fft(acc_IL_port);
facc_acf=fft(-acc_CF_port);
infacc_bil=fftshift(facc_bil); infacc_bcf=fftshift(facc_bcf);
infacc_ail=fftshift(facc_ail); infacc_acf=fftshift(facc_acf);
freqshift=1/dt*[-length(infacc_bil)/2:length(infacc_bil)...
   /2-1]/length(infacc_bil);

% BANDPASS FILTER ACCELERATION SIGNALS
 for i=1:length(freqshift)
       fin=abs(freqshift(i));
       if (fin > fcut_accel) | (fin < fs_accel)
           filta_bil(i)=0;  filta_bcf(i)=0;  filta_ail(i)=0; ...
               filta_acf(i)=0;
       else
            filta_bil(i)=infacc_bil(i); filta_bcf(i)=...
               infacc_bcf(i);
            filta_ail(i)=infacc_ail(i); filta_acf(i)=...
               infacc_acf(i);
       end
 end


figure(20)
```

```
plot(freqshift,2/length(freqshift)*abs(filta_bil)); axis([0 ...
    10 -inf inf]); grid on;

% INTEGRATE SIGNALS IN FOURIER SPACE
for i=1:length(freqshift)
     v_bil_fft=filta_bil/(2*pi*freqshift(i)*sqrt(-1)); ...
        d_bil_fft=filta_bil/(2*pi*freqshift(i)*sqrt(-1))^2;
     v_bcf_fft=filta_bcf/(2*pi*freqshift(i)*sqrt(-1)); ...
        d_bcf_fft=filta_bcf/(2*pi*freqshift(i)*sqrt(-1))^2;
end

% Filtered Cylinder Acceleration
aoutfft_bil=ifftshift(filta_bil); aoutfft_bcf=ifftshift(...
    filta_bcf);
a_bil=real(ifft(aoutfft_bil)); a_bcf=real(ifft(aoutfft_bcf));

aoutfft_ail=ifftshift(filta_ail); aoutfft_acf=ifftshift(...
    filta_acf);
a_ail=real(ifft(aoutfft_ail)); a_acf=real(ifft(aoutfft_acf));

% % Filtered Cylinder Velocity
voutfft_bil=ifftshift(v_bil_fft); voutfft_bcf=ifftshift(...
    v_bcf_fft);
v_bil=real(ifft(voutfft_bil)); v_bcf=real(ifft(voutfft_bcf));

% % Filtered Cylinder Displacement
doutfft_bil=ifftshift(d_bil_fft);  doutfft_bcf=ifftshift(...
    d_bcf_fft);
d_bil=real(ifft(doutfft_bil));     d_bcf=real(ifft(...
    doutfft_bcf));

figure;
plot(ts,d_bcf/max(d_bcf),ts,motion_CF_port/max(motion_CF_port...
    )); legend('CF displacement from acceleration','CF ...
    displacement'); axis([time_start_filter time_end_filter -...
    inf inf]);
figure;
plot(ts,d_bil/max(d_bil),ts,motion_IL_port/max(motion_IL_port...
    )); legend('IL displacement from acceleration','IL ...
    displacement'); axis([time_start_filter time_end_filter -...
    inf inf]);

end
```

Appendix C

MATLAB code for creating contour plots

```
clear all;
close all;

%Ce_margin_error = 0.0466; %or3
Ce_margin_error = 0.0329; %or3
fhat_col = 5;
amp_col = 6;
Ce_col = 7;
Ca_col = 8;

fid3=fopen(['NEW_results_CF_or3.txt'], 'r');

data = fscanf(fid3, '%f %f %f %f %f %f %f %f %f %f %f',[11 ...
    inf]);
fclose(fid3);

x = data(fhat_col,:);
y = data(amp_col,:);
x = sort(x);
y = sort(y);

fineness = 0.005;
extra = 0.05;

[X,Y] = meshgrid(min(x)-extra/2:fineness:max(x)+extra/2,0:...
    fineness:max(y)+extra);
```

```
Ce_interpol = griddata(data(fhat_col,:),data(amp_col,:),data(...
    Ce_col,:),X,Y,'linear');
Ca_interpol = griddata(data(fhat_col,:),data(amp_col,:),data(...
    Ca_col,:),X,Y,'linear');
Cd_interpol = griddata(data(fhat_col,:),data(amp_col,:),abs(...
    data(9,:)),X,Y,'linear');
Cl_interpol = griddata(data(fhat_col,:),data(amp_col,:),data...
    (10,:),X,Y,'linear');

% Ce contour plot

figure('Color','white','Position', [100, 100, 1149, 895]);

%v = [-0.9,-0.75,-0.5,0,0.5:0.25:2.0]; % Ca or 1 pure CF
%v = [-4.0:1.0:-1,-0.5,0.5,0.7]; % Ce or 1 pure CF
%v = [-0.6:0.2:0.6,0.7]; % Ce or 2 pure CF
%v = [-0.5, 0.0, 1.1, 2:1.0:5.0]; % Ca or 2 pure CF
%v = [-2:0.2:-0.2]; % Ce or 3 pure CF
%v = [-1,-0.5,0,0.5:1.0:3.5,3.0]; % Ca or 3 pure CF
[C, h] = contour(X,Y,Ce_interpol,'ShowText','on');
clabel(C,h,'LabelSpacing',962);
clabel(C,h,'FontSize',13+5);
hold on;

% Pure CF zero line

% Ce_pureCF = griddata(data2(fhat_col,:),data2(amp_col,:),...
    data2(Ce_col,:),X,Y,'linear');
% v = [0,0];
% contour(X,Y,Ce_pureCF, v, 'ShowText','off','LineWidth',2,'...
    Linecolor',[0 0 0]);

% 95% confidence interval lines

v = [0,0];
%[C, h] = contour(X,Y,Ce_interpol,v,'ShowText','on','...
    LineWidth',2,'Linecolor',[0 0 0]);
%clabel(C,h,'LabelSpacing',312);
clabel(C,h,'FontSize',13+5);
contour(X,Y,Ce_interpol+Ce_margin_error, v, 'ShowText','off',...
    'LineWidth',1,'Linecolor',[0 0 0]);
contour(X,Y,Ce_interpol-Ce_margin_error, v, 'ShowText','off',...
    'LineWidth',1,'Linecolor',[0 0 0]);
```

```
s = scatter(data(fhat_col,:),data(amp_col,:),10,'filled','...
    MarkerEdgeColor',[.5,.5,.5],'MarkerFaceColor',[.5,.5,.5]);
legend(s, 'Actual test runs');

xlabel('Nondimensional frequency [-]','FontSize',15+5);
ylabel('A/D [-]','FontSize',15+5);

set(gca,'FontSize',14+5);

% Ca contour plot

figure('Color','white');
[C h] = contour(X,Y,Ce_interpol, 'ShowText','on')
clabel(C,h,'LabelSpacing',172);
clabel(C,h,'FontSize',13);
hold on;

s = scatter(data(fhat_col,:),data(amp_col,:),10,'filled','...
    MarkerEdgeColor',[.5,.5,.5],'MarkerFaceColor',[.5,.5,.5]);
h = legend(s, 'Actual test runs');
%set(h, 'FontSize', 7);

xlabel('Nondimensional frequency [-]','FontSize',15);
ylabel('A/D [-]','FontSize',15);

set(gca,'FontSize',14);

% Drag contour plot

figure('Color','white');
[C h] = contour(X,Y,Cd_interpol, 'ShowText','on')
clabel(C,h,'LabelSpacing',172);
clabel(C,h,'FontSize',13);
hold on;
s = scatter(data(fhat_col,:),data(amp_col,:),10,'filled','...
    MarkerEdgeColor',[.5,.5,.5],'MarkerFaceColor',[.5,.5,.5]);
h = legend(s, 'Actual test runs');
%set(h, 'FontSize', 7);

xlabel('Nondimensional frequency [-]','FontSize',15);
ylabel('A/D [-]','FontSize',15);

set(gca,'FontSize',14);

% Lift contour plot
```

```
figure('Color','white');
[C h] = contour(X,Y,Cl_interpol, 'ShowText','on')
clabel(C,h,'LabelSpacing',172);
clabel(C,h,'FontSize',13);
hold on;
s = scatter(data(fhat_col,:),data(amp_col,:),10,'filled','...
   MarkerEdgeColor',[.5,.5,.5],'MarkerFaceColor',[.5,.5,.5]);
h = legend(s, 'Actual test runs');
%set(h, 'FontSize', 7);

xlabel('Nondimensional frequency [-]','FontSize',15);
ylabel('A/D [-]','FontSize',15);

set(gca,'FontSize',14);

fid3=fopen(['Ce_vivana_or3.dat'], 'w');
fid4=fopen(['Cadded_vivana_or3.dat'], 'w');

% NB!!!change for each orientation
a = 0.01;
b = 0.5;

for i = 1:length(X(1,:));
    f_hat = unique(X(:,i));
    if (unique(X(:,i)) >= a && unique(X(:,i)) <= b)
    [value, Ce0_index] = min(abs(Ce_interpol(:,i)));
    [Ce_max_value, Ce_max_index] = max(Ce_interpol(:,i));
    A_Ce0 = unique(Y(Ce0_index,:));
    A_Cemax = unique(Y(Ce_max_index,:));
    if(Ce_max_value > 0)
        fprintf(fid3, '%3.3f %3.2f %3.2f %3.2f %3.2f\r\n', ...
            f_hat, A_Ce0, A_Cemax, Ce_max_value, 0.0);
    end
    end
    % added mass
    amp_half_index = find(Y(:,i) == 0.6);
    Ca = Ca_interpol(amp_half_index,i);
    if (~isnan(Ca))
    fprintf(fid4, '%3.3f %3.1f\r\n', f_hat, Ca);
    end
end

fclose(fid3);
fclose(fid4);
```